ÇUKUROVA UNIVERSITY
INSTITUTE OF NATURAL AND APPLIED SCIENCES

PhD THESIS

Neslihan SARIGÜL

EXAMINATION OF GENERAL CAVITY THEORY FOR MAGNESIUM AND TITANIUM DOPED LITHIUM FLUORIDE (TLD-100) IN BONE AND LUNG HETEROGENEITIES

DEPARTMENT OF PHYSICS

ADANA, 2014

ÇUKUROVA UNIVERSITY
INSTITUTE OF NATURAL AND APPLIED SCIENCES

EXAMINATION OF GENERAL CAVITY THEORY FOR MAGNESIUM AND TITANIUM DOPED LITHIUM FLUORIDE (TLD-100) IN BONE AND LUNG HETEROGENEITIES

Neslihan SARIGÜL

PhD THESIS

DEPARTMENT OF PHYSICS

We certify that the thesis titled above was reviewed and approved for the award of degree of the Doctor of Philosophy by the board of jury on 20/05/2014.

……	…….	……..…
Prof. Dr. Zehra YEGİNGİL	Assoc. Prof. Dr. Bülent AYDOĞAN	Prof. Dr. Vedat PEŞTEMALCI
SUPERVISOR	Co. SUPERVISOR	MEMBER

……	……...
Prof.Dr.Süleyman GÜNGÖR	Asst. Prof. Dr. Sema DÜZENLİ
MEMBER	MEMBER

This PhD Thesis is written at the Department of Institute of Natural And Applied Sciences of Çukurova University.
Registration Number:

Prof. Dr. Mustafa GÖK
Director
Institute of Natural and Applied Sciences

ABSTRACT

PhD THESIS

EXAMINATION OF GENERAL CAVITY THEORY FOR MAGNESIUM AND TITANIUM DOPED LITHIUM FLUORIDE (TLD-100) IN BONE AND LUNG HETEROGENEITIES

Neslihan SARIGÜL

ÇUKUROVA UNIVERSITY
INSTITUTE OF NATURAL AND APPLIED SCIENCES
DEPARTMENT OF PHYSICS

Supervisor : Prof. Dr. Zehra YEĞİNGİL
II. Supervisor : Assoc. Prof. Dr. Bülent AYDOĞAN

Year: 2014, Pages: 152

Jury : Prof. Dr. Zehra YEĞİNGİL
: Prof. Dr. Vedat PEŞTEMALCI
: Prof. Dr. Süleyman GÜNGÖR
: Assoc. Prof. Dr. Bülent AYDOĞAN
: Asst. Prof. Dr. Sema DÜZENLİ

The aim of this thesis is to examine the accuracy of Burlin general cavity theory in bone and lung heterogeneities when measuring dose using TLDs of various thicknesses. A practical framework to convert the dose to TLD to the dose in medium using a correction factor is developed and verified.

Burlin cavity theory is verified in bone and lung, the most relevant heterogeneities in radiological physics. Theoretical calculations, experimental measurements and Monte Carlo simulations of $(f)_{\text{medium}}^{\text{TLD}}$were performed and compared for LiF: Mg,Ti (TLD-100) in bone and lung. Experimental setup included TLDs of three common thicknesses (0.015, 0.038 and 0.089 cm) that were irradiated in bone, lung, and water phantoms with 6 MV photon beam. $(f)_{\text{water}}^{\text{TLD}}$ is applied to convert the dose to TLD to the dose to medium, for which this study propose to use the Monte Carlo calculated values. Monte Carlo simulations of the same experiments were performed using BEAMnrc software. Theoretical calculations of Burlin general cavity theory were performed for 18 combinations of parameters including 6 different mass effective attenuation coefficient (β) and three different average path length of electrons across the cavity (g) which had been suggested in the previous studies. In the final step, $(f)_{\text{water}}^{\text{medium}}$factors calculated with Burlin cavity theory were compared with MC simulation factors in bone and lung for an experimental setup generally being used during treatment planning system (TPS) commissioning in order to verify heterogeneity correction models.

Theoretical f ($(f)_{\text{bone}}^{\text{TLD}}$, $(f)_{\text{lung}}^{\text{TLD}}$) factors calculated for 18 combinations agreed well to each other and fall within 1% deviation to that of Monte Carlo analysis for both bone and lung (SD = 0.1%) heterogeneities. $(f)_{\text{water}}^{\text{TLD}}$ factors of 0.833, 0.837 and 0.840 cm thick TLDs were used to convert the experimental TLD readings in bone and lung heterogeneities within the conversion framework being calculated with MC simulation. The *f* factor for bone was observed as decreases slightly for bone while it increases slightly for lung with increasing TLD thicknesses. In regard to the analyzes of results there were no statistically significant change in f factors with TLD thicknesses. The standard deviation differences between the MC simulations and theoretical calculations $(f)_{\text{water}}^{\text{medium}}$ factors for bone and lung using 0.089cm TLDs were 0.1% and 1.3%, respectively. The TLD measurements that were converted using theoretically calculated$(f)_{\text{water}}^{\text{medium}}$ factors have good agreement within 1% with the MC simulations for the experimental set up for both lung and bone.

In order to achieve a systematic comparison in different materials Burlin Cavity theory was chosen as it is adaptable to bone and lung which haven't been studied yet or dose verification in medical applications. Instead of Burlin cavity theory for TLDs, we derived and verified a new framework to convert dose to medium. The results for bone and lung were in good agreement when compared with MC simulations and theoretical calculations. This study suggests that$(f)_{\text{water}}^{\text{medium}}$ simulated by MC can be used for dose to medium conversion especially in high Z materials such as bone. Burlin cavity theory for TLDs inserted in bone and lung, the two most relevant heterogeneity in medical physics, was found to be accurate within the uncertainties.

Key Words: Burlin cavity theory, thermoluminescence dosimetry (TLD-100), bone, lung, heterogeneity, Monte Carlo simulation EGSnrc

ÖZ

DOKTORA TEZİ

EXAMINATION OF GENERAL CAVITY THEORY FOR MAGNESIUM AND TITANIUM DOPED LITHIUM FLUORIDE (TLD-100) IN BONE AND LUNG HETEROGENEITIES

Neslihan SARIGÜL

ÇUKUROVA ÜNİVERSİTESİ
FEN BİLİMLERİ ENSTİTÜSÜ
FİZİK ANABİLİM DALI

Danışman : Prof. Dr. Zehra YEĞİNGİL
İkinci Danışman : Doç. Dr. Bülent AYDOĞAN
Yıl: 2014, Sayfa: 152
Jüri : Prof. Dr. Zehra YEĞİNGİL
: Prof. Dr. Vedat PEŞTEMALCI
: Prof. Dr. Süleyman GÜNGÖR
: Doç. Dr. Bülent AYDOĞAN
: Yar.Doç. Dr. Sema DÜZENLİ

Bu çalışma, TLD kullanılarak kemik ve akciğer heterojen ortamlarında doz ölçmek için Burlin genel kavite teorisinin kullanımının doğruluğunu araştırmayı amaçlamıştır. Deneysel verilerin ve Monte Carlo simülasyon verilerinin kombinasyonu kullanılarak elde edilen bir düzeltme faktörü kullanılarak TLD ölçüm dozunu kemik ve akciğer gibi heterojen bir ortamdaki ortam dozuna çeviren bir metot geliştirilmiş ve doğrulanmıştır.

Radyoloji fiziğinde kemik ve akciğer gibi en yaygın kullanılan iki heterojen ortam içinde Burlin kavite teorisi doğrulandı. Magnezyum ve titanyum katkılı lityum florit termolüminesans dozimetreler (TLD-100) için kemik ve akciğer heterojen ortamları baz alınarak $(f)^{\mathrm{TLD}}_{\mathrm{medium}}$ un teorik hesaplamaları, deneysel analizleri ve Monte Carlo simülasyonları yapılmış ve karşılaştırılmıştır. Deney düzeneği kemik, akciğer ve su fantomunda 6 MV foton demeti ile ışınlanmış üç farklı kalınlıkta (0.015, 0.038 ve 0.089 cm) TLD'leri içermiştir. Monte Carlo simulasyonundan elde edilmiş ve bu çalışmada önerilen $(f)^{\mathrm{TLD}}_{\mathrm{water}}$ değerleri TLD deki dozun ortamdaki doza çevirilmesi için deneysel sonuçlara uygulandı. Aynı deneylerin Monte Carlo simülasyonları BEAMnrc yazılımı kullanılarak yapılmıştır. Burlin genel kavite teorisinin teorik hesaplamaları daha önceki benzer çalışmalarda önerilen 6 farklı etkin kütle zayıflatma katsayısı (β) ve 3 farklı elektronun kavite boyunca ortalama yol uzunluğu (g) gibi parametrelerin 18 kombinasyonu için gerçekleştirilmiştir. Teorik, deneysel ve MC ile elde edilen $(f)^{\mathrm{TLD}}_{\mathrm{medium}}$ değerleri karşılaşırılmıştır. Son olarak, heterojenite düzeltme modelinin doğruluğunu sınamak amacı ile genellikle tedavi planlama sistemi (TPS) süresince kullanılan deneysel düzenek için kemik ve akciğer içerisinde Burlin kavite teorisi ile elde edilen $(f)^{\mathrm{medium}}_{\mathrm{water}}$ faktörleri Monte Carlo simülasyonuyla karşılaştırılmıştır.

Teorik $(f)^{\mathrm{TLD}}_{\mathrm{medium}}$faktörleri hem kemik hem de akciğerde Monte Carlo analizlerin (SD=0.1%) %1'i içerisindeki tekrarlanabilir değerler ile elde edilen 18 durum için hesaplanmıştır. İnce, orta ve kalın TLD'ler için sırasıyla 0.833, 0.837 ve 0.840 cm olarak Monte Carlo ile hesaplatılmış $(f)^{\mathrm{TLD}}_{\mathrm{water}}$ faktörleri kemik ve akciğer heterojen ortamlarındaki deneysel TLD okumalarını çevirmek için kullanılmıştır. TLD kalınlığı arttırıldığında $(f)^{\mathrm{TLD}}_{\mathrm{medium}}$ faktörü kemik için kısmen azalırken, akciğer için ise kısmen artmıştır. Fakat sonuçların analizine göre kemik ve akciğer içerisinde TLD kalınlığının artmasıyla $(f)^{\mathrm{TLD}}_{\mathrm{medium}}$ faktöründe istatistik açıdan önemli bulunacak bir değişim gözlenmemiştir. 0.089 cm lik TLD ler kullanılarak kemik ve akciğer için teorik olarak ve MC ile hesaplanmış olan $(f)^{\mathrm{medium}}_{\mathrm{water}}$ değerleri arasındaki standart sapma sırasıyla % 0,1 ve % 1,3 olarak hesaplanmıştır.

Burlin kavite teorisinin uygulamaları farklı materyaller içerisinde yaygın olarak çalışılmıştır fakat medikal uygulamalarda doz doğruluğu ile ilişkili olan kemik ve akciğer ortamlarında çalışılmamıştır. Bu çalışma kemik gibi yüksek atom numarasına (Z) sahip materyallerdeki doz dönüşümü için MC simülasyonu ile elde edilen $(f)^{\mathrm{medium}}_{\mathrm{water}}$ faktörünü önerir. TLD dozunu ortam dozuna çevirmede kullanılan $(f)^{\mathrm{medium}}_{\mathrm{water}}$faktörü deneysel doz ölçümleri ile Monte Carlo hesaplamalarının kombinasyonu kullanılarak hesaplanmıştır. Geliştirilen metotla hesaplatılan f faktörleri teorik ve Monte Carlo sonuçları ile oldukça uyumlu çıkmıştır. Medikal fizik çalışmalarında sıkça karşılaşılan iki heterojen ortam olan: kemik ve akciğer içerisindeki TLD ler için Burlin cavity theorisinin doğru olduğu bulunmuştur.

Anahtar Kelimeler: Burlin kavite teorisi, termolüminesans dozimetresi (TLD-100), kemik ve akciğer, heterolen ortamlar, Monte Carlo simülasyonu EGSnrc

ACKNOWLEDGEMENTS

First of all, I would like to thank to my supervisor, Prof. Dr. Zehra Yeğingil, for her invaluable assistance and directions throughout the course of my research. I would also like to thank to Prof. Dr. Bulent Aydoğan and Assistant Prof. Dr. Murat Sürücü for their guidance, supporting me and supervising this research, and providing me the necessary research materials at the University of Chicago, Department of Radiation and Cellular Oncology and the University of Illinois at the Chicago Radiation Oncology and Loyola University Radiation Oncology Clinics during my stay in USA. Special thanks go to Dr. Sang Cho of the MD Anderson Cancer Center for sharing a copy of their phase space data for using our system and Dr. Reft Chester of the University of Chicago Radiation and Cellular Oncology for helping me the selection of TLDs for this study.

Sincere thanks to my colleague Research Assistant, Gizem Z. Portakal for her helps during the writing period of this thesis. I would like to give thanks to those whose names are not mentioned here for their direct / indirect assistance towards fulfilling this PhD program. I appreciate a lot to the Cukurova University supported this PhD thesis under the contract number BAPFEF2011D23.

Finally, many thanks go to my husband (Ismet Ozan Sarıgül), my mother and mother in law (Neriman Can and Serpil Sarıgül), my father and father in law (Hacı Can and Kazim Sarıgül) and my son (Alp Sarıgül) for their patience, support and providing me to feel powerful myself during this study.

CONTENTS **PAGE**

LIST OF TABLE **PAGE**

LIST OF FIGURE **PAGE**

LIST OF GRAPHICS **PAGE**

LIST OF ABBREVIATONS

3D-CRT : Three Dimensional Conformal Radiation Therapy

521icru.pegs4 : ICRU cross section data file for low energy photon beam

700icru.pegs4 : ICRU cross section data file for high energy photon beam

A : Mass number

AE : Default value for ECUT

Al_2O_3:C : Carbon doped aluminum oxide

AP : Default value for PCUT

B-G : Bragg-Gray

BEAMnrc : Monte Carlo simulation system for modelling radiotherapy sources

BSF : Back Scatter Factor

CaF_2:Mn : Manganese doped calcium fluoride

CaF_2:Dy : Dysprosium doped calcium fluoride

$CaSO_4$:Dy : Dysprosium doped calcium sulfate

CAX : Central Axis

CB : Conduction Band

CC : Charge Carriers

CLT : Central Limit Theorem

CPE : Charged-Particle Equilibrium

CSDA : Continuous Slowing Down Approximation

D : Absorbed Dose

D_{med} : Dose to medium

D_{cav} : Dose to cavity

DBS : Directional Bremsstarhlung Splitting

DNA : Deoxyribonucleic Acid

DOSXYZnrc : *EGSnrc* user interface for 3D absorbed dose calculations

EE : Electronic Equilibrium

EBM : Electronic Band Model

ECUT : Electron Cutoff Energy

ECUTIN : Electron Cut off In Mev Total Energy

EGS : Electron Gamma Shower

EGSnrc : Monte Carlo code used to simulate charged particle and photon transport

ESTEPE : Max fractional energy loss electron per step

FB : Forbidden Band

KERMA : Kinetic Energy Released in the Medium

LET : Linear energy transfer

LINAC : Linear accelerator

LiF : Lithium Fluoride

LiF: Mg,Ti : Magnesium And Titanium Doped Lithium Fluoride

LiF: Mg,Cu,P : Magnesium, Copper and Phosphor Doped Lithium Fluoride

LLN : Law of Large Numbers

MC : Monte Carlo

MU : Monitor unit

NIST : National Institute of Standards and Technology

OAR : Organs at Risk

SAD : Source to Axis Distance

SAR : Scatter Air Ratio

SDD : Source to Detector Distance

SMR : Scatter-maximum ratio

SPR : Scatter-phantom ratio

SSD : Source to Surface Distance

ICRP : International Commission on Radiological Protection

ICRU : International Commission for Radiation Units

IMRT : Intensity Modulated Radiotherapy

OF : Output Factor

OMEGA : Ottawa Madison Electron Gamma Algorithm

PCUT : Photon Cut off Energy

PCUTIN : Photon Cut off In Mev Total Energy

PDD : Percentage Depth Dose

PMT : Photomultiplier Tube

RE : Radiation Equilibrium

RC : Recombination Centers

RT : Radiotherapy

T : Traps

TAR : Tissue-air ratio

TCPE : Transient charged particle equilibrium

TERMA : Total Energy Released per unit Mass

TL : Thermoluminescence

TLD : Thermoluminescence Dosimetry

TMR : Tissue-Maximum Ratio

TPS : Treatment Planning System

TPR : Tissue Phantom Ratio

TTP : Time Temperature Profile

VB : Valence Band

Z : Atomic number

Z_{etkin} : Effective atomic number

cs : Compton Scattering

pe : Photoelectric

pp : Pair Production

rs : Rayleigh Scattering

S_c : Collimator scatter factor

$S_{c,p}$: Total scatter factor

S_p : Phantom scatter factor

pr : Photonuclear interaction

β : Beta

γ : Gamma

m : Linear attenuation coefficient

b : Order of Kinetic

eV : Electron Volt

E : Energy

Gy	: Gray
k	: Boltzmann constant
K	: Kelvin
s	: Frequency factor
Sv	: Sievert
I	: TL intensity
ρ	: Density
μ/ρ	: mass attenuation coefficient
S_{col}/ρ	: mass collisional stopping power
R_{CSDA}	: Range of continuous slowing down approximation
dE_{tr}	: The sum of the initial kinetic energies of all the charged ionizing particles
K_{col}	: Collision KERMA
K_{rad}	: Radiative KERMA
h	: Planck's constant
μ_{tr}	: Energy transfer coefficient
μ_{en}	: Energy absorption coefficient
d	: A parameter related to the cavity size that approaches unity for small cavities and zero for large ones
β	: The effective mass attenuation coefficient of the electrons penetrating in the cavity material
m	: Mass
Φ	: Particle fluence
Φ_E	: Particle fluence spectrum
Ψ	: Energy fluence
Ψ_E	: Energy fluence spectrum
E_{tr}	: Energy transferred to charged particles in photon interactions
E_{en}	: Energy deposited by charged particles released in photon interactions
g	: Radiative fraction
K	: Kerma
Kc	: Collision kerma

Kr	: Radiative kerma
Q	: Charge
Wair	: Mean energy required to produce an ion pair in air
e	: Electron charge

1. INTRODUCTION

1.1. Overview of Thesis

This thesis have six parts and appendices. The thesis is organized as follows;

Section 1 is the first part. It gives information about thesis aim, research problem and the role of dosimetry in radiation therapy. Besides it has background information about radiotherapy, external photon beam, common experimental quantities and review of literature. The review of literature has two group. The first one in deal with "Cavity Theory and its Monte Carlo Applications" and second one in deal with "Conversion of Dose to Medium to Dose to Water and its Monte Carlo Applications".

Section 2 starts with the cavity theories are described and showed equations which related to Bragg-Gray, Spencer Attix and Burlin cavity theories.

Section 3 includes general information about Monte Carlo Technique, photon and electron transports and BEAMnrc software. BEAMnrc software which is used in the presented study is built around the core EGSnrc Monte Carlo simulation software for radiation transport. This section describes how we can create phantom and calculate the dose distribution in phantom design using DOSXYZnrc software.

Section 4 starts with Luminescence and Thermoluminescence theorem follows it. To test the Burlin Cavity theory for inhomogeneity medium, the LiF:Mg,Ti (TLD-100) dosimeter is chosen. In this section, the TLD-100's properties and its sensitivity, dose response, photon energy dependence and annealing procedure are described. The materials and methods are summarized and the phantom designs are shown in this section. In method section, we described two methodology. First one is proposed in order to convert the experimental dose to TLD to dose to medium ($(f)_{water}^{TLD}$). Second one is proposed to dose to medium verification using dose to water calibration ($(f)_{water}^{medium}$).

Section 5 presents theoretical, Monte Carlo and experimental results for $(f)^{TLD}_{medium}$. With this results this chapter shows the accuracy of Burlin general cavity theory in bone and lung heterogeneities when measuring dose using TLDs of various thicknesses. Section 5 shows that $(f)^{medium}_{water}$ conversion factor can be used for dose to medium conversion especially in high Z materials such as bone.

Section 6 presents the conclusion.

1.1.1. Thesis Aim

Several studies have evaluated the applicability of Burlin cavity theory with measurements and/or Monte Carlo simulations, however, bone and lung heterogeneities, which are most relevant for dose verification in medical physics, have not been studied yet. The aim of this study is to examine the general cavity theory for Magnesium and Titanium doped Lithium Fluoride TLDs of varying thicknesses in bone and lung heterogeneities with experimental, theoretical, and Monte Carlo simulations for 6 MV photon beam. The validity of theory was tested with measurements and MC simulations and a framework for converting dose to TLD to dose to medium was presented.

1.1.2. Inhomogeneity and It's main problem

The human body consists of a variety of tissues and cavities with different physical and radiological properties. Most important among these, from a radiation dosimetry perspective, are tissues and cavities that are radiologically different from water, including lungs, oral cavities, teeth, nasal passages, sinuses, and bones. These inhomogeneities perturb the unit density dose calculations. The dose perturbation varies depending on the location of the point of calculation with respect to the inhomogeneity, the lateral dimensions of the inhomogeneity and the photon field size. In this research, we investigated only slab type inhomogeneities whose lateral dimensions are much larger than the photon field size.

Radiation therapy treatments require intensive planning and calculation to determine the dose deposited by a treatment or single beam. While estimating the dose deposite to a homogenous medium is not overly complicated, the introduction into such a medium of inhomogeneities makes this task much more complicated. Heterogeneities have been shown to have a profound effect on dose distributions as well as dose calculations for use in radiation therapy (Carrasco et al., 2004; Carrasco et al., 2007). Both high-Z and low-density materials, such as bone and lung, respectively, have been examined, since the effect of such materials often have the largest effect on dose calculation.

The major phenomena occur in the low-density inhomogeneities comparing to tissue, such an increase in the transmission caused by the low-density materials and the decrease of the number of interactions inside the lung. The classical dose calculations algorithms implemented un the treatment planning systems do not usually account for the decrease in the interaction coefficient and therefore usually over predict the dose inside of the lung.

In the case of high-density material, the opposite effects occur in the bone in comparison to lung due to the material densities and electron densities: the interactions coefficient inside the bone is increased and, the transmission coefficient is decreased. The classical dose calculations algorithms implemented un the treatment planning systems do not usually account for the increase in the interaction coefficient and therefore usually under predict the dose inside of the bone.

Currently there are several different methods to calculate dose around heterogeneities. Methods such as equivalent TARs (ETAR) and effective path lengths provide dose estimates but do not account for scatter. More advanced methods such as pencil beam convolution, superposition convolution and collapsed cone superposition convolution provide much more accurate calculation methods for dose distributions in an inhomogeneous material by using scatter kernels to describe the motion and energy deposition of secondary charged particles in the medium (Carrasco et al., 2004; Knoss et al., 2006). The most accurate methods of determining dose theoretically in an inhomogeneous medium is Monte Carlo modeling. MC methods require significant computational

resources because a large number (millions to billions) of events called histories or particles must be simulated in order to obtain a reasonably precise estimate of the quantities of interest (e.g., dose). In the case of radiation incident on a medium, this simulation can be compared to experimental results obtained by measurement with dosimeters such as TLDs. It is very common to use the first order approach to convert dose in TLD to dose in medium using stopping power ratios as suggested by Bragg-Gray cavity theory. This approach provides correct results for lung, however, not for bone.

1.1.3. The Role of Dosimetry in Radiation Therapy

Radiation dosimetry is the branch of science that attempts to quantitatively relate specific measurements made in a radiation field to physical, chemical, and/or biological changes that the radiation would produce in a target. Dosimetry is essential for quantifying the incidence of various biological changes as a function of the amount of radiation received (dose–effect relationships), for comparing different experiments, for monitoring the radiation exposure of individuals, and for surveillance of the environment (Turner, 2004). In medicine, radiation dosimetry is an important and regulatory requirement for surveillance of radiation workers in radiology, nuclear medicine and radiation oncology. The dosimetry is also predominantly required for quality assurance (QA) (i.e. precise estimation of delivered dose to patient) in external beam radiation therapy and brachytherapy as well.

In radiotherapy, the aim of dosimetry is to make sure that the dose to the target volume is as prescribed while minimizing the dose to the surrounding normal tissue. To obtain them, the absorbed dose distribution in a phantom must be known. Furthermore, while the measurement of absorbed dose distribution in a phantom is essential in treatment planning, the ultimate check on the absorbed dose delivered to the patient can only be made by *in vivo* absorbed dose measurements. Therefore, the applications of clinical dosimetry in radiation therapy may be divided into groups according to the used method: i) *in vivo* measurements in the region of interest or at

some convenient region of the body, ii) *in vitro* measurements, and iii) measurements in anatomical phantoms. The most useful phantom for absorbed dose measurements both in radiation therapy and diagnostic radiology is one which is designed, as far as it is, to simulate the structure of the human body (Aschan, 1999).

In clinical practice, the main detectors used for dosimetry are ionization chambers and semiconductors. Ionization chambers are commonly used for phantom measurements because of their accuracy and practicality (IAEA Rpt: 277, 1987; Svensson et al., 1986), but for *in vivo* measurements they are not frequently used because of the high voltage applied and the cables attached to the chamber. Semiconductor diodes are routinely used for absorbed dose measurements of clinical studies. These measurements make use of the advantages of semiconductors, such as ease of handling and the dose determination in real time (Rikner et al., 1987; Nilsson et al., 1988; Li et al., 1995). Thermoluminescent dosimeters (TLD), are semiconductor, are widely needed for a small, free standing dosimeter.

TLDs have been the passive detector of choice, able to perform in vivo dosimetry as well as remote QA checks of radiation therapy delivery systems. In addition to ‘‘in vivo’’ dosimetry, applications for TL dosimetry are: assessment of superficial tumour dose, electron field assessments for treatment of superficial lesions, total skin electron treatments for verifications of skin dose to whole body electron treatments, assessment of thyroid dose, and absorbed dose distribution in gynecological cancer treatments (Rivera, 2012). Thermoluminescent dosimetry is suggested as a good tool for total skin electron irradiation (TSEI) treatments in in vivo dosimetry, because it provides a useful quality assurance tool to verify the delivered dose to the skin (ICRU RPT.398, 2000). TLDs are also applied worldwide for personal dosimetry. For personal dosimetry, Lithium (Li) based TLDs are used as they are tissue-equivalent. In addition to radiation protection and quality assurance, TLD is commonly (Kron, 1999) used in the context of medical research.

1.2. Background Information

1.2.1. Radiotherapy

Radiation therapy is used as an important part of the cancer treatment process in addition to the chemotherapy and the surgery. It is required that the ionizing radiation projected into the malignant cells conform the tumor as closely as possible in terms of sufficient dose while delivering minimum possible dose to normal tissue during the treatment. Single or double strand breaks occur in the DNA molecule of a cell due to the result of the radiation interacting with base pairs (Metcalfe, 2008).

Treatments that are based on 3-D anatomic information and the beams are shaped to the contour of the three dimensional tumor volume referred to as three-dimensional conformal radiation therapy (3D-CRT). Treatments are delivered by radiation beams with uniform intensity across the field and wedges or compensators are used to modify the intensity profile to get more uniform dose distributions. Additionally, nonuniform fluence is delivered to the patient by any given position of the beam with using intensity modulated radiation therapy (IMRT). The main idea is to deliver the dose to the patient from a number of different directions or continuous arcs with optimized nonuniform fluence called “inverse planning” (Khan, 2003).

A typical radiation therapy can be stated respectively as diagnosis and 3D imaging, target volume and organ localization, beam selection, beam shaping, dose calculation & optimization, biological modeling & prescription, treatment verification and delivery. The chain is shown in Figure 1.1. The most difficult step to verify in the 3D-CRT process is dose calculation and optimization. To determine the absorbed dose to the tumor and surrounding tissue to avoid exceeding tolerance levels for the organs at risk (OAR) while achieving local control of the tumor is the main and an important part of the radiotherapy (Mayles, 2007). Due to the patient setup, organ motion and variations in machine output, dose monitoring during the treatment this is the most apparent way to verify the treatment plan (Cherry, 2009).

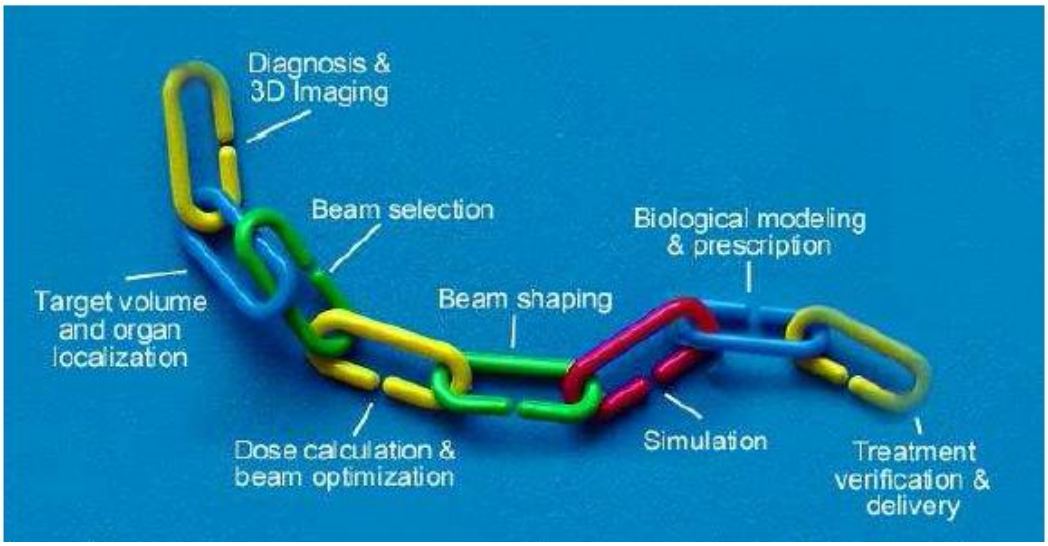

Figure 1.1. The chain of events that occurs during a typical radiation therapy treatment. The overall accuracy of the treatment is limited by the weakest link in the chain (Babcock, 2009).

1.2.2. Energy Deposition

To verify the treatment plan including dose calculation and optimization, it is of great importance to understand the energy deposition process. Treatment planning is in a state of rapid development with several new and powerful mathematical methods under implementation for clinical routine. For instance, accurate analytical, experimental and Monte Carlo generated energy deposition kernels are taken into use to describe the energy transport by secondary particles released by the primary photons (Eklöf, 1990). To predict the energy deposition of the incident radiation beam is difficult due to the contribution of uncertainties during the treatment.

The energy deposition in tissue from photon beams is a two-step process. (1) The TERMA step: An incident photon imparts its energy to the medium via an interaction. The resulting energy is carried away by resulting electrons and photons. (2) The DOSE step: Electrons undergo large number of collisions depositing energy locally along their paths. Bremsstrahlung x-rays are also generated which carry energy away to other interaction sites (Babcock, 2009).

A) Photon Interactions: TERMA (Total Energy Released per unit Mass)

The initial photon interactions within tissue are characterized by a linear attenuation coefficient (μ) which is the probability of a photon interacting per unit distance. This probability depends on:

- the incident photon energy, E (MeV);
- the tissue density, ρ (g/cm^3);
- the effective atomic number (Z) of tissue (AAPM Rp. 85, 2004).

The combined effect of these interactions is characterized by a mass attenuation coefficient (μ/ρ) which represents the probability of a photon being attenuated per unit mass thickness. As is known, the ensemble of photons reaching a point in the patient is characterized by an energy fluence (MeV.cm^{-2}). For a given energy fluence, the total energy released per unit mass, TERMA is given as the product of the total mass attenuation coefficient and the energy fluence (Ψ) at a point.

$$TERMA = \left(\frac{\mu}{\rho}\right).\Psi \qquad (1.1)$$

B) Charged Particle Interactions: The DOSE Step

When energy is transferred to the medium, the liberated charged particles continue to travel and interact within the medium. These interactions including photoelectrons, Compton electrons, and electron-positron pairs, which are ultimately responsible for energy deposition in tissue. This is called dose step.

The charged particles are launched with a spectrum of initial energies and directions. These particles then slow down through multiple Coulomb collisions, which deposit energy locally along the particle track and occasional radiative bremsstrahlung events that carry energy remotely away from the charged particle

track (AAPM Rp. 85, 2004). The amount of energy deposited along the particle path is dictated by the mass collisional stopping power (S_{col}/ρ) which is relevant to the energy loss per unit pathlength (in g/cm^2).

In reality, charged particles lose a variable burst of energy for each interaction, but this statistical energy straggling is often ignored and "continuous slowing down approximation (CSDA)" is assumed. This allows for the determination of a unique "CSDA range (R_{CSDA})" of the charged particle (AAPM Rp. 85, 2004). It depends on the particle's kinetic energy, mass as well as charge, and on the composition of the absorbing medium.

$$R_{CSDA} = \int_0^E \left(\frac{S_{col}}{\rho}\right) . dE \qquad (1.2)$$

Where E is energy. The CSDA range (typically cm^2/g) is a calculated quantity that represents the mean path length along the particle's trajectory and not necessarily the depth of penetration in a defined direction in the absorbing medium (Podgorsak, 2010).

1.2.3. Charged Particle Equilibrium

The concepts of radiation equilibrium (RE) and charged-particle equilibrium (CPE) are useful in radiological physics as a means of relating certain basic quantities (Attix, 2004). Basically, CPE occurs when the energy of electrons upon entering and leaving a small dosimetric volume are equal. For situations in which charged particle equilibrium has been established, absorbed dose is the product of the energy fluence and the mass energy absorption coefficient.

For CPE to occur, Fano (Fano, 1954) shows that two conditions must be met. First, the radiation field that generates primary electrons should be uniform throughout the volume of the detector. Second, the detector size should be significantly smaller than the average range of the electrons being generated. In these situations, the energy dependent response of a detector is governed by the ratio of the

mass collision-stopping power of the detector material to that of the medium in which dose is required, for instance mass- collision stopping power of air to that of water for an ionization chamber measurement (Sidek, 2010).

These conditions are easily met for an ionization chamber in a megavoltage beam due to the fact that the range of electrons in air is many times greater than the size of an air cavity. However in solid-state dosimeters, the range of electrons in the medium of the detector is very much less than that in air and as a consequence a more complicated analysis is required (Saeedi et al., 2004). We can say the CPE especially is not fully provided in a number of situation:

- when radiation beams enter the body, for example in the interface between different density materials such as in lung and bone surface;
- also where the beam-size is smaller than the electron range as in stereotactic radiosurgery, for example when electrons generated from megavoltage beams travel several cm and significant numbers of electrons diffuse out of the field which are not replaced (Yin et al., 2004; Saeedi et al., 2004).

1.2.4. Absorbed Dose and KERMA

Absorbed dose is a non-stochastic quantity applicable to both indirectly and directly ionizing radiations. As mentioned above, for indirectly ionizing radiations, energy is imparted to matter in a two-step process. In the first step (resulting in terma), the indirectly ionizing radiation transfers energy as kinetic energy to secondary charged particles. In the second step, these charged particles transfer some of their kinetic energy to the medium (resulting in absorbed dose) and lose some of their energy in the form of radiative losses (bremsstrahlung, annihilation in flight). That means not all the kinetic energy of the electrons will be absorbed. Some energy will be irradiated in the form of Bremmstrahlung radiation. For photon beams of energy typical for medical applications less than a few percent is irradiated in the form of Bremmstrahlung (Lemoigne and Caner, 2009). The absorbed dose D can

best be defined in terms of the related stochastic quantity energy imparted *e* (Attix, 2004).

Absorbed dose is the energy absorbed per unit mass at a given point. The fundamental dose quantity given by;

$$D = \frac{de}{dm} \tag{1.3}$$

where *de* is the mean energy imparted to matter of mass *dm* by ionizing radiation. The unit is the joule per kilogram (J kg^{-1}) and is given the special name gray (Gy). The dimensions and units of absorbed dose are the same as those used for Kinetic Energy Released in the Medium (KERMA).

The quantity KERMA is defined as "the quotient of dE_{tr} by *dm*, where dE_{tr} is the sum of the initial kinetic energies of all the charged ionizing particles (electron and positrons) in material of mass *dm*" (Khan, 2003). For a photon beam traversing a medium, KERMA at a point is directly proportional to the photon fluence and mass energy transfer coefficient:

$$KERMA = \frac{dE_{tr}}{dm} = \frac{\mu_{tr}}{\rho} . \Psi \tag{1.4}$$

The total KERMA is therefore usually divided into two components: the collision KERMA K_{col} and the radiative KERMA K_{rad}.

- The collision KERMA K_{col} is that part of KERMA that leads to the production of electrons that dissipate their energy as ionization in or near the electron tracks in the medium, and is the result of Coulomb force interactions with atomic electrons. Thus the collision KERMA is the expectation value of the net energy transferred to charged particles per unit mass at the point of interest, excluding both the radiative energy loss and energy passed from one charged particle to another.

- The radiative KERMA K_{rad} is that part of KERMA that leads to the production of radiative photons as the secondary charged particles slowdown and interact in the medium. These interactions most prominently are bremsstrahlung as a result of Coulomb field interactions between the charged particle and the atomic nuclei, but can also result from annihilation in flight (Podgorsak, 2010).

The total KERMA is thus given by the following:

$$KERMA = K_{col} + K_{rad} \tag{1.5}$$

Since radiative photons mostly escape from the volume of interest, one relates absorbed dose usually to collision KERMA. When CPE conditions occur and bremsstrahlung interactions are negligible, the final dose at a point is equal to the collision KERMA at that point. In reality, charged particle equilibrium is never fully achieved due to beam attenuation and divergence. However, if the spread of the beam is large enough to create a near equilibrium state in directions perpendicular to the axis of the beam, the attenuation simply causes an exponential shift in the dose at depth as a function of KERMA. In general, the ratio of dose and collision kerma is often denoted as:

$$\beta = \frac{D}{K_{col}} \tag{1.6}$$

β is the ratio of absorbed dose to collision KERMA. If radiative photons escape the volume of interest, an assumption is made that β≈1. The Figure 1.2 shows relationship between absorbed dose (Dose) and collision KERMA for a megavoltage photon beam.

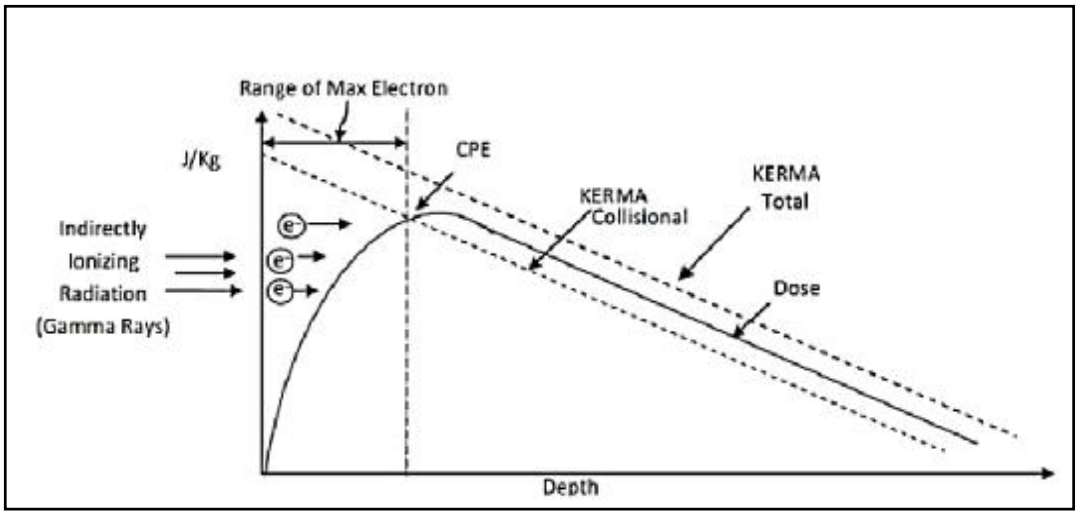

Figure 1.2. Collision KERMA, absorbed dose and CPE diagram as a function of depth (Kaiser, 2010).

1.2.4.1. External Photon Beam Calculation and Common Experimental Quantities

A photon beam propagating through air or a vacuum is governed by the inverse square law; a photon beam propagating through a phantom or patient, on the other hand, is affected not only by the inverse square law but also by the attenuation and scattering of the photon beam inside the phantom or patient. These three effects make the dose deposition in a phantom or patient a complicated process and its determination a complex task (Podgorsak, 2010).

Photon beams for radiation therapy are always contaminated with electrons. The fluence of these electrons varies with several parameters like field size, photon energy, material placed in the beam, etc. In the following section is about of the most commonly used quantities defined for points along the central axis of a photon beam. These are classified into those quantities:

- express the depth penetration characteristics of beams,
- attempt to separate scatter dose from primary dose and
- describe the output of the clinical accelerator.

1.2.4.1.(1). The Depth Penetration Characteristics of Beams

Percentage Depth Dose (PDD), Tissue Phantom Ratio (TPR) and Tissue Maximum Ratio (TMR) have been widely used.

PDD at a point in water is defined as the ratio of absorbed dose at that point to the absorbed dose at the depth of maximum build-up along the central axis. PDD data are impractical for direct reconstruction of dose distributions since they depend on the source to surface distance (SSD).

TPR is defined as the ratio of the total absorbed dose on the central axis at depth to that at a point also on the central axis and at the same distance from the source but with the surface of the phantom moved so that the point is at a specified reference depth (Karzmark et al., 1965). The TPR was defined to comply with recommendations that x-ray beams should be calibrated at a reference depth in a phantom (Ahnesjo and Aspradakis, 1999).

TMR which expresses the dose at some depth in a water equivalent medium (the Tissue) relative to the dose at the same distance from the radiation source, but with just the minimum amount of material overlying the point that would be necessary to provide full buildup (the Maximum). This ratio is referred to as the "Tissue Maximum Ratio". It is strictly a better choice for dosimetry systems (Dutreix et al., 1966).

1.2.4.1.(2). Attempt To Separate Scatter Dose from Primary Dose

Tissue Air Ratio (TAR), Scatter Primary Ratio (SPR), Scatter Air Ratio (SAR), Scatter Maximum Ratios (SMR) have been widely used.

TAR is based on the concept of primary dose. The ratio of the dose at a point in tissue to the dose at that same point in air is known as the Tissue-Air Ratio. The TAR was originally introduced to simplify dose calculations in rotational radiotherapy, but its use was subsequently expanded to isocentric irradiations with multiple stationary fields. In rotational radiotherapy, the radiation source moves in a circle around the axis of rotation, which is usually inside the tumor. During the

rotation around the patient the SSD varies with the patient contour; however, the SAD remains constant (Podgorsak, 2010).

SPR is a general name for quantities defined as ratios of scatter versus primary dose at a point. A related quantity is scatter air ratio (SAR) describing the absorbed dose originating from scattered radiation, and is practically derived by subtracting the extrapolated value for zero-area field TAR from finite field TAR (Ahnesjo and Aspradakis, 1999).

SMR, like the SAR, is quantity designed specifically for the calculation of scattered dose in a medium. The ratio of the scattered dose at a given point in phantom to the effective primary dose at the same point at the reference depth of maximum dose (Khan, 2003).

1.2.4.1.(3). The Output of the Clinical Accelerator

Collimator Scatter Factor (S_c), Phantom Scatter Factor (S_p) and Total Scatter Factor ($S_{c,p}$)have been used. Those are used for dose calculation.

S_c may be defined as the ratio of the output in air for a given field to that for a reference field. On the other hand for a given photon beam at a given SSD, the dose rate at a certain depth *d* in a phantom depends on the field size. The output factor (OF) is defined as the ratio of the dose for any field size AxA cm^2 to the dose for a reference field at the same source to surface distance, and at the same depth *d* in a slab phantom (Abou-Haidar, 2012).

S_p takes into account the change in scatter radiation originating in the phantom at a reference depth as the field size is changed. S_p may be as the ratio of the dose rate for a given field at a reference depth to the dose rate at the same depth for the reference field size (Khan, 2003).

$S_{c,p}(r)$ is the total scatter factor (output factor) (Korhonen, 2009) contains both the collimator and phantom scatter and when divided by S_c yields S_p at a given field size. Sc,p(A) is measured with constant SSD and SDD, and the detector is located at a certain calibration depth z_{cal} in a phantom.

In this section, the backscatter factor (BSF) would be appropriate to mention. BSF is the ratio of the dose rate with a scattering medium to the dose rate at the same point without a scattering medium at the level of maximum equilibrium.

In the light of this information, the accelerator calculations are made. The accelerator calculation has two techniques (Khan, 2003):

- SSD technique
- Isocentric technique (Source to Axis Distance, SAD)

These technique helps to the calculation of dose in the medium.

As mentioned above, within the patient's (or phantom) dose is almost impossible to measure directly. Because of this reason, in order to measure the absorbed dose in a medium and for the detection of the aforementioned parameters, it is necessary to introduce a radiation sensitive device (dosimeter or detector) into the medium. Generally, the sensitive medium of the dosimeter will not be of the same material as the medium in which it is embedded. Cavity theory relates the absorbed dose in the dosimeter's sensitive medium (cavity) to the absorbed dose in the surrounding medium containing the cavity. Ion chambers, TLDs are good example for the cavity.

Review of Literature

a) **Cavity Theory and Monte Carlo Applications:** Burlin et al. (1969) derived the expression for electron beams from the general cavity theory of ionization for photons. They assumed that an electron beam did not generate secondary electrons inside the cavity and there were no photons either to accounted for them, i.e. $\left(\frac{\mu_{en}}{\rho}\right)^{c}_{m}$ was zero and hence the second term in eqn 2.3 was eliminated to give the expression for electron beams. Almond and McCray (1970) modified the expression derived by Burlin et al.(1969) by taking into consideration the production of secondary electrons inside the cavity. They

were unable to find agreement between their theory and experiments for low Z media but found it satisfactory for high Z media such as lead. Almond and McCray tested their expression for several low Z TLD dosimeters and found excellent agreement with their experimental data but did not report any data for high Z media.

There have been relatively few experimental examinations of the validity of the Burlin cavity theory. For example, Chan and Burlin (1970) used Perspex dosimeters in cavity volumes ranging from 0.1 cm x 1 cm x 4 cm to 8 cm x 8 cm x 8 cm, and with wall media from Z = 6 to 82. The ^{60}Co δ-ray source was used in cylindrical geometry surrounding the dosimeter array. Ilic-Popovic (1971) used a gelatin-anthracene luminescence degradation dosimeter in layers from 0.002 to 0.024 g cm^{-2} in a Pb wall medium. This range of thicknesses does not extend to large enough sizes to test the Burlin theory for the ^{6o}Co δ-rays used. Ehrlich's (1971) experiment was the first to provide a useful test of Burlin's theory for a monodirectional δ-ray beam. She employed CaF_2: Mn thermoluminescent dosemeters in the form of plates 6 mm x 6 mm x 0.5 mm in size, stacking up to seven plates together. Thus her cavities had thicknesses ranging from 0.16 to 1.12 g cm^{-2}, irradiated perpendicularly by ^{6o}Co δ-rays and wall media had Z values of 6 to 82. Bertilsson (1974) also made use of a plane-parallel δ-ray beam, but from a ^{137}Cs teletherapy unit. LiF-Teflon discs were employed as TL dosimeters in stacks from 0.004 to 0.093 g cm^{-2}, enclosed in wall media from Z= 6 to 82.

Turner and Anderson (1973) investigated the relative energy response of LiF dosimeters (1 x 1 x 6 mm) at high photon energies of 30, 50, and 65 MV. They found from the experiment a decrease of about 10% in response at these energies when compared with ^{60}Co δ rays and invoked Burlin's cavity theory for photons to explain their findings.

Mansfield and Suntharalingam (1975) measured the energy response of loose TLD-100 powder for 5 to 45 MeV electrons and photon beams of 4, 32, and 45 MV relative to ^{60}Co δ rays and found no relative energy response. However, they made

use of thin layers of TLD-100 powder in Lucite phantoms, thus approaching a Bragg-Gray cavity at these energies.

Paliwal and Almond (1975) compared both the Burlin et al. (1969) and the Almond and McCray (1970) expressions. They showed for a very small cavity size which did not perturb the medium generated electron spectrum both the Burlin et al. and the Almond and McCray expressions were reduced to the Bragg-Gray equation. However, for large cavity sizes Burlin et al. overestimated the attenuation by the cavity and underestimated the build-up as there was no (1 - d) term in it to taked into account this phenomenon.

Lowe (1979) studied the application of cavity theory to the dosimetry of electron fields. He formed a comparison between mass stopping power ratios and the response of LiF relative to cobalt-60 radiation for various electron energies as calculated by Lowe and by Paliwal and Almond (1975). As a conclusion, the experimental results of Paliwal and Almond, which at first seemed to verify Almond and McCray's (1970) theory, were in disagreement with his calculations.

Ogunleye, Attix and Paliwal (1980) carried out Cobalt-60 gamma-ray absorbed dose measurements using LiF thermoluminescent (TL) dosimeters to obtain additional insight into cavity theory as applied to dosimeters of a size intermediate relative to the range of secondary electrons. Stacks of dosimeters (0.4 mm x3 mmx3 mm, hot-pressed LiF TLD-100) were surrounded by homogeneous LiF, polystyrene, aluminum, copper or lead. The absorbed dose in the stack (0.1 to 0.7 g cm^{-2} thick) was derived from TL readings of the individual dosemeters, and was compared with calculations based on the Burlin cavity theory. A relatively strong asymmetry in the experimental absorbed-dose distribution was found between the front, rear and middle dosimeters of the stack, especially when lead was the surrounding medium. Cavity theory showed good agreement with their experimental results obtained in polystyrene, while theory tends to overestimate the dose in the LiF dosimeters enclosed in AI, Cu, and Pb. Their normalization had been made to the measurements in the homogeneous (all LiF) holder, as the response throughout each dosimeter stack in that case was constant within experimental error. The theory was modified to

make it more applicable to the dose at the center of the stack. For lead, this clearly agreed more closely with experimental results than did the conventional theory.

Horowitz and Dubi (1982) proposed a simple modification of the well-known Burlin general cavity theory for photons. Their proposal distinguishes between the mean cavity path length for secondaries produced in the wall (g) and the mean cavity path length for secondaries produced in the cavity (g'). In general g' is less than g. In a more recent paper, Horowitz et al. (1983) compared the Burlin model, the modified Burlin model and the experimental data of Ogunleye et al. (1980).

Kearsley (1984) derived a new general cavity theory for photons, it taked into account secondary electron scattering at the cavity boundaries. The proposed model was used to calculate both the effective stopping power ratio as well as the dose distribution inside plane parallel cavities of lithium fluoride surrounded by aluminum, copper or lead. The gamma source was ^{6o}Co. A comparison was made between the proposed model, the well-known Burlin model, and experimental data. As a conclusion, the model reduced to the familiar Burlin form.

Mobit et al. (1997) performed the EGS4 Monte Carlo simulations to examine general cavity theory for a number of TLD cavity materials irradiated in megavoltage photon and electron beams. Their results indicated that the Burlin exponential attenuation technique could overestimate the dose contribution from photon interactions in a 1 mm thick LiF cavity by up to 100% compared with the Monte Carlo results for LiF TLDs irradiated in a water or Perspex phantom. However their results were disagree between Monte Carlo simulations and Burlin's theory of 6 and 12% for LiF TLDs irradiated in copper and lead phantoms respectively.

Miljanic et al. (1997) irradiated several types of thermoluminescent dosimeters (LiF:Mg,Ti, Al_2O_3:Mg,Y and CaF_2:Mn) at different depths in a water phantom placed at a distance of 2.5 m from a panoramic ^{60}Co source. Detectors were encapsulated in Plexiglas holders with a wall thickness of 0.5 cm. They compared the experimental data with the predictions of the general cavity theory for gamma ray spectra at different depths of water. The suitability of parameters of the cavity theory proposed by different authors was evaluated in the analysis of the experimental

results. They showed that there was no need for any modification to the original and simple Burlin expression.

Edy (2012) generalized the Kearsley´s general cavity theory for photons beams by regarding electron backscattering not only on the interfaces between medium and detector (cavity) but on each of the planes within the cavity. The Kearsley theory was improved for photon beams so the model generated small changes in the Kearsley model. It was therefore concluded that Kearsley theory did not need any improvement and represent the general expression for cavity theory for photon beams. The fitting between experiment and theory for Co-60 was remarkable. The relative bad agreement of Kearsley´s theory in fitting the experimental data for MV photons energy beams.

b) **Conversion of dose to medium to dose to water and the Monte Carlo Method:** Haraldsson et al. (2003) calculated the dose distribution to a phantom having a cylindrical air cavity containing a tube by Monte Carlo methods and the results were compared with data from a treatment planning system (TPS) to evaluate the accuracy of the TLD measurements. They used DOSXYZnrc Monte Carlo code to define phantom and calculations were performed with 6MV fields, with the TLD tube placed at different positions within the cylindrical air cavity. Differences between the Monte Carlo and the TPS calculations of the absorbed dose to the TLD tube were found to be small for an open symmetrical field. With respect to their comparisons, it should be possible to compare TLD measurements in a water equivalent tube placed in an air cavity to absorbed doses calculated using the studied pencil beam based TPS, at least as long as no half-beam field through the air cavity was used.

Siebers et al. (2000) developed conversion that was a method to convert dose to the medium to dose to water by applying Bragg–Gray cavity theory. The dose ratio for 6 and 18 MV photon beams was determined by computing the average stopping power ratio for the primary electron spectrum in the transport media. They

determined the dose ratio for 6 and 18 MV photon beams by computing the average stopping power ratio for the primary electron spectrum in the transport media. As a conclusion, they found that for a given photon beam energy, the same material dependent conversion factor can be used throughout the treatment field since the dose converting stopping power ratio does not depend upon the position in the field.

Dogan et al. (2006) studied to assess the differences between dose–volume indices for D_m and D_w MC-calculated IMRT plans. They performed MC calculations using an EGS4-based system. Converting D_m (absorbed dose to medium) to D_w (absorbed dose to water) for MC-based calculations was accomplished as a post-MC calculation process. D_w and D_m results for target and critical structures were evaluated using the dose–volume-based indices. They indicated that D_m to D_w conversion should be available when comparing MC-calculated treatment for consistency.

Ma and Li (2011) discussed the differences in dose calculated using water with different electron densities and that calculated for different biological media and the clinical issues on dose specification including dose prescription and plan evaluation using dose to water and dose to medium. They demonstrated that conventional photon dose calculation algorithms compute doses similar to those simulated by Monte Carlo using water with different electron densities.

Paganetti (2009) described the development of a formalism to convert dose to medium into dose to water for proton fields when simulating the dose with Monte Carlo techniques. The conversion was based on relative stopping power but also considers energy transferred via nuclear interactions. The influence of different interaction mechanisms of proton beams (electromagnetic versus nuclear) was demonstrated. As a result, he developed a formalism to convert dose to medium into dose to water for proton beam dose calculations and he found that the difference between the three methods (one of them is his method) was within 1% in most cases when analyzing doses to contoured structures.

2. CAVITY THEORIES

2.1. Dosimetry in Inhomogeneous Media

The presence of a dosimeter in a medium perturbs the charged particle fluence in the medium unless the dosimeter and the medium are identical with respect to atomic composition and density. The response of a dosimeter, therefore, depends on the geometry, construction and the surrounding medium. The main problem in radiation dosimetry is the determination of the absorbed dose in a medium material *m* of atomic number Z, at a point (small volume) where a detector (different material *c* with other atomic number Z) has been placed. This detector is called "cavity" and its response is proportional to the absorbed dose in the cavity material (Edy, 2012). Various cavity theories for photon beams have been developed, which depend on the size of the cavity; for example, the Bragg-Gray and Spencer Attix theories for small cavities and the Burlin theory for cavities of intermediate sizes. These various cavity theories are briefly reviewed in the next section.

2.2. Bragg-Gray Cavity Theory

Bragg–Gray (B-G) cavity theory is the first cavity theory developed to provide a relation between the absorbed dose in a dosimeter and the absorbed dose in the medium containing the dosimeter. The B-G cavity is a cavity (detector) so small that, when inserted into a medium, it does not disturb the fluence of charged particles existing in the medium (Carlsson, 2001). The fluence of Φ (charged particles/cm^2) of identical charged particles of kinetic energy passes through an interface between two different media, "c"(cavity) and "m"(medium), as shown in Figure 2.1.

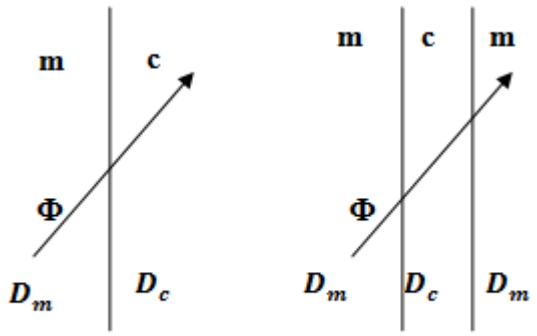

Figure 2.1: a) A fluence Φ of charged particle is shown crossing an interface between media "m" and "c". Assuming Φ to be continuous across the boundary, the dose ratio $\frac{D_m}{D_c}$ equals to corresponding ratio of mass collision stopping powers. b) A fluence Φ of charged particles passes through a thin layer of medium "c" sandwiched between regions containing medium med. Assuming Φ to be continuous across layer "c" and both interfaces, the dose ratio $\frac{D_m}{D_c}$ is again equal to the corresponding ratio of mass collision stopping powers.

Basically two conditions must be met for the B-G cavity theory to be applicable. They are firstly, the cavity must be small when compared with the range of charged particles incident on it so that its presence does not perturb the fluence of charged particles in the medium; and secondly, the absorbed dose in the cavity is deposited solely by charged particles crossing it and is not modified by the presence of the cavity, thus, photon interactions in the cavity are assumed negligible and therefore ignored.

The result of (first) condition is that the electron fluences are equal to the equilibrium fluence established in the surrounding medium. This condition can only be valid in regions of CPE or transient CPE (TCPE). In addition, the presence of a cavity always causes some degree of fluence perturbation that requires the introduction of a fluence perturbation correction factor. Condition (second) implies that all electrons depositing the dose inside the cavity are produced outside the cavity and completely cross the cavity. Therefore, no secondary electrons are produced inside the cavity and no electrons stop within the cavity.

Under these two conditions, according to the B-G cavity theory, the dose to the medium D_m is related to the dose in the cavity D_c as follows:

$$D_m = D_c \left(\frac{\bar{S}}{\rho}\right)_c^m \tag{2.1}$$

where $\left(\frac{\bar{S}}{\rho}\right)_c^m$ is the ratio of the average unrestricted mass collisional stopping powers for the medium to that for the cavity. The use of unrestricted stopping powers rules out the production of secondary charged particles (or delta electrons) in the cavity and the medium (Podgorsak, 2010).

However, the B-G cavity theory is not in agreement with experimental measurements, especially with cavity walls of high atomic number. The stopping power in the B-G theory is evaluated under the assumption of the CSDA. However, the delta rays produced by the knock-on electron-electron collisions enhance the equilibrium spectrum of lower energy electrons crossing the cavity. The resulting spectrum is further enhanced at low energies as the energy of the electrons is decreased because the Møller differential cross section for delta ray production is inversely proportional to the square of the energy. Since the stopping power increases with decreasing electron energy, the presence of additional low energy electrons in the equilibrium spectrum as a result of delta ray production, would give a larger stopping power ratio for low and high Z media than that evaluated using the CSDA assumption (Haider, 1995).

The next development of cavity ionization theory was due to Laurence (Laurence, 1937), who also employed the continuous energy loss model for electrons. He took account of the energy dependence of the stopping power, which necessitated giving more detailed consideration to the electron energy spectrum generated in the wall. Both Gray's and Laurence's treatment predicted that the ionization per gram of gas is independent of the cavity size (or the gas pressure). Many investigations have studied the original B-G theory and have suggested

modifications. The most important of these are those of Spencer and Attix (Spencer and Attix, 1955) and Burlin (Burlin, 1966).

2.3. Spencer-Attix Cavity Theory

The B-G cavity theory does not take into account the creation of secondary (delta) electrons generated as a result of hard collisions in the slowing down of the primary electrons in the sensitive volume of the dosimeter (Podgorsak, 2010). L. V. Spencer rederived the Bragg-Gray theory by a different (though more restricted) approach that is valuable in providing additional insight into the nature of the spectrum when charged particle equilibrium exists (Spencer and Attix, 1955). The Spencer-Attix theory assumes CPE and the absence of bremsstahlung generation in addition to the two B-G conditions. The equilibrium electron spectrum is divided into two groups in the Spencer-Attix theory.

a. Electrons that have energy T>Δ and are able to cross the cavity. These electrons can therefore transport energy into the cavity

b. Electrons that have energy T<Δ and are not able to cross the cavity as they deposit their energy locally. These electrons are therefore not able to transport energy into the cavity (Haider, 1995).

According to the Spencer Attix theory; the dose delivered to the medium D_m is given by the expression:

$$D_m = D_c \left(\frac{L}{\rho}\right)_c^m = D_{cav} \frac{\int_{\Delta}^{E_{max}} \phi_E \left(\frac{L(\Delta)}{\rho}\right)_m dE + \phi_E(\Delta)\left(\frac{S(\Delta)}{\rho}\right)_m \Delta}{\int_{\Delta}^{E_{max}} \phi_E \left(\frac{L(\Delta)}{\rho}\right)_c dE + \phi_E(\Delta)\left(\frac{S(\Delta)}{\rho}\right)_c \Delta} \quad (2.2)$$

Where,

$\left(\frac{L}{\rho}\right)_c^m$ = the ratio of the mean restricted mass collisional stopping powers from the medium to the cavity

ϕ_E = the fluence of particles with energy E,

$\left(\frac{L(\Delta)}{\rho}\right)$ = the restricted mass collision stopping power evaluated at energy E = Δ,

$\left(\frac{S(\Delta)}{\rho}\right)$ = the unrestricted mass collision stopping power evaluated at energy E = Δ

and

Δ = the lowest energy for which secondary electrons are considered part of the electron spectrum.

An assumption is made that all secondary electrons with energy below Δ are absorbed on the spot and is considered in the restricted stopping power, $\left(\frac{L(\Delta)}{\rho}\right)$ (Sidek, 2010).

Consequently, the difference between the Bragg-Gray theory and Spencer-Attix theory becomes negligible, as the cavity size is increased, due to the diminishing influence of delta rays. In the presented study the Burlin cavity theory was used.

2.4. Burlin Cavity Theory

Burlin proposed a general cavity theory to include all cavity sizes. The size of the cavity is defined relative to the range of the electrons. Figure 2.2 illustrates this cavity size transition. The cavities containing medium “c” is considered: small (satisfying the B-G conditions), medium and large compared to the ranges of the secondary electrons. The absorbed dose in the small cavity (Figure 2.2) is delivered almost entirely by “crossers”, ie., secondary electrons completely traversing the cavity, such as e_1. The average absorbed dose in the medium sized cavity in Figure 2.2 is delivered partly by crossers, but also by “starters” like e_2 that originate in the cavity and stop in the wall (m), stoppers (e_3) starting in the wall and terminating in the cavity, and insiders (e_4) that start and stop within the cavity (Attix, 1986).

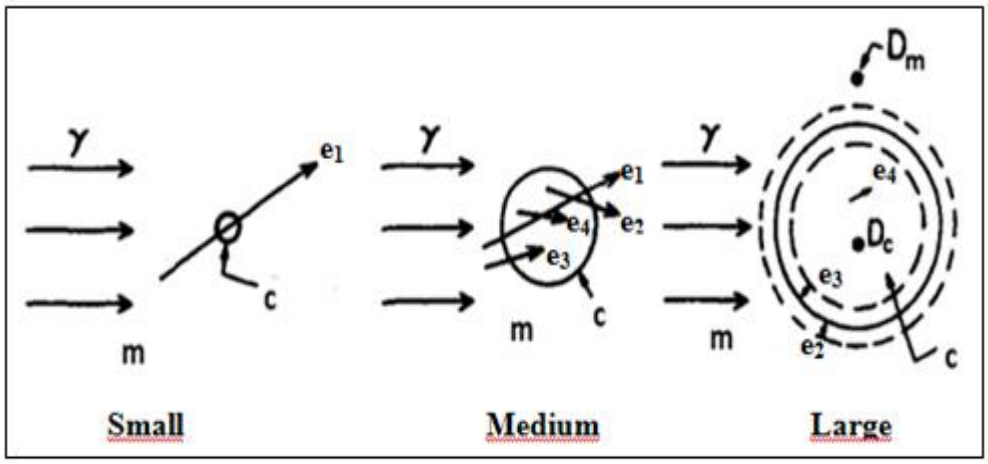

Figure 2.2. The cavity size transition in Burlin Theory (Attix, 1986).

Burlin's cavity theory that would bridge the gap between small cavities for which the Bragg-Gray or Spencer theory could be applied and very large cavities for which the wall influence is negligible.

When the cavity size is large, the electron spectrum within the cavity is determined by the cavity material itself. The ratio of the absorbed dose in the cavity to the absorbed dose in the medium is given by

$$f(T,\Delta) = \frac{D_c}{D_m} = \left(\frac{\mu_{en}}{\rho}\right)^c_m \tag{2.3}$$

where $\left(\frac{\mu_{en}}{\rho}\right)^c_m$ is the mean mass energy absorption coefficient of the cavity to that of the medium. Cavities whose dimensions are comparable to the range of electrons entering the cavity have a spectrum within the cavity that is partially determined by the medium and partially determined by the cavity material (Haider, 1995).

Burlin combined both conditions and gave the equation:

$$f = \frac{D_c}{D_m} = dS^c_m + (1-d)\left(\frac{\mu_{en}}{\rho}\right)^c_m \tag{2.4}$$

where;

D_c = the average dose delivered to the sensitive volume of cavity

d = a parameter related to the cavity size that approaches unity for small cavities and zero for large ones

S_m^c = the mean ratio of mass collision stopping powers for the medium to cavity and

$\left(\frac{\mu_{en}}{\rho}\right)_m^c$ = the mean ratio of the mass–energy absorption coefficients for the cavity and the medium.

The above equation is not valid for doses in the medium adjacent to the cavity as the dose is perturbed by the presence of the cavity.

The Burlin theory effectively requires that:

- The surrounding medium and the cavity medium be homogeneous;
- A homogeneous photon field exist everywhere throughout the medium and the cavity;
- CPE exist at all points in the medium and the cavity that are further than the maximum electron range from the cavity boundary;
- The equilibrium spectra of secondary electrons generated in the medium and the cavity be the same (Podgorsak, 2010).

Burlin provided a method in order to treat this quantitatively and estimate the weighting parameter d in his theory; he used the experimental results of the beta-ray absorption properties. The weighting factor *d*, varies between unity for small (or Bragg–Gray) cavity and zero for large cavity. The parameter d is the dose contribution resulting from photon interactions in the phantom material and accounts for the attenuation of electrons across the cavity (Burlin, 1966; Paliwal and Almond, 1975). It is, indeed, the fraction of secondary electrons generated in the medium that is absorbed in the cavity and can be calculated using the following formula (Mobit et al., 1997);

$$d \equiv \frac{\phi_m}{\phi_m^c} = \frac{\int_0^g \phi_m^c e^{-\beta' dl}}{\int_0^g \phi_m^c dl} = \frac{1 - e^{-\beta g}}{\beta g} \qquad (2.5)$$

$$1 - d \equiv \frac{\phi_c}{\phi_c^e} = \frac{\int_0^g \phi_c^e (1 - e^{-\beta l}) dl}{\int_0^g \phi_c^e dl} = \frac{\beta g + e^{-\beta g} - 1}{\beta g} \quad (2.6)$$

where, Φ_m^e and Φ_m are the electron fluence in medium with and without electron equilibrium conditions satisfied, respectively; 1-d in Equation 2.6 represents the dose component resulting from photon interactions in the cavity and can be formulated as the ratio of the electron fluence created by the photons in the cavity to that created under electronic equilibrium (Silva, 1989).The distance (cm) of any point in the cavity from the wall is given by l; g is the average path length of electrons across the cavity or the mean cord length; and β is the effective mass attenuation coefficient of the electrons penetrating in the cavity material that were originated from the wall (Ogunleye et al, 1980; Janssens et al, 1974).

Table 2.1. Equations for calculating mean cord length or average path length, g. t=thickness of cavity; V=cavity volume; S=surface area of the cavity.

	Ogunleye (Ogunleye et al., 1980)	Horowitz (Horowitz and Dubi, 1982)	Burlin (Burlin and Chan, 1969)
g	$1.2t$	$1.54t$	$\frac{4V}{S}$

Table 2.2. Equations for calculating effective mass attenuation coefficient of the electrons, β.

	Formula	***Material***
Evans (Evans, 1955)	$\beta_E = \frac{17}{(T_{max})^{1.14}}$	Aluminum
Paliwal and Almond (Paliwal and Almond, 1975)	$\beta_{PA} = \frac{14}{(T_{max})^{1.09}}$	LiF
Burlin (Burlin, 1966)	$\beta_B = \frac{16}{(T_{max} - 0 \cdot 036)^{14}}$	Air
Lovinger (Loevinger, 1956)	$\beta_L = \frac{18 \cdot 6}{(T_{max} - 0.036)^{1.37}}$	Soft tissue
Chan and Burlin (Burlin and Chan, 1969)	$e^{(-\beta_{CB}R)} = 0.01$	Ferrous Sulfate
Janssens (Janssens, 1974)	$e^{(-\beta_I R)} - 0.04$	Air

Various methods of calculating g (Table 2.1) and β parameters (Table 2.2) were proposed but there is no good agreement amongst them (Miljanic and Komor, 1997). Some investigators defined β using the extrapolated range (R) of maximum energy (T_{max}) of the electron spectrum from a head-on Compton collision of a photon with energy $h\nu$ whereas majority suggested the use T_{max} itself (Attix, 2004):

$$T_{max} = \frac{2(h\nu)^2}{2h\nu + 0.511\ MeV} \tag{2.7}$$

3. MONTE CARLO MODELING OF THE DOSE DISTRIBUTION AND PHOTON SPECTRA

3.1. Basic Principles of Monte Carlo Technique

Monte Carlo (MC) Simulation, is a statistical technique, is based on randomly happening events so that the outcome is not always absolute. The Monte Carlo method is firmly based on two mathematical theorems: the law of large numbers (LLN) and the central limit theorem (CLT) (Rice, 1995).

Basically;

The LLN is:

Suppose X_1, X_2…is a sequence of independent identically distributed (iid) random variables with E $[X_i] = \mu$. Then

$$\lim_{n \to \infty} \frac{X_1 + X_2 + \cdots + X_n}{n} = \mu \tag{3.1}$$

with probability one.

The CLT is:

Suppose X_1, X_2…is a sequence of independent identically distributed (iid) random variables with E $[X_i] = \mu$ and Var $[X_i] = \sigma^2$. Then $n \longrightarrow \infty$,

$$\frac{X_1 + X_2 + \cdots + X_n - n\mu}{\sqrt{n}\sigma} \rightarrow N(0,1) \tag{3.2}$$

The converge $\longrightarrow$ means

$$\lim_{n \to \infty} P\left(\frac{X_1 + X_2 + \cdots + X_n - n\mu}{\sqrt{n}\sigma} \leq y\right) = \Phi(y) \tag{3.3}$$

for every y € R.

The main components of the Monte Carlo method are (Walter, 2008):

- the probability distribution functions describing the physical system;
- the random number generator which is a source of uniformly distributed random numbers;
- the sampling rule which is a recommendation for sampling the probability distribution function;
- the variance reduction techniques, which are methods for reduction of the computational time for Monte Carlo simulation
- the scoring (or tallying), which represents the outcomes of the interest quantities.

In radiation sciences, the Monte Carlo method provides a numerical solution for the Boltzmann transport equation that directly employs the fundamental physics laws for electron-atom and photon-atom interactions in order to reproduce the individual particle tracks (Mayles, 2007; Walters et al., 2009).

The Monte Carlo simulation technique for neutral particles is based upon single-collision physics. Each photon or neutron is followed between each individual collision and the applicable geometrical boundary crossings. For electrons, this technique becomes computationally unfeasible because electrons will interact approximately 10^5 times for the same energy loss vs. a photon. The majority of electron Monte Carlo simulation codes in use today use techniques that are based upon the condensed history method of Berger. The basic feature of this method for electron transport is to group the many interactions of the actual physical transport into a single step of a condensed random walk (Demarco, 2002). Briefly, the Monte Carlo simulation codes has the ability to simulate the tracks of individual particals by sampling appropriate quantities from the main probability distributions of the individual physical processes. Quantities such as particle fluence, energy spectrum and absorbed dose distribution can be calculated by simulating a large number of particle histories.

A large number (millions to billions) of events called histories or particles must be simulated in order to obtain a reasonably precise estimate of the quantities of interest (e.g., dose), so MC methods require significant computational resources.

This chapter describes the major components of a MC code for the transport of photons and electrons in matter, cross sections, algorithms and dose calculations. The mass attenuation coefficient, the effective atomic number and the electron density are basic quantities required in determining the penetration of X-ray and photons in matter (Gowda, 2004).

3.2. Issues for Monte Carlo Algorithms

3.2.1. Photon Transport Processes, Cross Sections and Algorithms

For radiation transport problems, the computational model includes geometry and material specifications. Every computer code contains a database of experimentally obtained quantities, known as cross sections that determine the probability of a particle interacting with the medium through which it is transported (Zaidi, 2003). Photon and electron interactions with matter is different from each other. Unlike charged particles, photons are electrically neutral and do not steadily lose energy as they penetrate matter. Instead, the photons can travel some distance before interacting with an atom. How far a given photon will penetrate is governed statistically by a probability of interaction per unit distance traveled, which depends on the specific medium traversed and on the photon energy. The probability of occurrence of a certain kind of interaction depends on its relative contribution to the total cross section.

The cross section is perhaps the most quoted parameter in the fields of particle physics and radiation measurement because it gives a direct measure of what to expect from a certain beam of particles when it interacts with a material (Ahmed, 2007). We can define it mathematically:

$$\frac{d\sigma}{d\Omega}(E,\Omega) = \frac{1}{\phi}\frac{dN}{d\Omega} \tag{3.4}$$

where σ is total cross section, Φ is a flux (number of particles per unit area per unit time) and (dN) is the average number of particles per unit time that get scattered per unit solid angle (dΩ).

The differential cross section can be integrated to evaluate the total cross section at a certain energy (differential cross section is a function of energy of the incident particles), that is

$$\sigma(E) = \int \frac{d\sigma}{d\Omega} d\Omega \tag{3.5}$$

There are five types of interactions with matter by photons which must be considered in radiological physics. They are Compton scattering (cs), photoelectric effect (pe), pair production (pp), Rayleigh (coherent) scattering (rs) and photonuclear reactions (pr). Among these interactions, the first three are the most important because they lead to energy transfer to secondary electrons. Total cross section can be calculated by:

$$\sigma_{total} = \sigma = \sigma_{pe} + \sigma_{cs} + \sigma_{pp} + \sigma_{rs} + \sigma_{pr} \tag{3.6}$$

In this section, the interactions are explained basically if someone wants to obtain much more information about these, Attix's (Attix, 1986) and Podgorsak' (Podgorsak, 2010) s books are good reference.

3.2.1.1. Compton Scattering

The Compton scattering is known as incoherent scattering. It is an inelastic scattering of a photon by a free charged particle, usually an electron. The electron is ejected from its orbital position and the photon loses energy because of the interaction but continues to travel through the material along an altered path. Energy

and momentum are conserved in this process. The energy shift depends on the angle of scattering and not on the nature of the scattering medium. The Klein-Nishina treatment of the Compton differential cross-section is based on the assumption that the electron is free and stationary. This assumption is invalid for energies below 100 keV, where binding effects and Doppler broadening becomes significant.

3.2.1.2. Photoelectric Effect

The incident photon transfers all of its energy to an atomic electron. The photon gets absorbed and the electron is ejected with a vacancy left behind. The process is called the photoelectric effect (or photoelectric emission or photoemission), a material that can exhibit this phenomena is said to be photo emissive, and the ejected electrons are called photoelectrons; but there is nothing that would distinguish them from other electrons. The photoelectric effect occurs with photons having energies from a few electron volts to over 1 MeV. The direction of the photoelectron can be sampled from the Sauter distribution.

3.2.1.3. Pair Production

Pair production refers to the creation of an elementary particle and its antiparticle. It occurs when a photon is absorbed in the field of the nucleus and results in an electron-positron pair. Pair production is a direct conversion of radiant energy to matter. For pair production the photon energy must be at least equivalent to 0.51 million electron volts (MeV) of energy. To produce two electrons, the threshold energy for this interaction is 1.02 MeV.

3.2.1.4. Rayleigh Scattering

Rayleigh scattering is an elastic interaction hence the photon is merely redirected through a small angle with no energy loss. Besides it is known as coherent scattering because the photon is scattered by the combined action of the whole atom.

Rayleigh scattering contributes nothing to kerma or dose, since no energy is given to any charged particle, nor is any ionization or excitation produced (Attix, 1986).

3.2.1.5. Photonuclear Interactions

Photonuclear reaction occurs in a direct interaction between an energetic photon and an absorber nucleus causing nuclear disintegration. The nucleus is excited by an energetic photon and becomes radioactive. The process results in the emission of a proton in a (γ, p) reaction or a neutron in a (γ,n) reaction. The (γ,p) reaction has little contribution to dose in radiotherapy applications. The two description of ‘’photonuclear disintegration and ‘’nuclear photoelectric effect’’ are used for this interactions.

3.2.1.6. Linear Attenuation Coefficient

When a photon passes through matter, any of the four interaction processes (photoelectric effect (pe), Compton scattering (cs), pair production (pp), Rayleigh scattering (rs)) may occur. But in calculations we don’t consider contributions from photonuclear reactions and from less probable interactions such as Delbruck scattering and nuclear resonance scattering (Seltzer, 1993).

The probability of a photon of a given energy E undergoing absorption or scattering when traversing a layer of material Z can be expressed quantitatively in terms of a total linear attenuation coefficient μ (cm^{-1}) which is dependent on the material’s density, ρ ($g\ cm^{-3}$) :

$$\mu = \mu_{pe} + \mu_{cs} + \mu_{pp} + \mu_{rs} \tag{3.7}$$

where μ_{pe}, μ_{cs}, μ_{pp}, μ_{rs} are the linear attenuation coefficients for photoelectric effect, Compton scattering, pair production and Rayleigh scattering respectively. The inverse of μ is the mean free path λ, in units of length:

$$\lambda = \frac{1}{\mu} \tag{3.8}$$

It indicates the average distance traveled by a particle before undergoing an interaction. The exponential nature of photon attenuation can be represented by:

$$N = N_0 e^{-\mu x} \tag{3.9}$$

where N is the number of photons transmitted through a medium of thickness x with N_0 incident photons.

We can also write the total linear attenuation coefficient μ in terms of total cross section as follow;

$$\mu = \sigma N = \sigma \frac{\rho N_A}{A} \tag{3.10}$$

where A is the atomic weight of the material, N_A is the Avagadro's number.

3.2.1.7. Mass Attenuation Coefficient

The total linear attenuation coefficient determines how quickly or slowly a certain photon beam will attenuate while passing through a material. It is a function not only of the photon energy but also of the type and density of the material (Ahmed, 2007). Typically, the total mass attenuation coefficient μ_m, is in units of cm^2 /g, can be written as:

$$\mu_m = \frac{\mu}{\rho} = \frac{\mu_{pe}}{\rho} + \frac{\mu_{cs}}{\rho} + \frac{\mu_{pp}}{\rho} + \frac{\mu_{rs}}{\rho} \tag{3.11}$$

where ρ is a material density and μ is the lineer attenuation coefficient. We can also write this equation as follows:

$$\mu_m = \frac{\sigma N}{\rho} = \sigma \frac{N_A}{A} \tag{3.12}$$

3.2.1.8. Mass Energy-Transfer Coefficient

This coefficient determines the total energy given to electrons produced by the photon. The mass energy transfer coefficient $\frac{\mu_{tr}}{\rho}$ is defined as

$$\mu_{tr} = \frac{N_A}{\mu A} \sum_j f_j \sigma_j = f \frac{\mu}{\rho} \tag{3.13}$$

Where f_j is the average fraction of the photon energy E that is transferred to kinetic energy of charged particles in interaction of type j, and f is the weighted average of f_j. To see the energy-transfer fractions, look at Seltzer's (Seltzer, 1993) paper and Attix's (Attix, 1986) book.

3.2.1.9. Mass Energy-Absorption Coefficient

The mass energy-absorption coefficient is related to the mass energy-transfer coefficient by

$$\frac{\mu_{en}}{\rho} = \frac{\mu_{tr}}{\rho}(1 - g) \tag{3.14}$$

in which grepresents the average fraction of secondary-electron energy that is lost in radiative interactions, that is, bremsstrahlung production and (for positrons) inflight annihilation. For low values of *Z* and hν, g approaches zero and $\frac{\mu_{en}}{\rho} \simeq \frac{\mu_{tr}}{\rho}$ (Attix, 1986). The following Figure 3.1 is a reference for this comment:

Photon Energy	*WATER*			*LEAD*		
(MeV)	$\frac{\mu}{\rho}$	$\frac{\mu_{tr}}{\rho}$	$\frac{\mu_{en}}{\rho}$	$\frac{\mu}{\rho}$	$\frac{\mu_{tr}}{\rho}$	$\frac{\mu_{en}}{\rho}$
0.01	5.33	4.95	4.95	131.	126.	126.
0.1	0.171	0.0255	0.0255	5.55	2.16	2.16
1.0	0.0708	0.0311	0.0310	0.0710	0.0389	0.0379
10.0	0.0222	0.0163	0.0157	0.0497	0.0418	0.0325
100.0	0.0173	0.0167	0.0122	0.0931	0.0918	0.0323

Figure 3.1. Mass attenuation, mass energy transfer and mass energy absoption coefficients (cm^2/g) for Photons in Water and Lead (Turner, 2004).

3.2.1.10. Effects of Atomic Number and Energy

The mass attenuation coefficient depends on atomic number and energy. The table 3.1 shows how the mass attenuation coefficient dependence on Z, low photon energy (le) and high photon energy (he). The data come from the National Institute of Standarts and Technology (Nist).

The mass energy absorption coefficient depends on atomic number, and thus the collision KERMA is changed locally within the absorbing material as previously. This is well known in kilovoltage x-ray dosimetry, where a factor is used to calculate the enhancement of dose to bone for a given photon fluence, assuming CPE. For megavoltage photons, the collision KERMA can similarly be used to estimate the local dose, but only if a sufficient mass of material allows CPE or at least TCPE to become established. This is generally not the case for small bone regions and such dose enhancement calculations based on collision KERMA ratios are not very accurate in bone (AAPM Rp. 85, 2004).

Table 3.1. Mass attenuation coefficient dependence on atomic number (AAPM Rp. 85, 2004):

Atomic Number, Z	Mass Attenuation coefficient at low photon energy, (cm^2/g) $\left(\frac{\mu}{\rho}\right)_{le}$	Mass Attenuation coefficient at high photon energy, (cm^2/g) $\left(\frac{\mu}{\rho}\right)_{he}$	(cm^2/g) $\left(\frac{\mu}{\rho}\right)_{le} - \left(\frac{\mu}{\rho}\right)_{he}$
1 to 10	3.5 (for Z=1) to 1.9 (for Z=10) decreases with increasing Z	2.7 (for Z=1) to 1.4 (for Z=10) decreases with increasing Z	0.8 (for Z=1) 0.5 (for Z=10)
11 to 60	0.9 (for Z=11) to 7.0 (for Z=60) increases with increasing Z	0.4 (for Z=11) to 1.0 (for Z=60) increases with increasing Z	0.5 (for Z=11) 6.0 (for Z=60)
61 to 92	7.1 (for Z =61) to 4.4 (for Z=92) decreases with increasing Z	0.1 (for Z =61) to 2.8 (for Z=92) increases with increasing Z	7.0 (for Z =61) 1.6 (for Z=92)

The photoelectric absorption coefficient is directly proportional to Z^5 and inversely proportional to $(h\nu)^3$ on average. Photoelectric absorption is most pronounced in high- Z materials and for low-energy photons (less than 0.5 MeV) (Martin, 2006). The cross section increases rapidly with decreasing energy, except around the absorption edges.

The Compton interaction coefficient decreases with increasing energy so it is inversely proportional to E and it is almost independent of atomic number which is determined by electron density. The mass attenuation coefficient is slightly higher for hydrogenous or low-Z materials due to higher electron densities. For photon with energies above 100 KeV (Martin, 2006), Compton interactions in soft tissue are much important than either the photoelectric or pair production interactions.

The pair production absorption coefficient increases rapidly with energy above the 1.022 MeV threshold and varies approximately as Z^2 (Martin, 2006). The contribution of triplet production is higher for low-Z materials. Since triplet production accounts for less than 10% of the total cross section for low-Z materials and less than 1% for high-Z materials, most Monte Carlo codes do not model this interaction explicitly. Instead, it is simulated as a pair production event by including the contribution of triplet production in the pair production cross section (Cecen, 2008).

Rayleigh scattering has more practical importance at low energies, partly because the scattering angle is greater. The atomic cross section for Rayleigh scattering is proportional to Z and inversely proportional to $(h\nu)^2$ on average. Rayleigh scattering contributes only a few percent or less of the narrow-beam attenuation coefficient (Attix, 1986).

3.2.1.11. Effective Atomic Number

The atomic number, *Z,* is a ubiquitous parameter in atomic and nuclear physics where it occurs in almost any formula. For a complex medium, the effective atomic number, Z_{eff}, is in some cases a convenient parameter for representing X-ray and gamma ray interactions, e.g. in designs of radiation shielding or in calculations of absorbed dose in radiotherapy. However, as stated by Hine, a single number cannot represent the effective atomic number of a material, which is composed of several elements (Manohara, 2008). The effective atomic number is important for predicting how photons interact with a substance, as certain types of photon interactions depend on the atomic number. To calculate Z_{eff}, there are various formulas which are derived from first principles using photon interaction cross sections of the constituent atoms. The Manohara and et al. has shown basic and practical formulas, examples for Z_{eff} .

3.2.1.12. Density Effect

As the electron energy increases, the electric fields of orbital electrons at an increasing distance are felt because of relativistic effect (Lorrentz contraction of the coulomb field). This causes an increase in the mass collision stopping power known as the realistic rise. However, the effect of distant electrons is screened by intervening atoms, which reduces the slope of the relativistic rise from what it otherwise would be. For higher density materials,the number of intervening atoms is greater and thus the reduction in slope is larger. Therefore, as energy increases, the increase in stopping power with energy is smaller for higher density materials; hence the name density effect (Metcalfe et al, 2007). The Sternheimer's paper (Sternheimer, 1952) has how to calculate the density effect.

3.2.1.13. Algorithm of Photon Transport

A general algorithm of photon transport is best described by Rogers and Bielajew (Rogers et al, 1990). Figure 3.2 shows a diagram for a Monte Carlo simulation of photon transport. This is a simplified algorithm that involves only one medium, and it does not account for the tracking of secondary electrons. At the start of a new history, the parameters of a photon, such as its energy, position and direction, are sampled and pushed onto a stack. Its energy is first compared with a user-defined cutoff value. Then distance to next interaction is determined. The word DETERMINE in the diagram means that the quantities of interest are found by sampling from the relevant probability distribution using one or more random numbers.

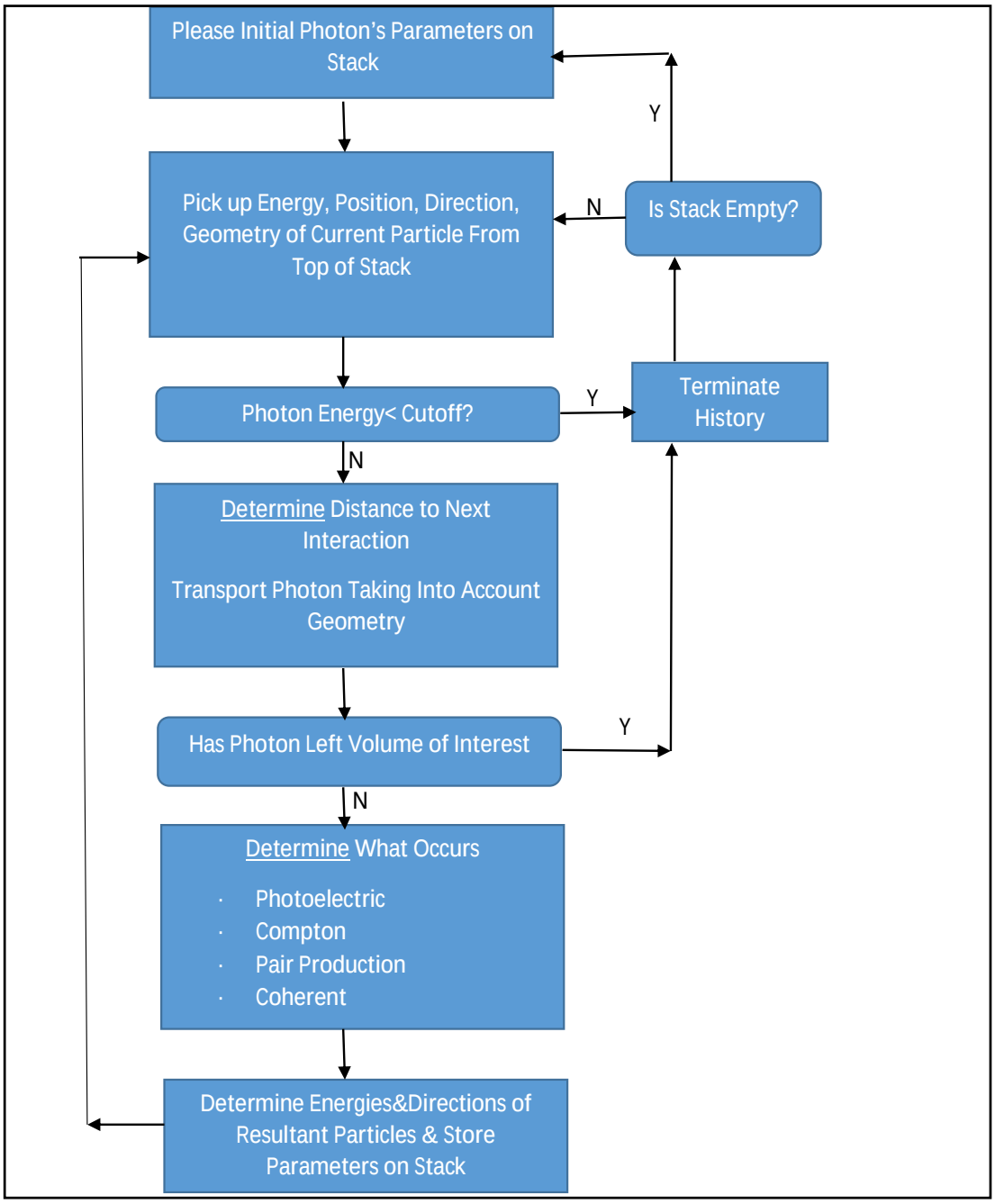

Figure 3.2. Photon Transport Algorithm (Y means "yes", N means "No").

Given a photon at a definite location with given momentum and energy, the first step is to sample the free path lengths (λ) until the next interaction site. The mean free path is a distance between two points in a medium that a photon travels without interaction.

The mean free path can be calculated by equation 3.8

$$\lambda = \frac{-\ln(R_1)}{\sigma} \tag{3.15}$$

where R_1 is a random number uniformly distributed between 0 and 1. In the energy rangeof radiation therapy σ is calculated as a sum of three relevant contributions (Fippel, 2006; Metcalfe et al., 2007).

$$\sigma = \sigma_{pe} + \sigma_{cs} + \sigma_{pp} \tag{3.16}$$

These parameters are different for photons of different energy. They also depend on the atomic composition of the material, i.e. they change from voxel to voxel. A second random number R_2 from interval [0, σ] can be used to sample the interaction type. We simulate a photoelectric absorption if R_2 is less than σ_{pe}. We simulate a Compton interaction if R_2 is larger than σ_{pe} but less than the sum of σ_{pe} plus σ_{cs}; otherwise, we simulate a pair production process (Fippel, 2006; Metcalfe et al., 2007).

After the interaction, the parameters of the resultant particles will be sampled and pushed onto the stack so that they can be processed in turn. The procedure continues until the stack becomes empty. At that point, a new particle history can start.

3.2.2. Electron Transport and Algorithms

The Monte Carlo simulation of electron transport should be included in all calculations where the complete electromagnetic cascade is to be considered. The interest in medical radiation physics focuses on situations where electron ranges are comparable with the dimensions or the spatial resolution of the problem to be solved, or the contribution of bremsstrahlung plays a significant role in the amount of energy locally deposited or transported away (Zaidi, 2003). The electron's path is divided into sub-steps, and the energy loss and angular deflection at each step are averaged over many individual collisions. Electron transport algorithms are often categorized

as Class I or II models based on how the energy of the primary electron is related to the energy lost in individual interactions. Since the electron transport may be crucial to some radiotherapy calculations, further investigation and validation of electron transport algorithms is needed (Fraass, 2003).

3.2.2.1. Stopping Power Ratio

Electrons lose their energy in many interactions with the matter. The track of high energy electrons can be quite long, even up to few centimeters. Therefore, it is natural that for electrons the interesting value is the rate of energy loss per unit of length of its path through matter. Because the loss of energy is a stochastic process, we are interested in the expectation value of the energy loss. This value is called stopping power (Lemoigne, 2009). Stopping powers are widely used in radiation dosimetry, but they are rarely measured and must be calculated from theory. For electrons and positrons the Bethe theory is used to calculate stopping powers. Basically the stopping power is;

$$S = \frac{dE}{dx}\left[\frac{MeV}{cm}\right] \tag{3.17}$$

In dosimetry it is better to measure the distance in units related to the density of the absorber. Then the stopping power becomes the mass stopping power (Lemoigne, 2009).

$$\frac{S}{\rho} = \frac{dE}{\rho dx}\left[\frac{MeV.cm^2}{g}\right] \tag{3.18}$$

When one is interested in the fate of the energy lost by the charged particle, stopping power may be subdivided into “collision stopping power’’ and “radiative stopping power. ” The former is the rate of energy loss resulting from the sum of the soft and hard collisions, which are conventionally referred to as “collision

interactions (Attix, 1986). Detailed information about these are in Attix's book (Attix, 1986). In this study we deal with mass collision stopping power.

For dosimetry, the mass collision stopping power is often represented by a special case called the restricted mass stopping power, L/ρ, which excludes energy losses above a certain value (say 100keV). This is because in calculating the energy deposited at a point, the energy given to δ rays that have a significant range should not be counted, as it will be deposited remotely. The actual energy deposited at a point is, therefore, defined as the energy transferred by secondary electrons in collisional energy losses less than a specific value Δ. The linear restricted stopping power, L_{Δ}, also known as the linear energy transfer (LET), is therefore the energy loss per unit pathlenght in restriction placed on the energy loss, ($L_{\Delta}=L_{\infty}=S_{coll}$). The restricted mass stopping power is therefore defined as

$$\left(\frac{S}{\rho}\right)\text{coll} = \left(\frac{L}{\rho}\right)\Delta \tag{3.19}$$

Where the parameter Δ is typically set at 100 keV because the range of electrons in water at such a low energy is less than 1 mm (Metcalfe et al., 2007).

3.3. Variance Reduction Technique

The accuracy of MC dose calculation is mainly restricted by the statistical noise (in each voxel is determined by the number of simulated particle histories), because the influence of MC model approximations should be much smaller. This statistical noise can be decreased by a larger number of histories leading to longer calculation times as well. However, there are a variety of methods to decrease the statistical fluctuations of MC calculations without increasing the number of particle histories. These techniques are known as variance reduction (Kawrakow and Fippel, 2000).

There are a few variance reduction techniques which are particle splitting, Russian Roulette, range rejection, and source particle reuse are used to increase the

efficiency of photon and electron transport. Detailed informations about these are in NRCC packages are NRCC report PIRS 509 (Rogers et al, 2009), NRCC report PIRS 702 (rev) (Mainegra- Hing, 2011), NRCC report PIRS 701 (Kawrakow and Rogers, 2009).

The variance reduction techniques required are directional bremsstrahlung splitting (DBS) to maximize the efficiency of photon production in the BEAMnrc simulation source in conjunction with photon splitting (n split) to maximize the efficiency of the DOSXYZnrc calculation (Walters et al., 2005).

3.4. Scoring or Tallying

After a particle history ends or, more usually, after a particle leaves a cell, its contribution to the score (or tally) is added to the running score of interest (Dunn and Shultis, 2012). The outcomes must be accumulated into overall tallies or scores for the quantities of interest. It is often preferable to set the scoring regions to coincide with the geometric regions. This will eliminate ambiguities in the allocation of energy depositions to the appropriate regions, as particles must stop or take very small steps when they approach a geometrical boundary.

3.5. Monte Carlo Methods for Radiotherapy Dose Calculations

The development of efficient computation code and the advances in computer processor technology in recent years have significantly enabled applications of Monte Carlo method in radiation therapy. Because the interactions of x rays and γ rays with materials can be modeled in detail, the Monte Carlo algorithm can provide very accurate dose predictions provided proper source and tissue models are available (Zhou, 2009). Besides Monte Carlo is accepted to be the gold standard for estimating absorbed dose in or near heterogeneities and this method has superior accuracy compared to the TPS if enough histories are followed to ensure a low degree of statistical noise (Haraldsson, 2003).

The MC method propagates individual particles (photons, electrons, etc.) through the treatment machine, and then through the patient, tracking each particle history to determine where energy is deposited along the particle tracks. Individual particle histories are simulated, based on known particle interaction cross sections, particle transport, and energy deposition characteristics (Fraass, 2003).

For the application of Monte Carlo calculations and external beam radiotherapy, a 2-step development approach is followed. The first step requires a realistic model of the linear accelerator treatment head to quantify the energy, angular, and positional, distribution of photons and electrons entering the patient. This initial simulation is performed once and requires a reformat of the treatment head phase-space distribution into a virtual linac source model. This virtual source must recreate the distribution of photons and electrons exiting the treatment head without the time-consuming process of simulating individual photon and electron trajectories through the various patient-independent structures of the accelerator treatment head, such as the flattening filter. The second step utilizes this virtual source to simulate the linac depth dose and profile characteristics incident upon a water phantom (Demarco, 2002). After these 2 steps, the dose within the patient can be calculated by required programme.

3.6. Monte Carlo Codes

For medical physics applications, there are several code systems that can be used in dose measurements some of which are BEAMnrc/DOSXYZnrc (EGSnrc-based), MCSIM (EGS4-based) (Ma et al., 2004), Geant4 (Poon and Verhaegen, 2005), MCNP (Juste et al., 2005), FLUKA (Andersen, 2005) and PENELOPE (Sempau, 2001). For radiation therapy research, the commonly-used software packages are EGSnrc, MCNP and PENELOPE. The EGS/EGSnrc-based systems, in particular the BEAMnrc/DOSXYZnrc system, enjoy the widest engagements in medical radiation physics in the last two decades. Applications span from X-ray and nuclear imaging to radiotherapy to radiation shielding design (Rogers, 2006).

In this research the EGSnrc system was used for modelling the experimental setup, getting phase space data, checking the beam source, getting stopping power ratio and absorption coefficient, calculating the dose due to its suitability, and ease of used to obtain results. Besides the system was used for creating TLD-100, lung and bone materials in PEGS4 data. The EGSnrc (Electron Gamma Shower nrc) system comprises of BEAMnrc, DOSXYZnrc, DOSRZnrc, FLURZnrc and other simulation codes that come as a package under license to the National Research Council of Canada (nrc) (Kawrakow et al., 2009).

3.6.1. The BEAM/BEAMnrc software

In radiotherapy, accelerator simulations (to derive the spectrum of radiation) and patient dose calculations are the most common Monte Carlo applications. In 1995, the collaborative OMEGA project (Ottawa Madison Electron Gamma Algorithm for electron beam treatment planning) between the National Research Council (NRC) of Canada and the University of Wisconsin in Madison, USA had spawned the release of a general purpose accelerator modeling code called BEAM (Rogers et al., 1995). The BEAM code system was then integrated with EGSnrc and was released in 2002 with the name BEAMnrc (Rogers et al., 2002).

Standard component modules in the BEAMnrc system include, to name a few, the SLABS which can be used to mimic the vacuum window and X-ray target, CONS3R which chamfers the primary collimator, FLATFILT which shapes the flattening filter, CHAMBER which assembles the monitor chamber, MIRROR which represents the tilted optical mirror, JAWS which moulds the X- and Y-jaws and VARMLC or DYNVMLC which crafts the MLC assembly.

The components within the LINAC head and their geometry and material composition are defined in the specify accelerator and build accelerator steps. The components are listed as modules and are called component modules (CM)s. The specify accelerator step is used to “specify” the order of the component modules to be used. Each component module presents itself as a horizontal block with at least a proximal and a distal surface. There must a small air gap between successive

component modules. The component module program handles the repeated problem of finding the whereabouts of the particle and calling the subroutines HOWFAR and HOWNEAR to calculate its trajectory to the next interface/boundary of region of a different material type and/or density. Figure 3.3 shows a schematic view of the steps required to model an accelerator. The CM used in this work is SLABS for phase space scoring plane.

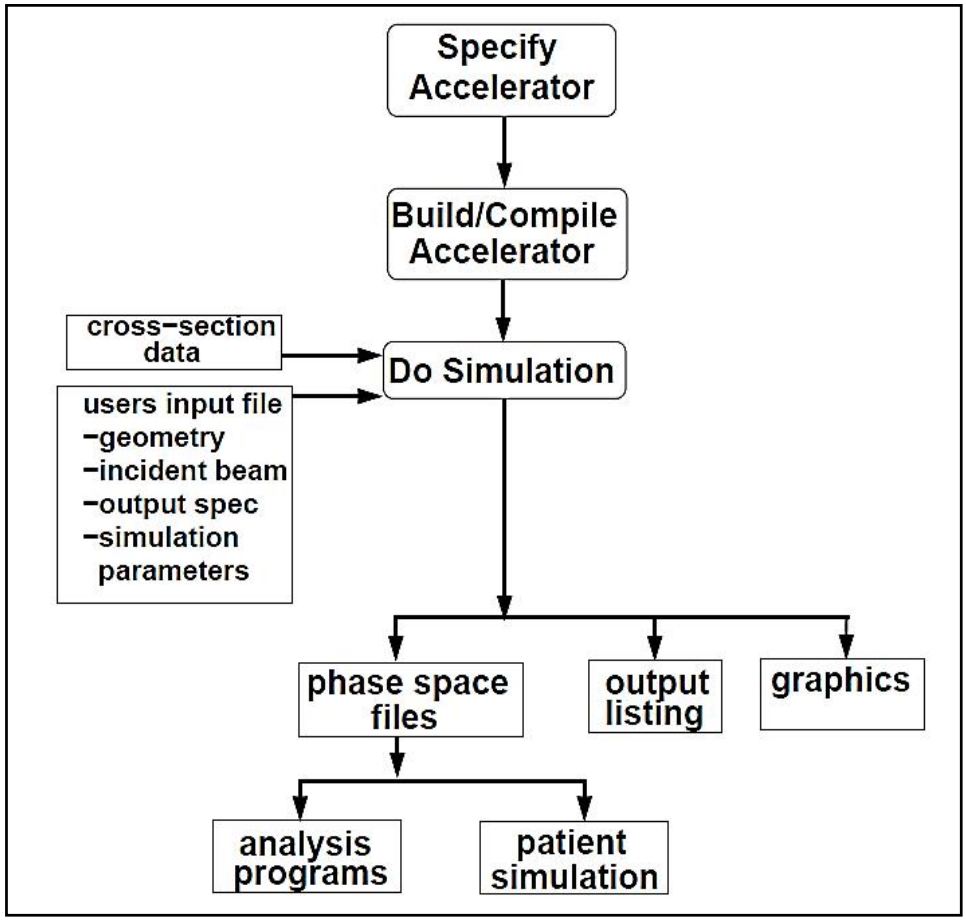

Figure 3.3. Schematic view of the BEAMnrc algorithm (Rogers et al., 2002)

3.6.1.1. Phase Space Data

The phase space data contain data of particle position, direction, charge and weight for every particle crossing a scoring plane. Phase space files can be generated at any scoring plane within an accelerator. It is like an output of BEAMnrc programme.

The first record phase space file is different from the others and contains the following information (Rogers et al., 2009).

MODE RW: The file mode: it can be either ’MODE0’ or ’MODE2’ depending on whether ZLAST is included in the phase-space parameters.

NPPHSP: The total number of particles in the file.

NPHOTPHSP: The total number of photons in the file.

EKMAXPHSP: The maximum kinetic energy of the particles stored in the file.

EKMINPHSPE: The minimum electron kinetic energy (MeV).

NINCPHSP: The number of particles incident from the original (non-phase space) source used to generate the phase space file.

Each record in a phase space file contains the following information about a particle:

LATCH, E, X, Y, U, V, WT, (ZLAST) where:

LATCH contains the particle charge, IQ, the number of times the particle has crossed the scoring plane, NPASS, and information which allows the particle’s history to be traced.

E: is the particle total energy (kinetic and rest mass, single precision).

X: is the particle X-position (cm)

Y: is the particle Y-position (cm)

U: is the X-direction cosine

V: is the Y-direction cosine WT is the particle’s weight;

WT: also carries the sign of W, the Z-direction cosine

ZLAST: is the Z-position of last interaction for photons and is the Z-position of where an electron.

Files, are created with BEAMnrc, are used as input files in DOSXYZnrc.

3.6.2. DOSXYZ/Dosxyznrc Phantom or Patient Dose Scoring

DOSXYZnrc is an EGSnrc-based Monte Carlo simulation code for calculating dose distributions in a rectilinear voxel phantom and is based directly on the DOSXYZ code developed for the EGS4 code system (Walters et al., 2005). EGSnrc/DOSXYZnrc simulates the transport of photons and electrons in a Cartesian volume and scores the energy deposition in the designated voxels. DOSXYZnrc is "stand alone", in the usual EGSnrc sense, that it is controlled by scripts which explicitly refer to the .pegs4dat and .egsinp files. DOSXYZnrc is capable of writing out ASCII formatted dose distribution arrays. There is also a powerful graphical user interface, which allows input files to be created graphically. The geometry is a rectilinear volume with the X-Y plane on the page, X to the right, Y down the page and the Z-axis into the page. Voxel dimensions are completely variable in all three directions. Every voxel (volume element) can have different materials and/or varying densities (for use with CT data).The original DOSXYZ code contained the CT reformatting module which inevitably competes for memory. The new code ctcreate was then written so that DOSXYZ needed only to focus on the dose scoring.

EGSnrc/DOSXYZnrc simulates the transport of photons and electrons in a Cartesian volume and scores the energy deposition in the designated voxels. To make simulation in this programme the steps are followed:

- choose or prepare input file as in the BEAMnrc programme
- select file which contains information about material will be used in simulation
- define phantom size in form of voxel
- introduce phase space file or select the radiation source
- After defining the voxels, the doses which are in the region of interest are proven to write on the output file.

The following source types have been developed for DOSXYZnrc (Walters et al., 2005):

- Parallel rectangular beam incident from the front (isource = 0)
- Parallel rectangular beam incident from any direction (isource = 1)
- Phase-space source, particles incident from any direction (isource = 2)
- Point source incident from the front (isource = 3)
- Beam characterization model, particles incident from any direction (isource = 4)
- Uniform isotropically radiating parallelepiped within DOSXYZnrc volüme (isource = 6)
- Parallel rectangular beam incident from multiple angles (isource = 7)
- Phase-space source incident from multiple angles (isource = 8)
- Full BEAM treatment head simulation as source (isource = 9)
- Full BEAM treatment head simulation as source incident from multiple angles (isource= 10)
- Simulation through moving MLC with multiple variable settings (isource = 20)
- Full BEAM treatment head simulation through moving MLC with multiple variable settings (isource = 21)

The following Figure 3.4 shows the voxels of the defined medium will be simulated. Voxels may be specified in a column (for depth dose calculations) or slice (for dose profile and depth dose calculations) within a larger phantom of the same medium.

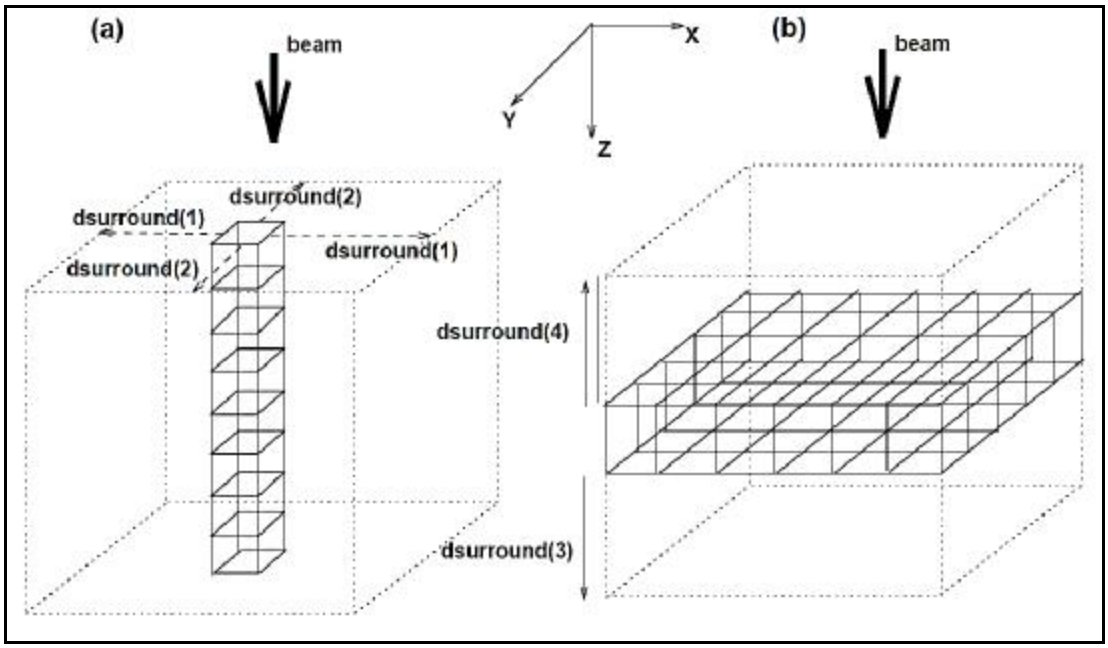

Figure 3.4. In (a) voxels are only specified in a single column for scoring depth-dose, while the rest of the phantom is defined using dsurround(1) and dsurround(2) (dsurround(3) and dsurround(4) are 0 in this particular example). (b) shows voxels specified in a horizontal slice for scoring the dose profile at a given z value. In this latter example, the dimensions of the phantom below and above the slice are defined by dsurround(3) and dsurround(4) respectively. dsurround(1) and dsurround(2) are set to 0 in (b) (Walters et al., 2005).

In this study, isource=2 is used as a radiation source. The phase space data is obtained from Dr.Cho who simulate Varian TrueBeam STx 6MV.

3.6.3. BEAMDP

BEAMDP (BEAM Data Processor) is an interactive program, developed for the OMEGA (Ottawa Madison Electron Gamma Algorithm) project. BEAMDP helps the BEAMnrc users to analyze the electron beam data obtained by the Monte Carlo simulation of the coupled transport of photons and electrons in a clinical accelerator and to derive the data required by the simplified subsource models of these electron beams for use in Monte Carlo radiotherapy treatment planning (Ma and Rogers, 2009). The BEAMDP program can read and process the data in the Phase space file

to produce the energy spectrum of the previous simulation to produce a new radiation source which effectively requires smaller storage space.
When running BEAMDP, a user is given the following options:

- analyze a phase-space data file for beam characterization models;
- derive fluence vs position from a phase-space data file;
- derive energy fluence vs position from a phase-space data file;
- derive spectral distributions from a phase-space data file;
- derive an energy fluence distribution from a phase-space data file;
- derive mean energy distributions from a phase-space data file;
- derive angular distributions from a phase-space data file;
- derive distributions for ZLAST from a phase-space data file;
- derive the distribution of particle weights from the phase-space data file;
- combine two phase-space files into one;
- list the parameters of phase-space particles on the screen.

With BEAMDP programme, the energy fulence and spectral distribution were obtained. These spectrums were helped to calculate the mass energy absorption coefficients and mass stopping powers.

4. THERMOLUMINESCENCE MECHANISM AND THERMOLUMINESCENCE DOSIMETERS

4.1. Luminescence

The term luminescence implies luminous emission which is not thermal in origin i.e. luminescence is 'cold light', light from other sources of energy, which takes place at normal and lower temperature. Basically, luminescence is the light emission from a material following the initial absorption of external energy.

The various types of luminescence are classified according to the mode of excitation. In particular, photoluminescence is the emission of light arising "from direct photoexcitation of the emitting species". Fluorescence, phosphorescence, and delayed fluorescence are well-known forms of photoluminescence. There are other types of luminescence that differ by the mode of excitation (chemiluminescence, bioluminescence, electroluminescence, cathodoluminescence, radioluminescence, sonoluminescence, thermoluminescence, triboluminescence) (Valeur and Berberan-Santos, 2011).

The distinction between fluorescence and phosphorescence is based on the characteristic lifetime τ between absorption of the excitation energy and emission of the luminescence. The line of mark is about 10^{-8} (Garlick, 1949; Curie, 1960). It means that the fluorescence emission is essentially a spontaneous process. It takes place simultaneously with the absorption of radiation and stops immediately when the radiation ceases, as shown in Figure 4.1. But, the phosphorescence emission is characterized by a delay between the radiation absorption and the time t_{max} to reach full intensity. Phosphorescence and thermoluminescence are the same process; the only difference is the fixed and the rising temperature, respectively, of the emitting material during the emission.

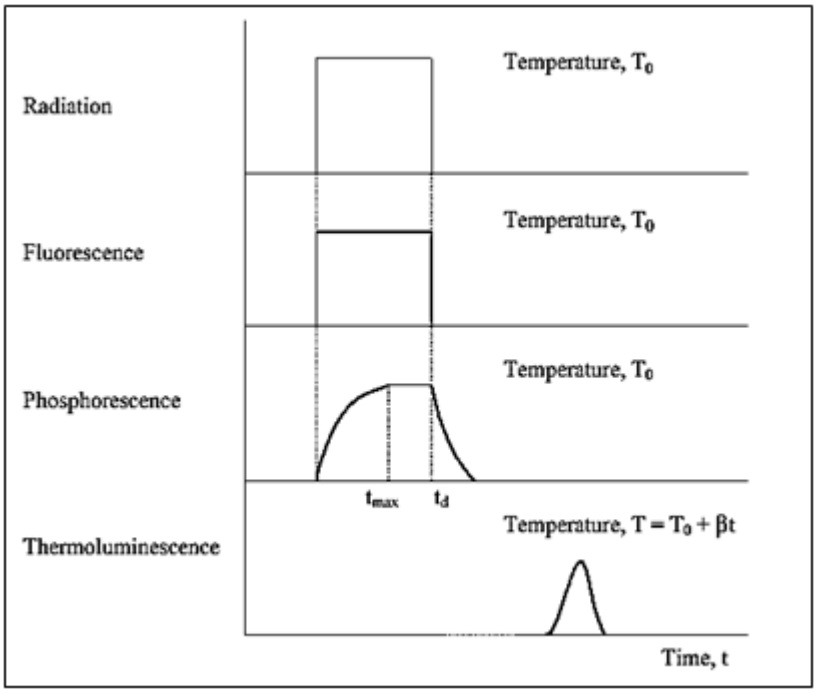

Figure 4.1. Relationships between radiation and the emission of fluorescence, thermoluminescence. T_0 is the temperature at which radiation takes place; β is the heating rate; t_d is the time at which the radiation ends and the decay of phosphorescence begins (Wang, 2002).

As is well known, in luminescence, some energy sources kicks an electron of an atom of its ground state (lowest energy) into an exited state (higher energy) by supplying extra energy, then as this excited state is not stable electron jumps back to its ground state by giving out this energy in form of light (McKeever et al., 1995). According to the Jablonski model (Jablonski, 1935), consider a ground state energy level g and an excited state level e, illustrated in Figure 4.2. Energy from radiation is transferred to the electrons of the solid, so exciting the electrons form g to e (1). Fluorescence takes place when an electron returns to level g (2). If the excited electron makes a transition from the excited state to a metastable level m (3), where it will remain until it receives enough energy to return to the excited state e (4) with the subsequent emission of light. After this process, return to the ground state is known as phosphorescence.

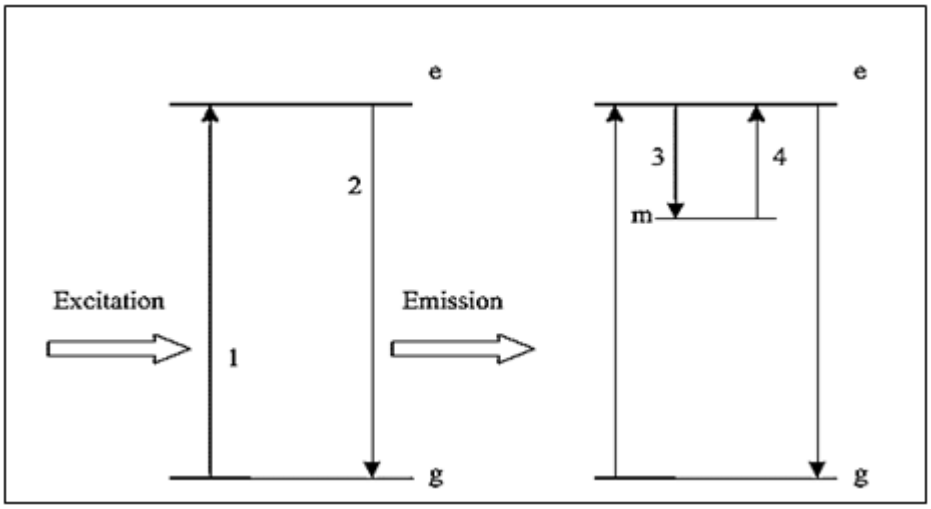

Figure 4.2. Jablonski Model. Fluorescence and phosphorescence (Chen and McKeever, 1997).

4.1.1 Thermoluminescence

Thermoluminescence as mentioned by McKever and et al., is one of the processes in Thermally Stimulated Phenomena (McKeever et al, 1995). In a general view, *thermoluminescence* is a temperature stimulated light emission from a crystal after removal of excitation. Nevertheless, microscopically, it is much more complicated.

With the developing technology, thermoluminescence has various application areas such as, radiation dosimetry, age determination and geology. To be useful for dosimeters, a TL material must have a relatively strong light output and be able to retain trapped electrons for reasonable periods of time at temperatures encountered in the environment (Radiation Safety for Radiation Workers, 2005).

Thermoluminescent dosimeters contain inorganic crystalline or polycrystalline materials doped with suitable activators (Pradhan, 1981). But some TL detectors do not require the addition of an activator but rely instead upon inherent impurities and defects in the natural crystal (Radiation Safety for Radiation Workers, 2005, Chen and McKeever, 1997).

4.1.2. Thermoluminescence Mechanism

A thermoluminescent dosimeter, or TLD, is a type of radiation dosimeter and measures ionizing radiation exposure by measuring the amount of visible light emitted from a crystal in the detector when the crystal is heated. The amount of light emitted is proportional to the dose absorbed by the irradiated material. Shortly TLD based on the thermoluminescence (TL) phenomenon. The TL mechanism is as follows: when a crystalline material is irradiated it suffer alterations in its structure due to ionization; during this process electrons are liberated from the crystal lattice generating two types of mobile carriers: electrons and holes (Nieto, 2004).

For perfect lattice, the electron transitions only take place between energy bands, e.g. electrons in valence band are given enough energy to surmount an energy gap in order to be excited to the next higher energy band, i.e., conduction band, and electrons' return to the valence band will emit fluorescence. But the lattice has impurities, the phenomenon will not the same as in the perfect lattice. Many general theoretical models have been postulated to explain this phenomenon, but even now difficulties arose when specific dosimetric materials are considered (Azorin, 1990; McKeever, 1985). One of the possible mechanisms for TL emission may be developed by considering the electronic band model (EBM) of the semiconductor (Fig. 4.3), considering three main elements as existing ones (e.g. recombination centres (RC), mobile carriers (MC) or charge carriers (CC), and traps (T)). Besides, the EBM assumes the existence of energy excited states in the forbidden band (FB) which play the role of traps or recombination centers.

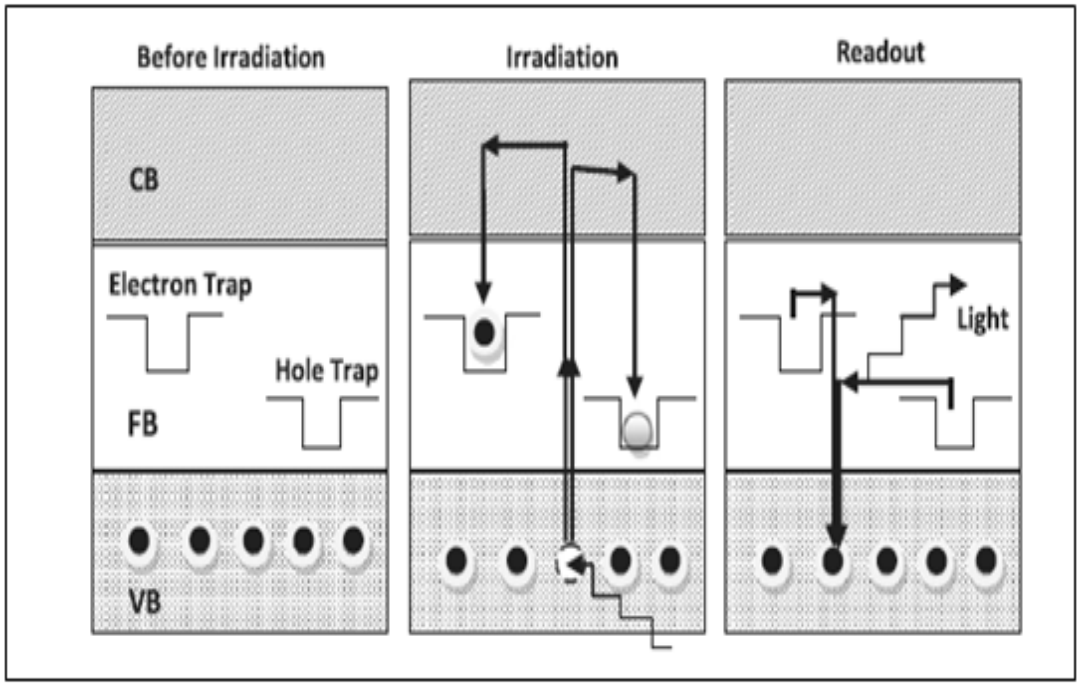

Figure 4.3. The mechanism of thermoluminescent phenomenon (Rivera, 2012)

Ionizing radiation can supply the energy for creating the mobile carriers (electron and holes). The electrons are free to travel from the valence band (VB) to the conduction band (CB), meanwhile, the holes remain in the valence band or are free travelling near the VB. Due to the light emission process that involves the releasing of some traps at different energies, the mobile carriers are released at different temperatures giving rise to a glow curve which is characteristic of the material exhibiting one or more peaks (Rivera, 2012). Figure 4.4 shows some glow curve examples of some thermoluminescent materials.

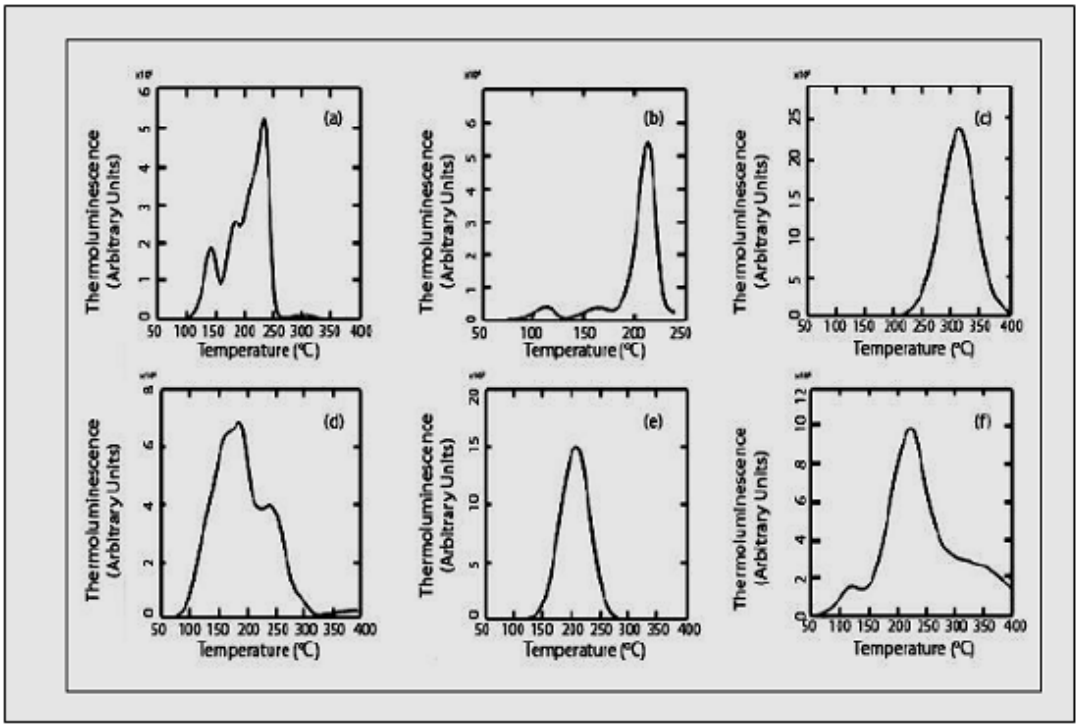

Figure 4.4. Some representative examples of glow curves of some of the main TLD materials. (a) LiF: Mg,Ti; (b) LiF: Mg,Cu,P; (c) CaF_2:Mn; (d) CaF_2:Dy; (e) Al_2O_3:C; (f) $CaSO_4$:Dy (McKeever et al.,1995).

The shape, position and intensity of the glow peaks are related to various trapping parameters of the trapping states responsible for the TL emission. These parameters include the order of kinetics b, the activation energy E (eV) and the frequency factor S (s^{-1}). Several methods are currently employed for obtaining E of an isolated glow peak. Most of these methods can only be applied when the order of kinetics b is well defined, namely when this peak is fairly isolated.

4.1.2.1. First- and second-order kinetics

Usually the intensity versus temperature or glow curves are analyzed on the basis that they represent either first- or second-order kinetics or, in rare cases,more complex kinetics. As is well known, first-order kinetics are observed where the intensity of the thermoluminescence is proportional to the concentration of thermally released charges. If the thermally released charges are retrapped one or more times before entering into a light-emitting process, "second-order" kinetics are observed

(Fairchild et al, 1978). The first theoretical treatment for a well-isolated TL peak was proposed by Randall and Wilkins, who mainly considered the non-re-trapping case. This case is usually called first-order kinetics (Rasheedy, 1996). In this chapter the first and second order kinetics will be simply described. The rate of release of electrons per unit time, s at a temperature T (K) is given;

$$I = -\frac{dn}{dt} = nSexp(-\frac{E}{kT}) \quad (4.1)$$

where I (in arbitrary units) is the TL intensity, n (cm^{-3}) the electron concentration trapped at time t (s) and k (eV K^{-1}) Boltzmann's constant. For first order kinetics:

$$I = n_0 Sexp(-\frac{E}{kT})exp\left[-\frac{S}{R}\int_{T_0}^{T} exp(-\frac{E}{kT'})dT'\right] \quad (4.2)$$

where R (K s^{-1}) is the linear heating rate and n_0 (cm^{-3}) is the concentration of traps populated at the starting temperature T_0 (K). The re-trapping and proposed an equation for the second order process were considered by Garlick and Gibson.

$$I = -\frac{dn}{dt} = \frac{n^2 S}{N} exp(-\frac{E}{kT}) \quad (4.3)$$

where N (cm^{-3}) is the concentration of traps.

When the first order and second order kinetics are inadequate, the general order is used.

$$I = -\frac{dn}{dt} = n^b S' exp(-\frac{E}{kT}) \quad (4.4)$$

where S' ($cm^{3(b-1)}$ s^{-1}) is a pre-exponential factor. Later, the equation 4.4 has recently been modified to:

$$I = -\frac{dn}{dt} = \frac{n^b}{N^{b-1}} S exp\left(-\frac{E}{kT}\right) \quad (4.5)$$

4.1.3. A Brief History of the TLDs in Radiotherapy

Thermally Stimulated Luminescence (TSL) or Thermoluminescence (TL) is the emission of light from an insulator or a semiconductor following the previous absorption from the source of exciting light energy, X-rays, or other ionizing radiation. The phenomenon of TL may have been known as early as 1663 as empirically defined, when Sir Robert Boyle reported to the Royal Society about "experiments and considerations upon colours with observations on diamond that shines in the dark" (1663) and described how, upon warming of a diamond in contact with his body, he saw a luminescence in the dark (Rivera, 2012). The history of TLD commences in the same year as the discovery of X rays by C. W. Roentgen in 1895. E. Wiedemann and G. Schmidt described the use of TL for the detection of 'cathode rays', the term used for the electron beams before the electron as such was discovered. However, the developments which form the basis of the present use of TLD in medicine are centred around the work F. Daniels at the University of Wisconsin. F. Daniels' first successful application of LiF to radiation dosimetry during atomic bomb testing in the early 1950s used a form of this material which is almost identical to the TLD-100 of today (McKeever et al., 1995). The most promising material to emerge at this time was LiF. Only later was it to become evident that the desirable properties of the material were the result of the interplay between the complex defects present within the material resulting from the presence of Mg and Ti impurities. This realization emerged with the work of Cameron and colleagues and this work led eventually to the patenting of TLD-100 by Harshaw Chemical Company in 1963 (McKeever et al., 1995). This events appear to be still relevant for clinical TLD in 1998. It was found that 90% of all academic institutions and 50% of other hospitals used TLD for in vivo dosimetry. Semiconductor diodes were the second most common detector with about half the abundance of TLD (Kron, 1995).

4.1.4. The LiF: Mg, Ti (TLD-100) Dosimeters

Thermoluminescent dosimetry (TLD) has been widely employed as a technique of ***in vivo*** dosimetry measuring dose and fluence of both ionizing and non-ionizing radiation. The most commonly used dosimeter has been lithium fluoride (LiF) containing trace impurities of magnesium and titanium denoted as TLD-100 (Cooke and Hogstrom, 1980). LiF is fitting that the first family of TLD materials. LiF doped with about 180 ppm magnesium and 10 ppm titanium provides a good thermoluminescent phosphor (Jain, 1986).

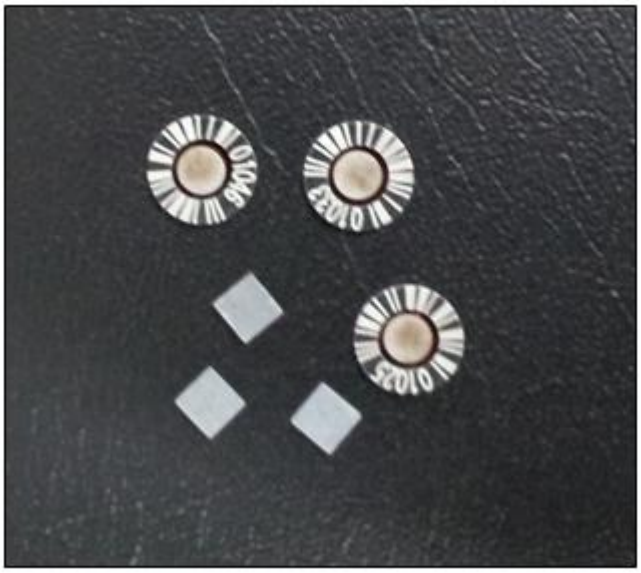

Figure 4.5. TLD 100 chips.

TLD-100 dosimeter materials come in a variety of physical forms, including single crystal, extruded rods, hot pressed chips, powder or impregnated PTFE (Teflon) disc (McKeever et al, 1995). The most popular form is probably the 3.2 x 3.2 x 0.89 mm^3 hot pressed chip. But in clinic the other forms are 3.2 x 3.2 x (0.15 and 0.38) mm^3 used too. The TLD-100 chips are shown at Figure 4.5.

Dose Response: Coupled with other properties, it has proved to be an excellent ionizing radiation dosimetry material for which purpose it has been used widely in spite of its several drawbacks, such as complicated peak structure and complications in reuse procedure, the need for sophisticated instrumentation for

measurement of low doses, supralinearity beyond 10 Gy, severe radiation damage beyond 10^3Gy and unknown preparation parameters (Pradhan, 1981). The dose response of it is linear up to 1 Gy (Figure 4.6).

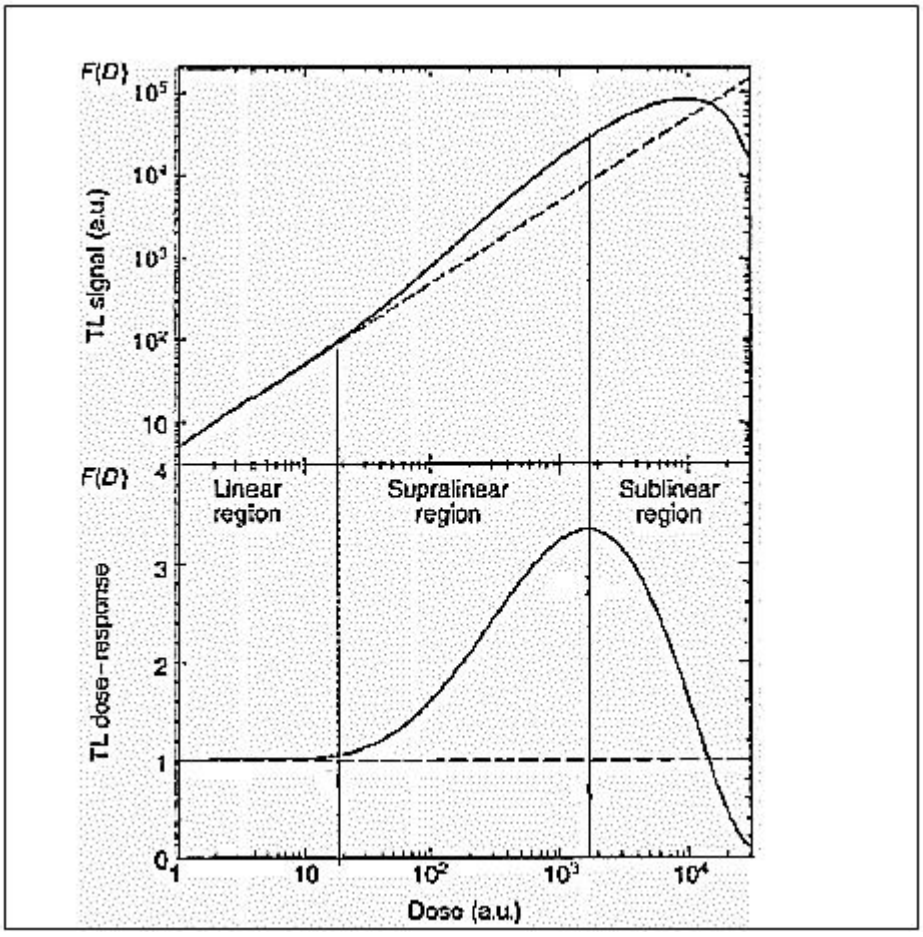

Figure 4.6. General Futures of TL dose/fluence response showing regions of linearity, supralinearity, saturation and radiation damage. The region of linear response usually defines the most useful dose range of the dosimeter. The dose-response of glow peak 5 in LiF:Mg,Ti (TLD-100) has been demonstrated to be linear from the lowest dose level measurable of ˜3μGy to 1Gy (Horowitz et al., 2007).

Sensitivity: Thermoluminescence detectors, usually made of LiF, are often used for depth dose measurements in heterogeneous phantoms because of their compact size and reasonable tissue equivalence. Upon being irradiated, atomic electrons are ionized and trapped in higher energy states from the impurities in the TLD crystal. These electrons can drop back to their ground state by thermal

stimulation, emitting visible light photons of energy equal to the energy difference between the trap state and the ground state. These photons are detected by PM tubes, which convert to electrical current signal measured by the electrometer as collected charges. However, the electrons in the low energy trap state are not as stable as high energy ones, necessitating the pre-heating process up to 100–150 °C to eliminate the luminescence coming from these unstable, shallow traps in order to have precise readouts over repeated measurements. Further, the TLD's luminescence response under same condition is different with each other, due to the subtle crystal structure different from imperfect manufacturing. Therefore, sensitivity correction is necessarily needed. Finally, TLD needs to be calibrated in order to convert charge collected into dose deposited.

On each occasion, the sensitivity S_i of each TLD was found using;

$$S_i = \frac{<Q>}{Q_i} \qquad (4.6)$$

where Q_i was an individual TLD reading and <Q> was the average of all TLD readings in a single irradiation.

Photon Energy Dependence: TLD-100 is routinely used for dose measurements in radiotherapy since the effective atomic number of 8.2 is close to that of water or tissue.This property is well reflected in the photon energy response. Figure 4.7 shows the calculated and measured energy response of LiF:Mg,Ti (TLD-100).

Curve A is the relative calculated absorbed dose in LiF per unit of exposure based on the ratio of exposure based on the ratio of the mass energy absorption coeffitient of LiF to that of air. Curve B is ralative TL response per unit exposure determined experimentally. Curve C represents the relative TL per unit absorbed dose in LiF. Curve C is obtained by the ratio: curve A/ curve B (McKeever, 1995).

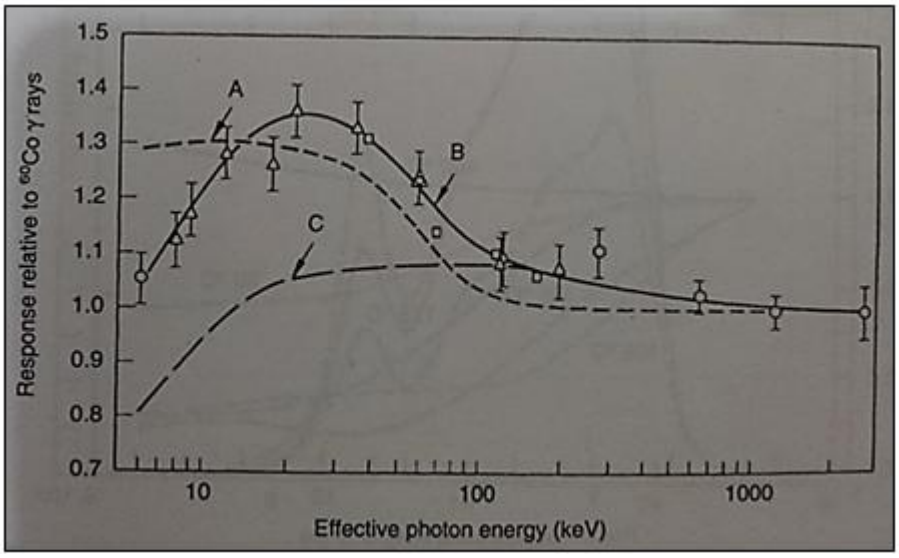

Figure 4.7. Photon energy response of LiF:Mg,Ti per exposure and absorbed dose in LiF (McKeever, 1995).

Annealing: Annealing is the thermal treatment needs to erase any irradiation memory from the dosimetric material. Some thermoluminescent material required a complex annealing procedure. LiF:Mg,Ti is one of them. It requires a high temperature anneal, followed by a low temperature anneal. Generally speaking the high temperature anneal is required to clear the dosimetric traps of residual signal which may cause unwanted background during subsequent use of the dosimeters. The low temperature anneal is required to stabilize and aggregate low temperature traps in order to enhance the sensitivity of the main dosimetry traps and to reduce losses of radiation-induced signal due to thermal or optical fading during use. The combination of these two anneals is termed standard anneal (Furetta, 2003).

For LiF the standard annealing consists of a high temperature anneal at 400°C during 1 hour followed by a low temperature thermal treatment for 20 hours at 80°C. In some laboratories, annealing at 100°C for 2 hours has been used instead of the longer anneal at 80°C (McKeever, 1995; Furetta, 2003, McKinlay, 1981).

Glow Curve: It is the plot of the thermoluminescence intensity, I, as a function of the sample temperature during read out. The LiF:Mg,Ti has a caracteristic glow curve consisting mainly of 5 peaks (Figure 4.8) (Blak et al., 1974). The Figure 4.8 shows till peak 6.

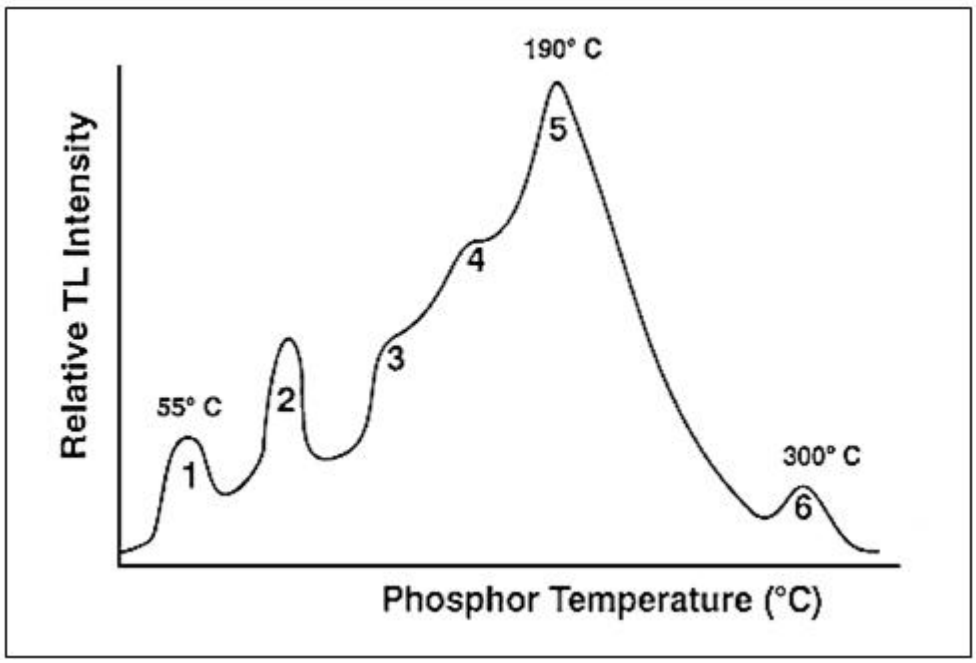

Figure 4.8. The glow curve of TLD-100 (Keser,2005)

Actually the glow curve of LiF:Mg,Ti consists of a relatively large number of glow peaks. The main dosimetric peak, Peak 5, appears at approximately 190 ^{0}C followed by a series of peaks numbered 6–13 which appear at higher temperatures up to 450 ^{0}C (Shachar, and Horowitz, 1993). Peak 5 has a low temperature shoulder known as Peak 4, and several low temperature peaks in the temperature range between 55 and 150 ^{0}C numbered 1–3. In addition there are a large number of peaks which appear below room temperature and may be observed if the sample is irradiated at liquid nitrogen temperature and the thermoluminescence emission is observed while the sample is heated and allowed to reach room temperature. These low temperature peaks are numbered 0, −1, −2, −3, −4, etc. Because of the low temperature peaks the TLD-100 are annealed 1-2 hours at 100 ^{0}C or 16-24 hours at 80 ^{0}C prior to irradiation (McKinlay, 1981).

4.1.5. TLD Reader System

Variations in the TLD evaluation process may alter the results of TLD measurements. Thus, it is important to understand the reader system used to evaluate

TLDs. The TLD reader system used to heat a TLD phosphor, and measure the resulting thermoluminescence light emitted. Basically the TLD reader system principle is shown in Figure 4.9.

The basic TLD reader system consists of a planchet for placing and heating the TLD, a photomultiplier tube to detect the thermoluminescence light emission and convert it into an electrical signal linearly proportional to the detected photon fluence and an electrometer for recording the PMT signal as a charge or current. A TLD is placed in the reader (either on a planchet or in a carrier disk) and is heated. Heating is accomplished by means of preheated Nitrogen (N_2) gas or by an ohmically heated pan. The emitted luminescence is then detected and amplified by a photomultiplier tube (PMT) that converts the TL into an electrical signal.

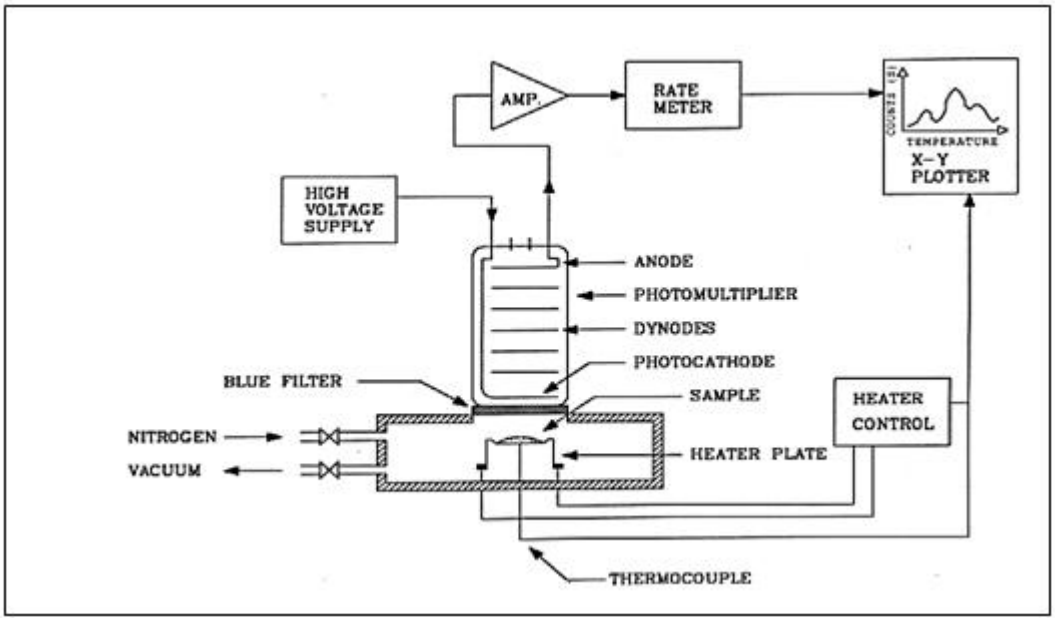

Figure 4.9**.** Shematic diagram of a TLD reader system (Botter-Jensen, 1997).

4.2. Materials and Methods

4.2.1. Materials

4.2.1.1. Accelerator

The 6 MV x-ray beams in this study were from a TrueBeam™ STx linear accelerator with a high definition 2.5 mm MLC leaf (High Definition, HD (MLC), Varian Medical Systems, Palo Alto, CA) at the University of Chicago Radiation and Cellular Oncology Center. The system has the capability of delivering both flattening filter and flattening filter free beams. The system uses sophisticated imaging and respiration synchronization tools to visualize soft tissue during treatment and make changes accordingly. With new beam-shaping capabilities used with the High-Intensity Mode, it enables the delivery of large doses in small places (Varian Medical Systems). The TrueBeam™ STx combines all of the advanced radiotherapy techniques within its capacity such as IMRT, IGRT, Gated RT, Rapidarc, SRS and SBRT. Figure 4.10 shows TrueBeam™ STx Accelerator.

The accelerator output was configured to produce 0.85 cGy per monitor unit (MU) under reference calibration conditions, which was defined at depth of d_{max} (1.5 cm for 6 MV) and a 10X10 cm^2 field, 100cm SAD. For this accelerator 100 MU was equal to 85 cGy, 103.4 cGy and 111.2 cGy in solid water, bone and lung phantoms respectively.

Figure 4.10. TrueBEAM™ STx Accelerator

4.2.1.2. TLD-100 Chips

In this study the TLD-100 chips which their thicknesses were 0.89 mm (large), 0.38 mm (medium) and 0.15 mm (small) were used. The TLD-100 chips has a density of 2.64 $g \cdot cm^{-3}$, with Mg and Ti dopant concentrations and its fractional composition by weight:

Lithium: 2.670 $x10^{-1}$,

Fluorine: 7.328 x 10^{-1},

Magnesium: 2 x 10^{-4} ,

Titanium: 1 x 10^{-5} (Davis, 2003, NIST).

These values were used also for EGSnrc PEGS4 data to create TLD-100.

The following table 4.1 summarizes the general characteristics of LiF: Mg, Ti TLD material.

Table 4.1. The general characteristics of LiF: Mg, Ti TLD material.

TLD	Relative gamma ray sensitivity	TL emission peak (Aº)	Dosimetric peak temp.(ºC)	Useful range	Effective atomic No. (Z)	Photon energy dependence at 30 KeV (Co^{60}=1)	TL fading
LiF: Mg, Ti	1	4000	200	50µGy to 10^3Gy	8.2	1.3	0% month

Totally 158 TLDs were used. 59 of total were large TLDs, 47 TLDs were medium and rest of them were small TLDs. Among 158 TLDs, 15 of them were separated for background TL measurements.

4.2.1.3. TLD Reader System

TLD readouts were performed using a HARSHAW QS 5500 (Termo Scientific) type reader. It measures and evaluates doses with an automatic, compact table-top system that provides unattended operation for up to 50 thermoluminescence detectors (TLD). The reader (see Figure 4.11) has a linear, programmable heating system and a cooled photomultiplier tube with associated electronics to measure the TL light output.

Figure 4.11. HARSHAW QS 5500 type TLD reader.

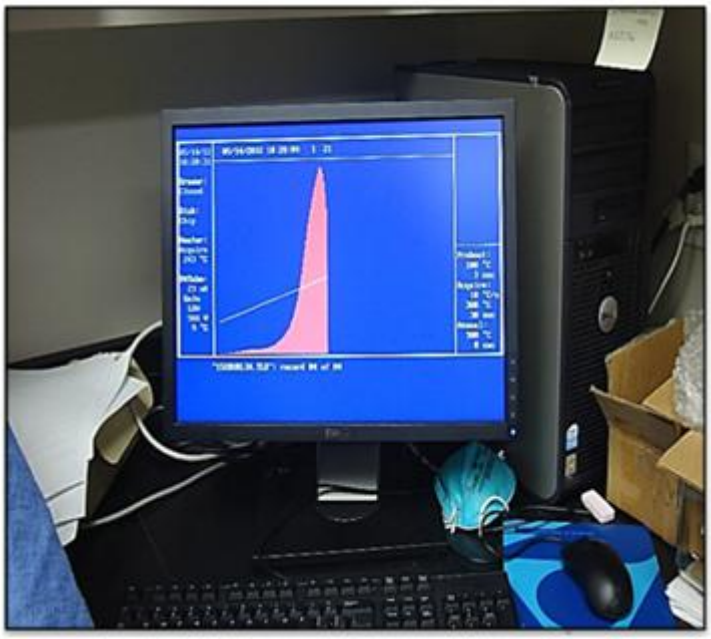

Figure 4.12. Glow curve of TLD-100 chip.

The WinREMS Software, which runs on a separate computer (see Figure 4.12), provides the user interface, the reader control and the applications software. The same time-temperature profile (TTP) was used for the TLD-100 chips.

In this study, the chips were placed on the disc shown in the Figure 4.11. The initial temperature increament was arranged in such a way that the planchet temperature became 100°C in approximately 3 seconds, and then increased linearly at 10°C·s^{-1} to a maximum temperature of 300°C. A continuous flow of nitrogen gas was used to purge the heating chamber, both duringand after readout to prevent the anomalous fading.

4.2.1.4. TLD Annealing Oven and Furnace

The TLD-100 annealing procedure is not as simple, it requires two step annealing: The first one is high temperature annealing and the second one is low temperature annealing. In this study the Fisher Scientific™ Isotemp™ Oven (Fisher Scientific, Pittsburgh, PA) (see Figure 4.13) was used for high temperature annealing proses.

Figure 4.13. a) Fisher Scientific™ Isotemp™ Oven b) Inside of the Fisher Scientific™ Isotemp™ Oven and c) Control Panel of Fisher Scientific™ Isotemp™ Oven.

The high temperature annealing before re-use of LiF:Mg,Ti has two functions: I) to minimise the residual TL signal by emptying the high temperature traps (6-10); II) to restore the original sensitivity and glow curve structure. The recommended high temperature annealing procedure for LiF:Mg,Ti is 400 ^{0}C for one hour. So the TLDs were heated at 400 ^{0}C for an hour.

The TLD annealing furnace 120 VAC (Radiation Product Design, Inc. Albertville, MN. Item number: 168-001) (see Figure 4.14) was used for low temperature annealing prosess. The purpose of the low temperature annealing is to reduce fading through minimization the contribution of the low temperature peaks (1-3) (see Section 4, 4.1.4). The standard low temperature pre-irradiation annealing for LiF:Mg,Ti is 20-24 h at 80 ^{0}C. So the TLDs were annealed at 80 ^{0}C for 20-24 h.

Figure 4.14. a) TLD Annealing Furnace 168, 001 (120 VAC) Radiation Product Design. b) Inside of the TLD Annealing Furnace 168, 001.

4.2.1.5. Vacuum Tweezers

The vacuum tweezers system (see Figure 4.15) allows the handling of TLDs of varying sizes without risk of damage or contamination. This system eliminates defects caused through pinching, scratching or handling when a mechanical tweezers is used.

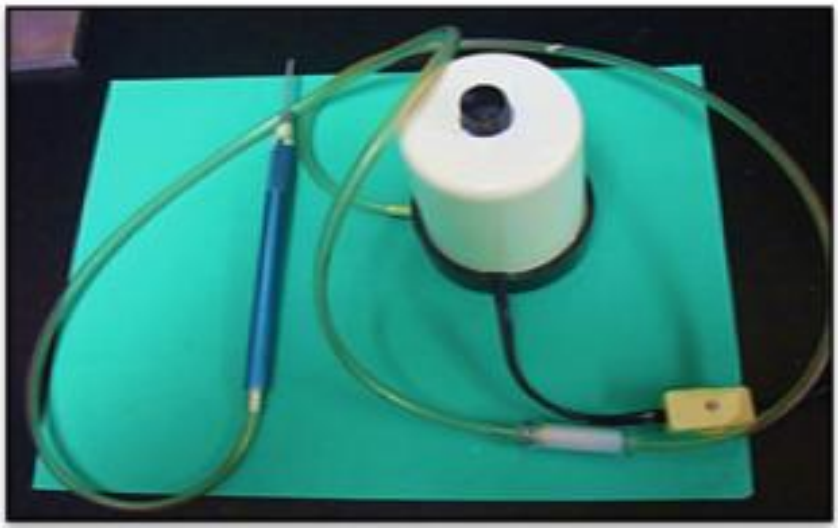

Figure 4.15. A Vacuum Tweezers System

4.2.1.6. Experimental Setups and Phantoms

The presented study has two experimental setups. The first one was done to examine the accuracy of Burlin general cavity theory in bone and lung heterogeneities when measuring dose using TLDs of various thicknesses. A framework to convert measured dose through TLDs to that of in medium using a correction factor, $(f)^{\mathbf{TLD}}_{\mathbf{medium}}$, is developed. The second setup was done to verify dose to medium verification using both, $(f)^{medium}_{water}$ and s/ρ^{medium}_{water} stopping power ratios. And all of the setup were simulated with MC.

Setup 1: Cortical bone (Gammex, Middleton, WI), lung (Gammex, Middleton, WI) and solid water (Gammex, Middleton, WI) phantoms were used to replace real material. Figure 4.16 shows the three slab phantoms designed to be used. The slabs were 30x30 $cm^2$with thicknesses ranging from 0.1 to 5 cm. The first phantom consists of a 2 cm cortical bone equivalent material, followed by 3 cm cortical bone equivalent material for back scattering. The second phantom was 6 cm lung equivalent material, followed by 16 cm lung equivalent material and third phantom was 10 cm water equivalent material, followed by 5 cm water equivalent material.

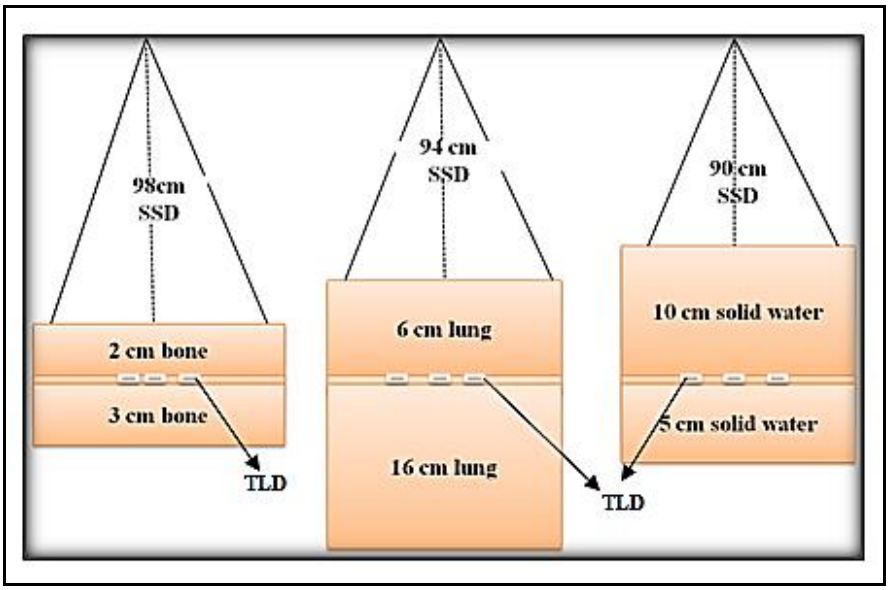

Figure 4.16. Phantom configurations used in the physical TLD component of the experiment, as well as in the simulations used by EGSnrc, (Left) the bone phantom, (Middle) the lung phantom and (Right) the water phantom.

The 6 small, 6 medium and 6 large TLDs were placed at 2 cm depth in bone respectively. The 6 small, 6 medium and 6 large TLDs were placed at 6 cm and 10 cm depth in lung and solid water phantom respectively like in bone phantom. All of configurations had source-to-axis distance (SAD) of 100 cm.

Setup 2: This section was done to dose to medium verification using dose to water calibration. We have designed a simple experiment, which is generally used in heterogeneity correction commissioning with slab phantoms. Figure 4.17 shows the phantom geometries for both lung and bone where 4 cm solid water, either 4 cm cortical bone or 7 cm lung phantom material, and 9 cm solid water slabs (Gammex, Middleton, WI) were used.

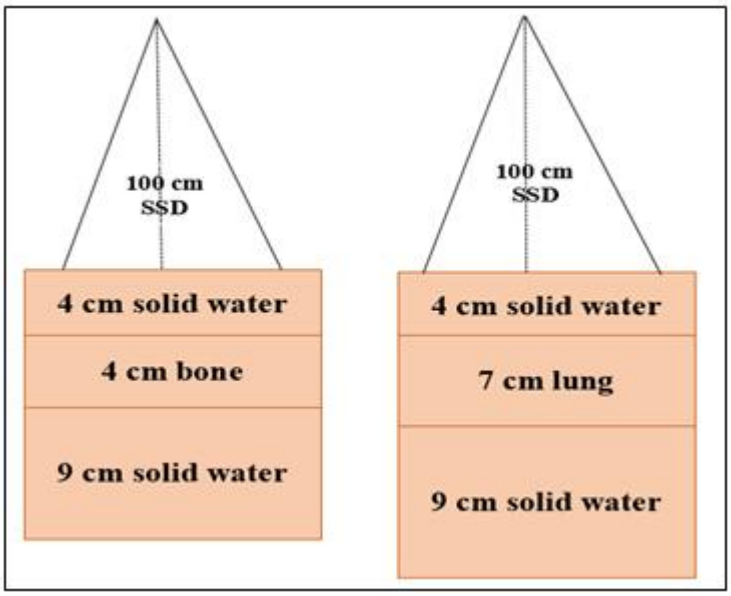

Figure 4.17. Phantom configurations used in the physical TLD component of the experiment, as well as in the simulations used by EGSnrc, (Left) The water-bone-water phantom, and (Right) the water- lung-water phantom.

Each slab was modified to have small cutout sections for TLD placement. TLDs were placed at 1.5 cm, 3.5 cm, 8.5 cm and 10 cm in solid water (3 TLDs at each depth) and at 4.5 cm, 5.5 cm, 6.5 cm and 7.5 cm in bone equivalent plastic (2 TLDs at each depth). Also, two TLDs were placed at the water-bone interface depth of 4 cm, and three TLDs were placed at the bone-water interface of 8 cm. TLDs were placed inside the water-lung-water phantom at 8 different depth (1, 1.5, 4, 6, 8, 10, 11, 13 cm) along the central axis, 3 at each depth. Both configurations had a source-to-surface distance (SSD) of 100 cm.

The composition of the lung-equivalent material is 8.1 % H, 59.3 % C, 1.9 %N, 19% O, 0.6 % Cl, 0.1% Ca, 11.0% Mg by weight, with an average density of 0.32 g/cm^3 (MAUCERI, 1987).The bone equivalent material, is composed of TMD, Araldite, Epoxide and $CaCO_3$ with an average density of 1.85 g/cm^3.

4.2.2. Methods

4.2.2.1. Theoretical Calculations

Theoretical *f* factor described in Equation 2.3 was calculated using the ratios of mass collision stopping power (S_{med}^{cav}),and the average mass energy absorption coefficients of the cavity to the medium $\left(\frac{\mu_{en}}{\rho}\right)_{med}^{cav}$ in addition to the parameter d, which can be calculated using the parameters β and g (see Equation 2.4). For 6 MV photon beam, the mean photon energy (*hv)* is approximately *is* 2 MeV. The average starting energy of the secondary electrons from the Compton Effect is given by

$$\frac{T_{av}}{h\nu} = \frac{\sigma_{tr}^{e}}{\sigma^{e}} \tag{4.7}$$

where σ^{e} is the Klein-Nishina energy and σ_{tr}^{e} is the energy transfer cross section for Compton interaction (Horowitz, 1982) which resulted in a T_{av} of about 1.1 MeV. The average equilibrium-spectrum electron energy is assumed to be about 0.55 MeV. Therefore the mean photon energy of 2 MeV was used to find the $\left(\frac{\mu_{en}}{\rho}\right)_{med}^{cav}$ and the average equilibrium-spectrum electron energy of 0.55 MeV was used to find (S_{med}^{cav}) from NIST (National Institute of Standards and Technology) database. In order to validate these assumptions, Monte Carlo phase space files were recorded at the TLD level and both photon and electron spectrums were analyzed and spectrum weighted average of $\left(\frac{\mu_{en}}{\rho}\right)_{med}^{cav}$ and (S_{med}^{cav}) were calculated. Eighteen *f* factors for each TLD thickness in each medium were calculated using all combinations of the six different *β* (Table 2.2) and three different *g* parameters (Table 2.1).

4.2.2.2. TLD measurements

TLD measurements were made along the central axis at various depths as mentioned section 4.2.1.7. Before using the TLDs, the standard annealing procedure (see section 4.1.4) as recommended by the manufacturer was used. The chips were annealed at 400°C in a high-temperature oven for one hour, in an aluminum holder. After the high-temperature annealing, the chips were left for fast cooling to room temperature by placing the tray on a brass block. After approximately 30 minutes, they were then annealed at 80°C in a low-temperature oven for 20- 24 hours, and were again rapidly cooled to room temperature, where they were kept at least 16-24 hours. A total of 109 LiF:Mg;Ti (TLD-100) (Saint-Gobain Crystals and Detectors (TLD-100, Bicron, Solon, OH)) were irradiated four times under consistent conditions to determine a relative sensitivity for each dosimeter in order to determine the "best" TLDs to use. The irradiations were done in 10 cm depth solid water phantom which was 10 cm water equivalent material, followed by 5 cm water equivalent material. The TLDs were performed using 10x10 cm^2 field size of the 6 MV photon beam with 115 and 150 MU dose. The sensitivity factor of TLDs was calculated using the procedures (see 4.1.4 equation 4.6) described by Reft et al.earlier (McKinlay, 1981). Basically, we divided the charge value for all TLDs by the individual group average. This relative readout value was then averaged between the four groups, and the standard error of the mean was computed for every TLD. For reproducible results only the TLDs with less than 2% percentage standard deviation were used (see Appendix A). This average sensitivity factor was multiplied for each TLD reading.

The measurements using the phantoms and TLDs (small, medium and large) as they are shown in Figure 4.16 were performed by 6 MV photons and 10x10 cm^2 field size from a TrueBEAM^{TM} STX linear accelerator. The phantoms were irradiated with 100 monitor units (MU) of the 6 MV photon beam and the exposing was repeated 3 times for each of the bone, lung and water phantoms.

For the second setup as shown in Figure 4.17, the only large TLDs were placed at the depths of 1.5, 3.5, 4, 4.5, 5.5, 6.5, 7.5, 8, 8.5 and 10cm in the water-

bone-water phantom and that of 1, 1.5, 4, 6, 8, 10, 11, 13 cm in the water-lung-water phantom. In this setup, the exposure was performed using 4x4 cm^2 field size of the 6 MV photon beam with 100 MU dose.

4.2.2.3. Monte Carlo Simulations

In this study, EGSnrc (Electron Gamma Shower, National Research Council Canada) based BEAMnrc code (Walters et al., 2001) was used to generate the LINAC model, BEAMdp was used to analyze energy fluence spectrum, and DOSXYZnrc (Walters et al., 2005) was used to calculate dose distribution in phantoms.

4.2.2.3.(1). BEAMnrc

For simulation, BEAMnrc was used to find phase space file. The pegs4 file which was used for this project was 700ICRU. Only three slabs were chosen for each experimental set up. It was achieved by creating a phase space file where we want. The simulations were developed via 6 MV beam using CHO's LINAC head. 10^7 particles were used for this simulation. For lung, water and bone slabs, electron cut-off energy was terminated as ECUTIN = 0.700 MeV; photon cut-off energy was terminated as PCUTIN= 0.01 MeV. In main inputs, the Global Electron Cut off Energy (ECUT) as0.7 MeV and the Global Photon Cut off Energy (PCUT) as 0.01 MeV were chosen for each phase space file. The phase space files were created on the phantom surface. Directional bremsstrahlung splitting (DBS), bremsstrahlung splitting and electron range rejection variance reduction techniques were used for reducing the variance in the estimated solution to reduce the computational time for Monte Carlo simulation.

The phase space data were obtained on the two scoring plane: first one was on bone (or lung or water) phantom surface and second was on TLD surface (see Appendix B). At the end of the program, we got two phase space files and these were used in BEAMDP program to obtain energy fluence and spectra.

4.2.2.3.(2). BEAMDP

The phase space files were used to find the spectral distribution and energy fluence with BEAMDP by 10x10 cm^2 field. As described Appendix C, the energy fluence or spectral distribution were chosen from BEAMDP gui (graphical user interface) and it was executed. The resulting data were used to obtain graph of spectral and energy fluence distribution. According to these data, value of the mass energy absorption coefficient and mass collision stopping power were evaluated using NIST data. The values of the mass energy absorption coefficient and mass collision stopping power were investigated by taking into account the co energy values from the NIST data. For the mass energy absorption coefficient, fluence that corresponding to each energy was multiplied by the mass energy absorption coefficient. Then the "average fluence x mass energy absorption" was divided to the average fluence value. It was recorded as the mass energy coefficient value acquired from MC calculations. For mass collision stopping power, similar method was carried on. The same method applied to bone, lung and water medium.

4.2.2.3.(3). DOSXYZnrc

This study has 5 different phantom experimental setup. As mentioned section 4.2.1.7, three phantoms (*bone*, *lung* and *water)* design were shown in Figure 4.16 that were simulated in setup1 and two phantoms (*water-bone-water* and *water-lung-water*) design, were shown in Figure 4.17, were simulated in setup2. The phantoms were simulated using DOSXYZnrc gui.

Setup 1: The water, lung and bone regions were assigned following material properties H2O521ICRU, LUNG521ICRU and ICRPBONE521ICRU, respectively. In order to set up the cross-sections of the lung, TLD-100 and bone materials, their elemental compositions (including their weight fractions) and the physical densities were inserted into the PEGS4 code. The cross section data for BEAMnrc are created by the code PEGS4. For more information on how running this code, see the PEGS4 manual (Nelson et al, 1985). The phantoms were designed in such a way that so one

can have finer resolution of voxels at the interfaces and central axis (see Appendix D).

The accuracy in dose calculations increases through decreasing voxel sizes; however, applying such reduction will result in an increase in statistical uncertainty in the Monte Carlo dose calculation or an increase in calculation time when a high degree of accuracy is required (Osei et al, 2003). All calculations were simulated until the statistical uncertainty of each voxel (over the build-up region) was less than 1%. All doses were normalized by the D_{max} (the maximum dose in the distribution).

Four TLD-100 chips were inserted along the central axis (CAX) beyond the d_{max} for the measurements in bone, lung and water phantoms. A separate simulation was performed for small, medium and large TLDs in each medium: the size of (3.2×3.2× (0.152, 0.381, 0.889 mm^3)) TLD chips were used. So the phantoms were design to have 3.2×3.2 mm^2 in-plane (i.e., X- and Y- dimensions) voxel size and 0.08 mm voxel size along the central axis (i.e., Z- dimension) near dmax and the media interfaces, where the TLD chips were placed. The DOSXYZnrc phantom designs for bone, lung and water phantoms were shown in Figure 4.18, 4.19, 4.20 respectively.

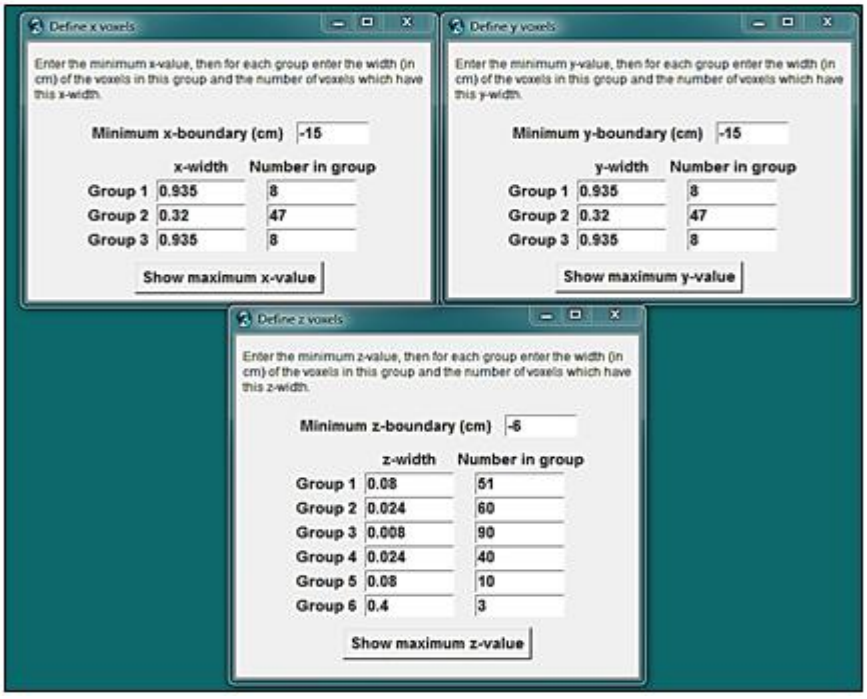

Figure 4.18. Bone Phantom design with MC

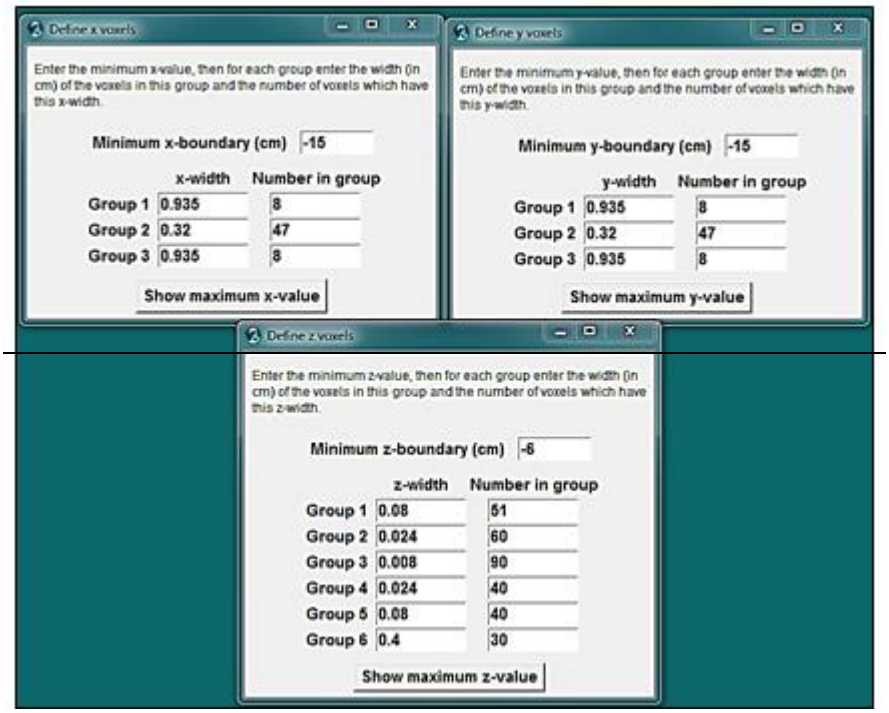

Figure 4.19. Lung phantom design with MC.

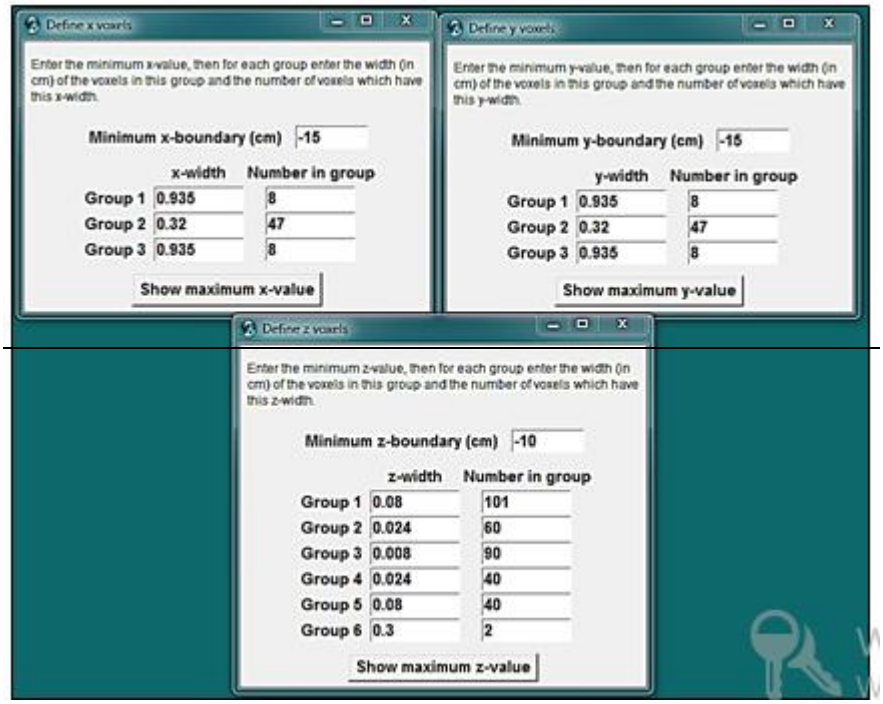

Figure 4.20. Water phantom design with MC.

The SSD for the phantom with the lung inhomogeneity was 94 cm, for the phantom with the bone inhomogeneity it was 98 cm and for the phantom with the water homogeneity was 90 cm.

For lung, water and bone, electron transport was terminated at 10 keV (ECUT = 0.521 MeV) and the creation of delta rays above this cut-off was explicitly simulated (AE = 0.521). The photon transport cut-off was set to 0.010 MeV and the creation of bremsstrahlung photons with energy above 0.010 MeV was also explicitly simulated (AP = PCUT = 0.010 MeV). The fractional energy loss per electron step was set to 2.5% (ESTEPE = 0.025). Typically, $5x10^8$ histories were used in the MC simulations to achieve uncertainty ≤1%. PEGS4 material database with cross-sections for total energies down to 0.521 MeV is used for each medium. NSplit parameter was chosen to be 30 for the highest efficiency in MC calculations (Walters et al., 2005). Three variance reduction techniques have been used in DOSXYZnrc code; directional bremsstrahlung splitting (DBS), photon splitting, electron range rejection for reducing the variance in the estimated solution to reduce the computational time for Monte Carlo simulation. Source beam energy was supplied Linac device simulated by Dr. Cho in BEAMnrc gui.

MATLAB (version 2009b, Mathworks, Natick, MA) was used to analyze the dose distribution calculated. The results were presented as the average of 4 TLDs in each calculation. In order to estimate f factor, dose to medium is, therefore, a separate simulation for each medium was performed without TLDs, and the dose to medium at the same location of TLD was calculated using $f = \frac{D_c}{D_m}$. The Matlab codes are in Appendix E.

Setup 2: The "***solid water – bone – solid water***" phantom: water, bone, water regions were assigned following material properties H2O521ICRU, ICRPBONE521ICRU and H2O521ICRU respectively. The "***solid water – lung – solid water***" phantom: water, lung, water regions were assigned following material properties H2O521ICRU, LUNG521ICRU and H2O521ICRU respectively.

MC simulation was carried out for the 4x4 cm^2 with SSD = 100 cm. PEGS4 521icru data base was chosen as a PEGS4 cross-section data file. For the simulation,

electron transport was terminated at 10 keV (ECUT = 0.521 MeV) and the photon transport cut-off was set to 0.010 MeV. The fractional energy loss per electron step was set to 2.5% (ESTEPE = 0.025). Typically, $5x10^8$ histories were used in the MC simulations to achieve uncertainty ≤1%. Source beam energy was chosen to be monah6.spectrum. The DOSXYZnrc phantom designs for solid water-bone-solid water and solid water-lung-solid water phantoms were shown in Figure 4.21, 4.22 respectively.

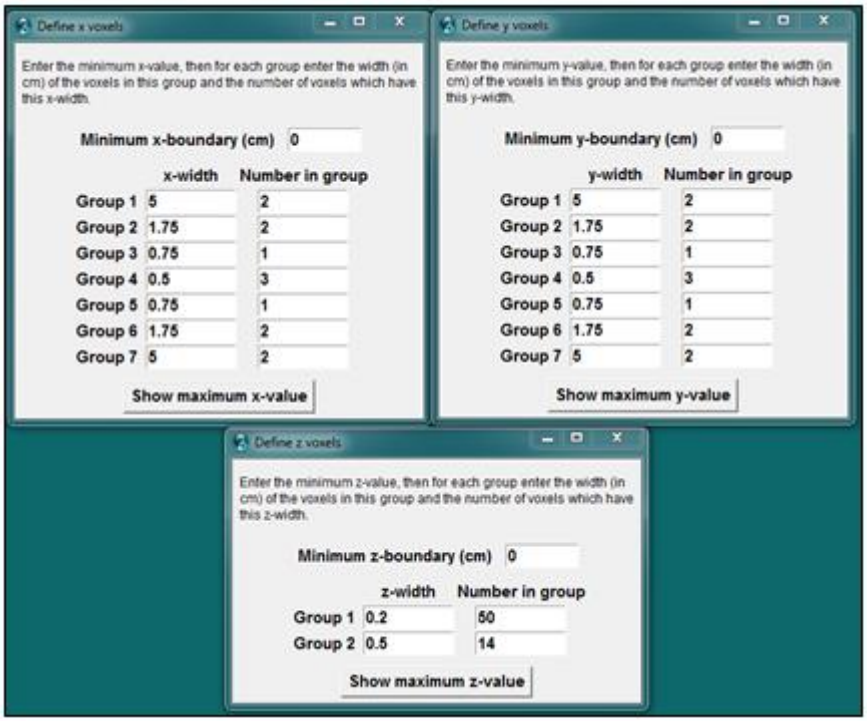

Figure 4.21. Water-Bone-Water phantom design with MC.

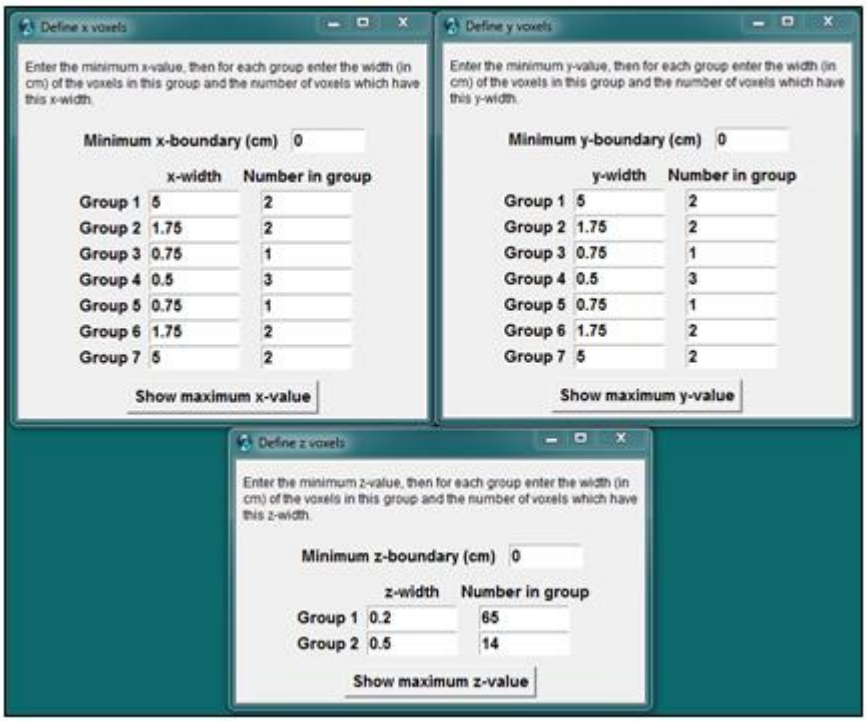

Figure 4.22. Water-Lung-Water phantom design with MC.

4.2.2.4. Dose to Medium Conversion Method

Dose in radiation therapy is traditionally reported as the water-equivalent dose, or dose to water. Monte Carlo dose calculations report dose to medium and thus a methodology is needed to convert dose to medium into dose to water (or vice versa) for comparison of Monte Carlo results with results from planning systems (Paganetti, 2009).

Following is a methodology this study proposed in order to convert the experimental dose to TLD to dose to medium. In case of TLD irradiated in a medium, the Equation $f = \frac{D_c}{D_m}$ can be rewritten as:

$$f_{medium}^{TLD} = \frac{(D_{TLD})^{medium}}{D_{medium}} \tag{4.8}$$

where D_{medium} can be calculated using,

$$D_{medium} = D_{water}(f)^{\text{medium}}_{\text{water}} \tag{4.9}$$

TLD is a relative dosimeter, therefore a dose calibration is needed to be performed in water (or water equivalent medium) by delivering a known dose (D_{water}). Then the dose to TLD in water will be:

$$(D_{TLD})^{water} = D_{water}(f)^{\text{TLD}}_{\text{water}} \tag{4.10}$$

The dose to TLD in medium can be written as:

$$(D_{TLD})^{medium} = (D_{TLD})^{water} \frac{(R_{TLD})^{medium}}{(R_{TLD})^{water}} \cdot \frac{(TPR)^{water}}{(TPR)^{medium}} (f)^{\text{medium}}_{\text{water}} \tag{4.11}$$

where $(R_{TLD})^{water} and (R_{TLD})^{medium}$ are the raw TLD readings in water and medium, respectively. TPR is defined as the ratio of the total absorbed dose on the central axis at depth to that at a point also on the central axis and at the same distance from the source but with the surface of the phantom moved so that the point is at a specified reference depth (Karzmark et al 1965). The TPR was defined to comply with recommendations that x-ray beams should be calibrated at a reference depth in a phantom (Ahnesjo and Aspradakis, 1999). So TPR ratios to account for the differences caused by the change in the medium of measurement. Combining Equations 4.10 and 4.11:

$$(D_{TLD})^{medium} = D_{water}(f)^{TLD}_{water} \frac{(R_{TLD})^{in\ medium}}{(R_{TLD})^{in\ water}} \cdot \frac{(TPR)^{for\ water\ experiment}}{(TPR)^{for\ medium\ experiment}} (f)^{medium}_{water} \tag{4.12}$$

In order to calculate *f* factor Equations 4.8, 4.9 and 4.12 could be combined:

$$(f)^{\mathbf{TLD}}_{\mathbf{medium}} = \frac{(D_{TLD})^{in\ medium}}{D_{medium}},$$

$$(f)^{TLD}_{medium} = \frac{D_{water}(f)^{TLD}_{water}\frac{(R_{TLD})^{in\ medium}}{(R_{TLD})^{in\ water}} \cdot \frac{(TPR)^{for\ water\ experiment}}{(TPR)^{for\ medium\ experiment}}(f)^{medium}_{water}}{D_{water}(f)^{medium}_{water}} \quad (4.13)$$

where $D_{water}(f)^{\mathbf{medium}}_{\mathbf{water}}$ in numerator and denominator will be cancelled yielding:

$$(f)^{TLD}_{medium} = \frac{(D_{TLD})^{in\ medium}}{D_{medium}} = \frac{(R_{TLD})^{in\ medium}}{(R_{TLD})^{in\ water}} \cdot \frac{(TPR)^{for\ water\ experiment}}{(TPR)^{for\ medium\ experiment}}(f)^{TLD}_{water} \quad (4.14)$$

In the final equation, $(f)^{\mathbf{TLD}}_{\mathbf{water}}$ is needed to convert the dose to TLD to the dose to medium, for which this study propose to use the Monte Carlo calculated values.

4.2.2.4.(1). Dose to Medium Verification Using Dose to Water Calibration

The dose to medium in clinical experiments, verifications, and heterogeneity correction commissioning is measured generally with TLDs. Being relative dosimeters TLDs need a calibration under a known dose in water. LiF TLDs having similar effective atomic number can be used to report the dose to water and likewise dose to lung. For such materials both Bragg-Gray and Burlin cavity theories provide similar results. Difficulty is, however, with the measuring dose in material with high atomic numbers like cortical bone where Burlin cavity theory is deemed to be more appropriate (DeWerd).

Based on the work presented here the *f* factors in water and medium are

$$f^{TLD}_{water} = \frac{(D_{TLD})^{in\ water}}{D^{water}} = \frac{(R_{TLD})^{in\ water} \times k_{TLD}}{D^{water}} \quad (4.15)$$

$$f_{\text{medium}}^{TLD} = \frac{(D_{TLD})^{\text{in medium}}}{D^{medium}} = \frac{(R_{TLD})^{\text{in medium}} k_{\text{TLD}}}{D^{medium}} \tag{4.16}$$

where k_{TLD} is the TLD reading to dose conversion factor, i.e., Gy per unit TLD light output and it is independent of the surounding medium. Divinding Eqn 4.15 with 4.16 k_{TLD} will be cancelled yielding

$$\frac{f_{water}^{TLD}}{f_{medium}^{TLD}} = \frac{(D_{TLD})^{medium}}{D^{water}} = \frac{(R_{TLD})^{in\,water}}{(R_{TLD})^{in\,medium}} \frac{D^{medium}}{D^{water}} \tag{4.17}$$

$$\frac{D^{medium}}{D^{water}} = \frac{f_{water}^{TLD}}{f_{medium}^{TLD}} \frac{(R_{TLD})^{\text{in medium}}}{(R_{TLD})^{\text{in water}}} \tag{4.18}$$

We can show it; ($\frac{f_{water}^{TLD}}{f_{medium}^{TLD}}$) as f_{water}^{medium}. If the PDD is crossed by this factor, the problem will solved.

5. ANALYSIS AND RESULTS

The results are presented in three sections: Theoretical Results, Monte Carlo Calculations and Experimental Results.

5.1. Theoretical Results:

The average values of the electron mass attenuation coefficients, β (Table 5.1), and the mean cord length g (Table 5.2) were calculated using equations which are in table 2.1 and table 2.2. The resulting value of parameter d was calculated using all possible combinations of β and g values.

Table 5.1. Average values of the electron mass attenuation coefficients, β in cm^2g^{-1} calculated using Table 2.1 (T_{max}=1.77 MeV).

Author	***Formula***	***Result***
Evans	$\beta_E = \frac{17}{(T_{max})^{1.14}}$	8.867
Paliwal and Almond	$\beta_{PA} = \frac{14}{(T_{max})^{1.09}}$	7.513
Burlin	$\beta_B = \frac{16}{(T_{max} - 0 \cdot 036)^{1.4}}$	7.404
Lovinger	$\beta_L = \frac{18 \cdot 6}{(T_{max} - 0.036)^{1.37}}$	8.750
Chan and Burlin	$e^{(-\beta_{CB}R)} = 0.01$	4.41
Janssens	$e^{(-\beta_J R)} = 0.04$	3.080

Table 5.2. Theoretical values of mean cord length, g in g/cm^2, calculated using Table 2.2.

TLD Thickness	Ogunleye	Horowitz	Burlin
0.015 cm	0.048	0.062	0.073
0.038 cm	0.120	0.155	0.162
0.089 cm	0.281	0.361	0.301

For these calculations, mass collision stopping powers and average mass energy absorption coefficients for cavity and medium were obtained from NIST database (Berger, 1993; ICRU RPT. 37, 1984). The Equation 2.7 was used to obtain value of T_{max} and the Equations 2.4, 2.5, 2.6, Table 5.1 and Table 5.2 were used to calculate the theoretical values of f factors. They were calculated for lung and bone heterogeneities using 18 combinations of β and g and listed in Table 5.3. The results were found to be in good agreement each other with a very small standard deviation (std.) of 0.1 %.

Table 5.3. Theoretical values of $(f)^{TLD}_{medium}$ for the three TLD thicknesses calculated using 18 combinations of β and g values. Each factor is noted with the initials of the authors, i.e., βPA is the β calculated by Paliwal and Almond's equation.

	LUNG			**BONE**		
Thicknes s	**0.015 cm**	**0.038 cm**	**0.089 cm**	**0.015 cm**	**0.038 cm**	**0.089 cm**
βPA, gO	0.822	0.827	0.833	0.899	0.897	0.894
βB, gO	0.822	0.826	0.832	0.899	0.897	0.894
βE, gO	0.823	0.828	0.834	0.899	0.896	0.893
βL, gO	0.823	0.828	0.834	0.899	0.896	0.893
βCB, gO	0.822	0.827	0.833	0.899	0.897	0.894
βJ, gO	0.821	0.825	0.830	0.899	0.898	0.895
βPA, gH	0.823	0.828	0.834	0.898	0.896	0.893
βB, gH	0.823	0.828	0.834	0.899	0.896	0.893
βE, gH	0.824	0.829	0.835	0.898	0.895	0.892
βL, gH	0.824	0.829	0.835	0.898	0.895	0.892
βCB, gH	0.823	0.828	0.834	0.898	0.896	0.893
βJ, gH	0.822	0.826	0.832	0.899	0.897	0.894
βPA, gB	0.824	0.829	0.833	0.898	0.896	0.894
βB, gB	0.824	0.828	0.833	0.898	0.896	0.894
βE, gB	0.825	0.830	0.834	0.898	0.895	0.893
βL, gB	0.825	0.830	0.834	0.898	0.895	0.893
βCB, gB	0.824	0.829	0.833	0.898	0.896	0.893
βJ, gB	0.822	0.826	0.831	0.899	0.897	0.895
Average	0.823	0.828	0.833	0.899	0.896	0.893
% Std.	0.1	0.1	0.1	0.1	0.1	0.1

Table 5.4. The f factor that is used in comparison with MC and experimental results.

Thickness	**0.015 cm**	**0.038 cm**	**0.089 cm**
BONE	0.823	0.828	0.833
LUNG	0.899	0.896	0.893

5.2. Monte Carlo Results

Step 1: BEAMnrc and BEAMDP: Mass collision stopping powers and average mass energy absorption coefficients for cavity and medium were used in theoretical calculations compared with the MC spectrum analysis performed in this study (Tables 5.5, 5.6). For these comparisons, the BEAMDP and the phase space data which were obtained by BEAMnrc were used. The experimental setup were simulated by BEAMnrc and then resulting phase space data were used in BEAMDP. The same parametrs were also calculated using EGSnrc code SPRRZnrc to check our process. A good agreement observed with the maximum deviation of 1% (average 0.3%) between NIST and MC results. MC spectrum weighted values were used in this study for the f factor calculations. The following graphics show the planar fluence profiles and spectral distribution of photons and electrons at the bone, lung and water phantom surface for a 10 × 10 cm^2 field at 6 MV.

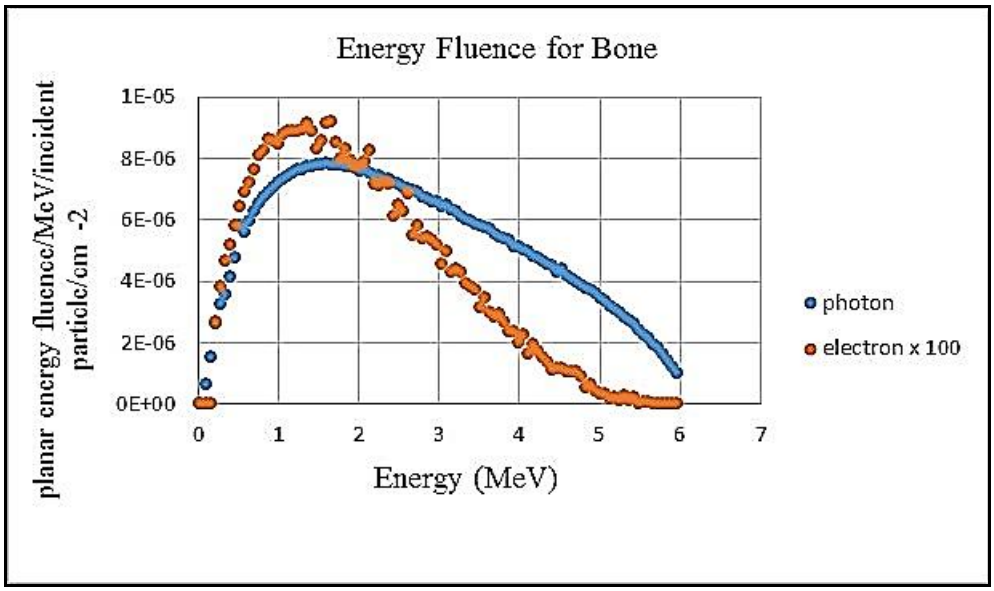

Graphic 5.1. The planar fluence profiles of photons and electrons at the bone phantom surface for a 10 × 10 cm^2 field at 6 MV.

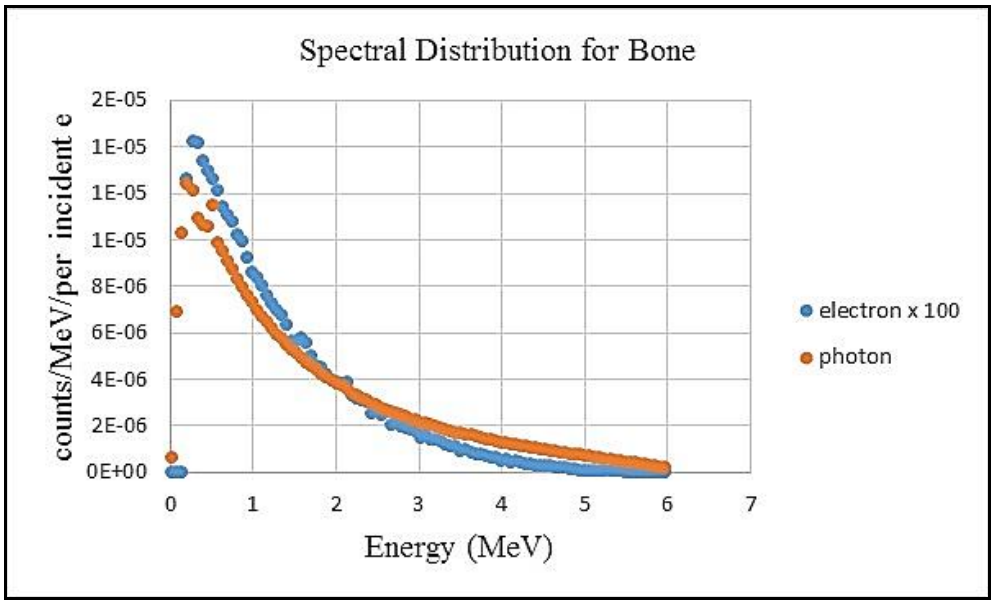

Graphic 5.2. The spectral distribution of photons and electrons at bone phantom surface for the 10x10 cm^2 field of a 6MV.

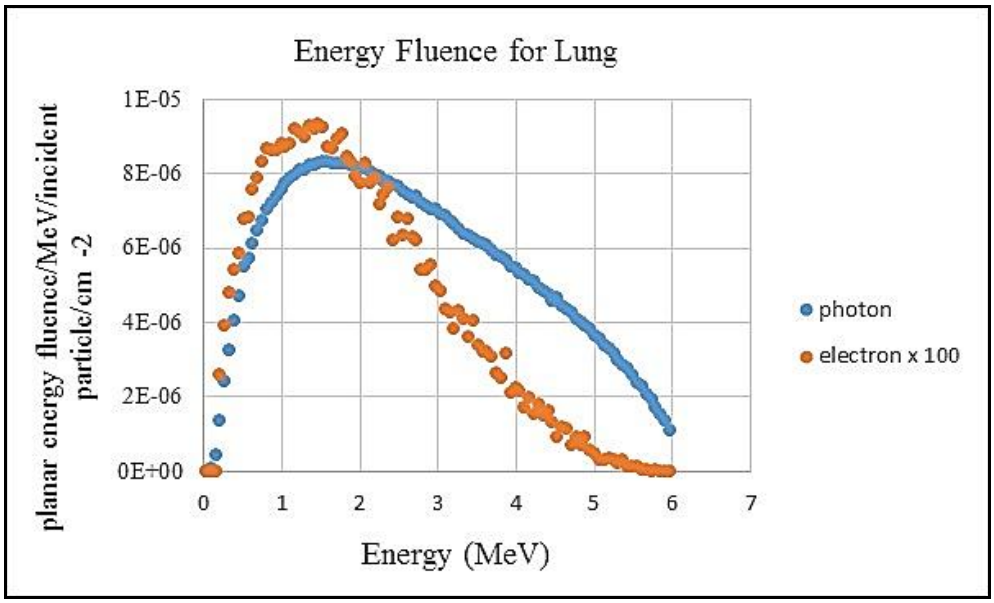

Graphic 5.3. The planar fluence profiles of photons and electrons at the lung phantom surface for a 10 × 10 cm2 field at 6 MV.

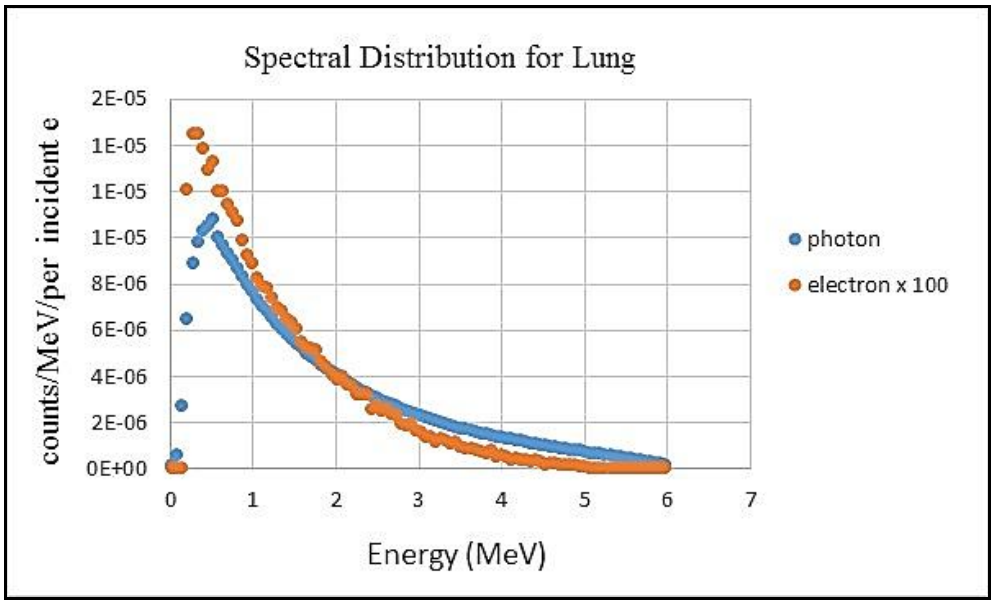

Graphic 5.4. The spectral distribution of photons and electrons at lung phantom surface for the 10x10 cm^2 field of a 6MV.

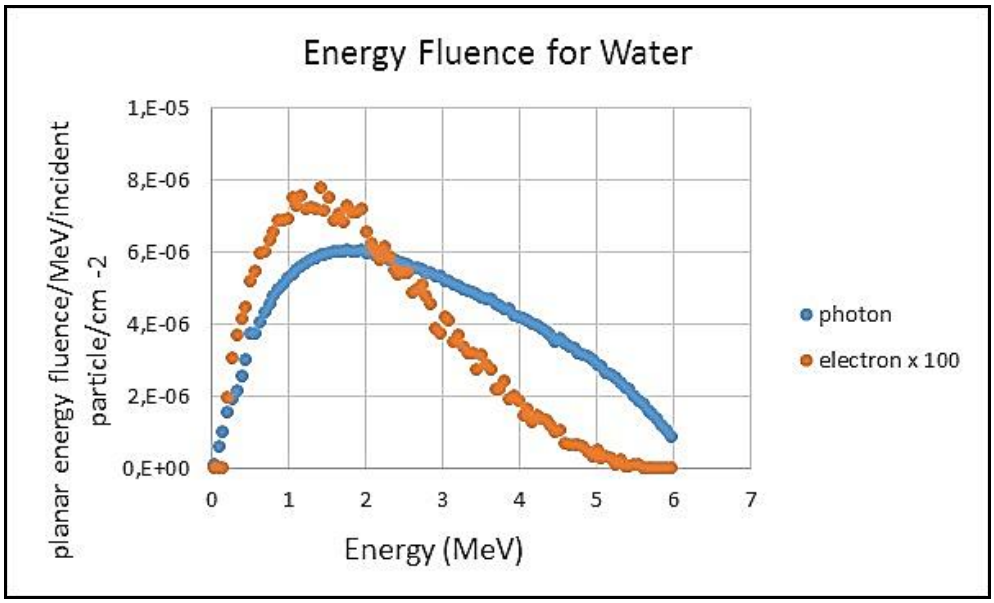

Graphic 5.5. The planar fluence profiles of photons and electrons at the water phantom surface for a 10 × 10 cm2 field at 6 MV.

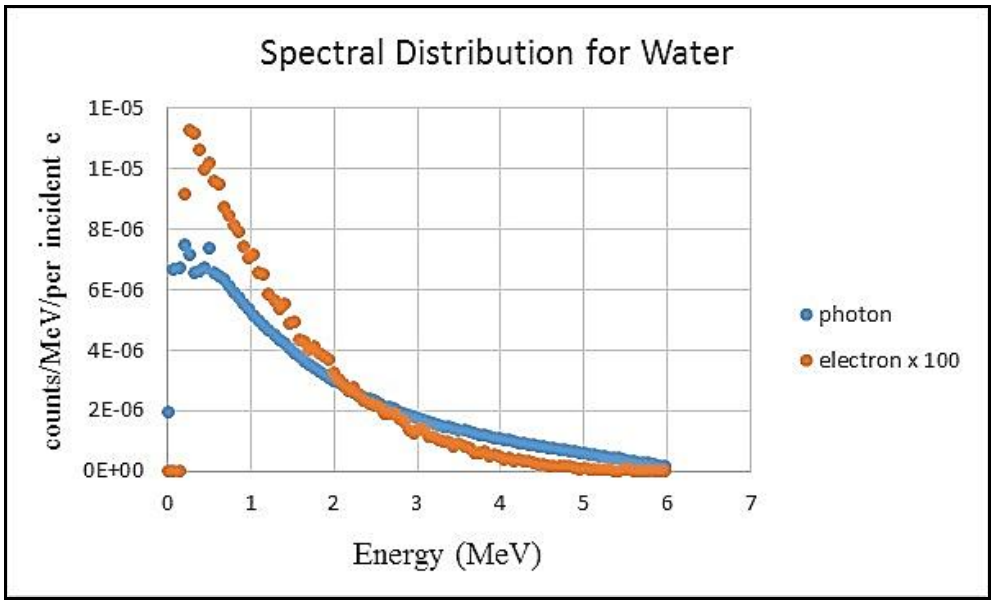

Graphic 5.6. The spectral distribution of photons and electrons at water phantom surface for the 10x10 cm2 field of a 6MV.

The table 5.5 and 5.6 were created using values of graphic 5.1, 5.2, 5.3, 5.4, 5.5, 5.6.

Table 5.5. Comparison of MC calculated and NIST values of mass collisional stopping power ratios. NIST values were based on Compton average equilibrium electron energy, and the Monte Carlo values were based on the electron spectrum analysis.

s/ρ (coll)	**NIST**	**Monte Carlo**	**Std. Dev. (%)**
LiF / BONE	0.899	0.901	0.2
LiF / LUNG	0.816	0.818	0.2
LiF / WATER	0.807	0.810	0.4

Table 5.6. Comparison of MC calculated and NIST values of mass energy absorption coefficient ratios. NIST values were based on the average photon energy while the Monte Carlo values are based on the photon spectrum analysis.

μ_{en} / ρ	**NIST**	**Monte Carlo**	**Std. (%)**
LiF/ BONE	0.898	0.889	1.0
LiF/ LUNG	0.840	0.843	0.3
LiF/ WATER	0.833	0.836	0.3

Step 2: DOSXYZnrc: *Setup 1:* Monte Carlo based *f* factors for the heterogeneous phantoms were calculated by dividing the dose in TLD with the dose in medium simulated with no TLD at the same position. This process was fulfilled by using MATLAB program. The .3ddose file, obtained from DOSXYZnrc, was read out with MATLAB. We observed the PDD and surface dose in the phantoms with MATLAB. MATLAB codes are given in Appendix E. The Table 5.7 summarizes the Monte Carlo results for *f* factor. These results show that *f* factors were not being changed too much with the TLD thicknesses ranged from 0.015 cm to 0.089 cm. As seen in the table 5.7, the maximum standard deviation of the f factors is 0.5 % in both bone and lung phantoms.

Table 5.7. Values of $(f)^{TLD}_{medium}$ factor calculated using Monte Carlo

	f values for LUNG			**f values for BONE**		
Thickness (cm)	**0.015**	**0.038**	**0.089**	**0.015**	**0.038**	**0.089**
TLD 1	0.827	0.834	0.837	0.905	0.892	0.891
TLD 2	0.831	0.842	0.839	0.901	0.895	0.893
TLD 3	0.827	0.836	0.836	0.893	0.895	0.892
TLD 4	0.828	0.834	0.839	0.897	0.896	0.892
Average	0.828	0.836	0.838	0.899	0.894	0.892
% Std.	0.2	0.4	0.2	0.5	0.2	0.1

Monte Carlo calculated $(f)^{TLD}_{water}$ for thin, medium and thick TLDs, listed in Table 5.8. The $(f)^{TLD}_{water}$ value was applied to the experimental results to find the values of $(f)^{TLD}_{medium}$ (see equation 4.14).

Table 5.8. Monte Carlo calculated $(f)^{TLD}_{water}$ factors that are used in the dose to medium conversion.

TLD Thickness	**0.015 cm**	**0.038 cm**	**0.089 cm**
$(f)^{TLD}_{water}$	0.833	0.837	0.840

Setup 2: The PDD curves were obtained from MC. The .egslst files were read out using excel page for setup 2. The deviation was less than 1%. Graphic 5.7 and graphic 5.8 shows PDD curves for bone in water and lung in water respectively.

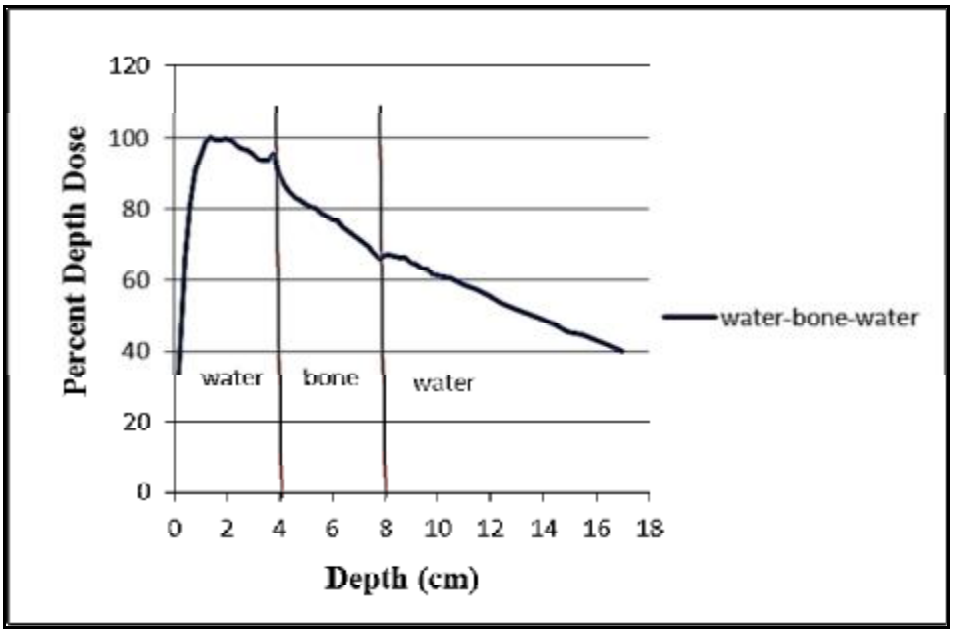

Graphic 5.7. PDD curve for water-bone-water phantom.

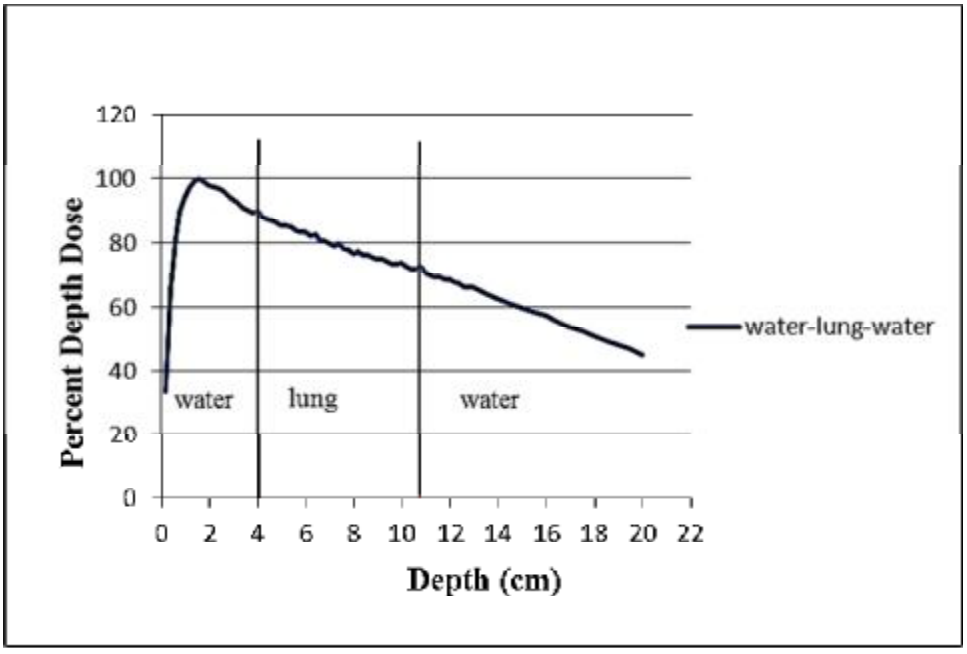

Graphic 5.8. PDD curve for water-lung-water phantom.

5.3. Experimental Results

As discussed in the 4.2.2.4, to convert the experimental dose to TLD to dose to medium, new parameter was inserted to the Equation 4.14. Using the Equation 4.14, the experimental $(f)_{\text{medium}}^{\text{TLD}}$ factors for both bone and lung heterogeneities

were calculated from the measured TLD charges and $(f)^{TLD}_{water}$ values which were calculated with Monte Carlo simulation. Table 5.9 and Graphic 5.9 demonstrate a good agreement between the $(f)^{TLD}_{medium}$ factors calculated using our proposed method in Equation 4.14, MC and theoretical results. The experimental data were summarized at Appendix A.

Table 5.9. Comparison of experimental, theoretical, and Monte Carlo calculated f factors in bone and lung heterogeneities.

	Thickness (cm)	**f Experimental**	**f Theoretical**	**f MC**	**STD. DEV.**
BONE	**0.015**	0.893	0.899	0.899	0.3%
	0.038	0.889	0.896	0.894	0.3%
	0.088	0.887	0.893	0.892	0.3%
LUNG	**0.015**	0.825	0.823	0.828	0.2%
	0.038	0.828	0.828	0.836	0.5%
	0.088	0.832	0.833	0.838	0.3%

The f factor for bone is observed to decrease slightly for bone while it increased slightly for lung with increasing TLD thickness. The results of the f are not the same but their standard deviations are less than 0.5%. The following graphic 5.9 shows the error bars according to the STD. DEV.

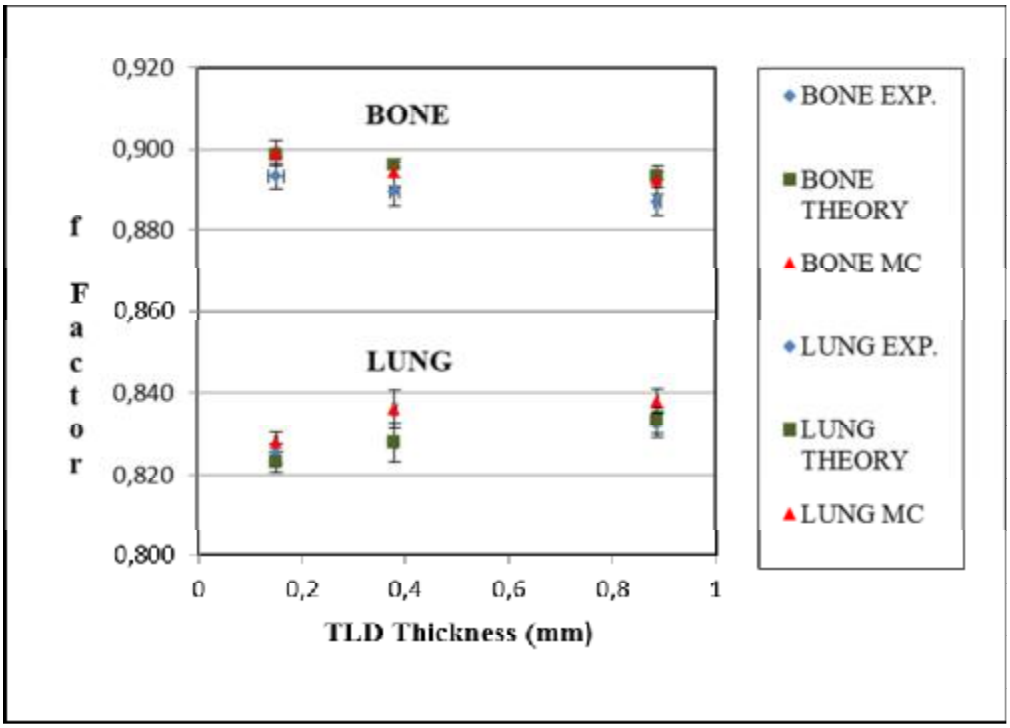

Graphic 5.9. Comparison of experimental, theoretical, and Monte Carlo calculated *f* factors in bone and lung heterogeneities.

5.4. Dose to Medium Verification Using Dose to Water Calibration Results

For dose to water calibration, the f factors were suggested in equation 4.18. After that the f factors were calculated using MC technique and the results were in section 5.2. Dose to medium conversions were done both using stopping power ratios and the f factors and compared with MC simulated dose to medium. TLD measurements were corrected both in the presence of both Bragg-Gray cavity theory and Burlin cavity theory using s/ρ_{water}^{medium} and f_{water}^{medium} respectively.

The table 5.11 and 5.12 introduce the TLD reading and PDD results. Graphic 5.10 shows EGSnrc based Monte Carlo calculated PDD curves for the A- cortical bone and B- lung hetereogeneity phantoms as it is depicted in Figure 4.17 including TLD measurements presented as dose to water and dose to medium.

Table 5.10. PDD values for water-bone-water phantom.

Depth (cm)	Dose to water (Gy) (%PDD)	Dose to medium: corrected with s/ρ_{water}^{medium} (Gy) (%PDD)	Dose to medium: corrected with f_{water}^{medium} (Gy) (%PDD)
1.5	100.00	100.00	100.00
3.5	92.36	92.36	92.36
4	94.27	84.62	88.77
4.5	88.60	79.53	83.44
5.5	80.08	71.88	75.41
6.5	73.32	65.81	69.04
7.5	67.25	60.37	63.33
8	60.69	60.69	60.69
8.5	60.63	60.63	60.63
10	53.49	53.49	53.49

Table 5.11. PDD values for water-lung-water phantom.

Depth (cm)	Dose to water (Gy) (%PDD)	Dose to medium: corrected with s/ρ_{water}^{medium} (Gy) (%PDD)	Dose to medium: corrected with f_{water}^{medium} (Gy) (%PDD)
1	98.211	98.211	98.211
1.5	100.000	100.000	100.000
4	89.768	88.778	89.982
6	83.590	82.668	83.789
8	78.278	77.415	78.465
10	71.876	71.083	72.047
11	69.891	69.891	69.891
13	63.377	63.377	63.377

A_

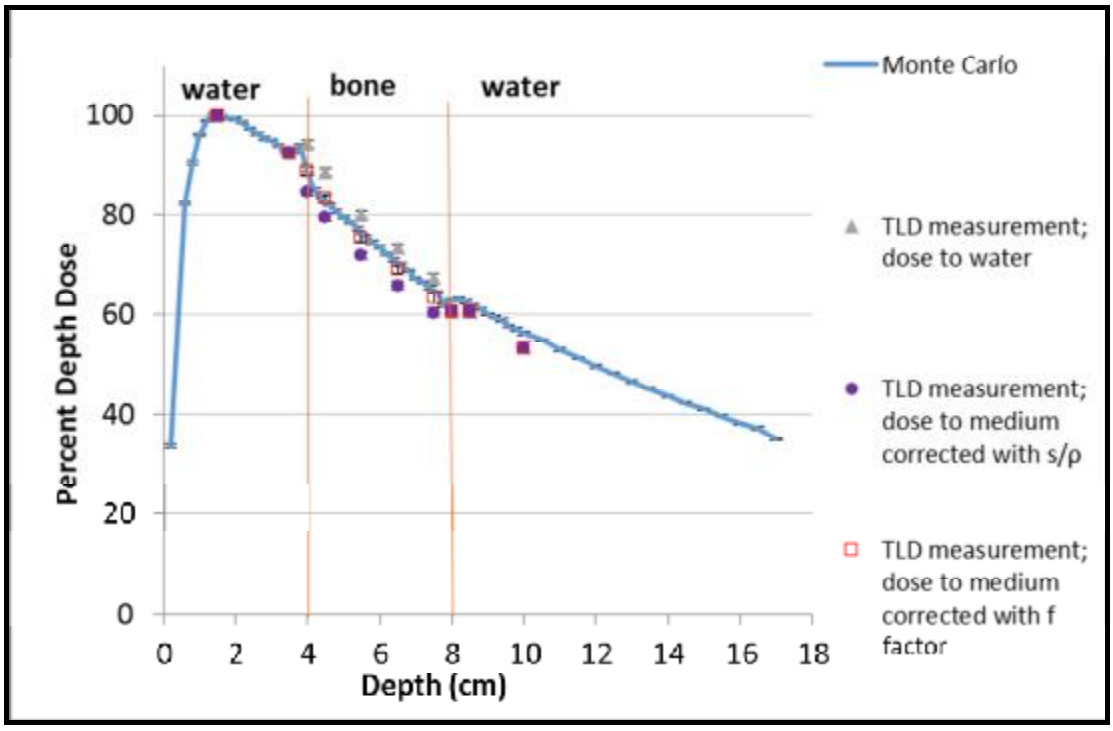

B_

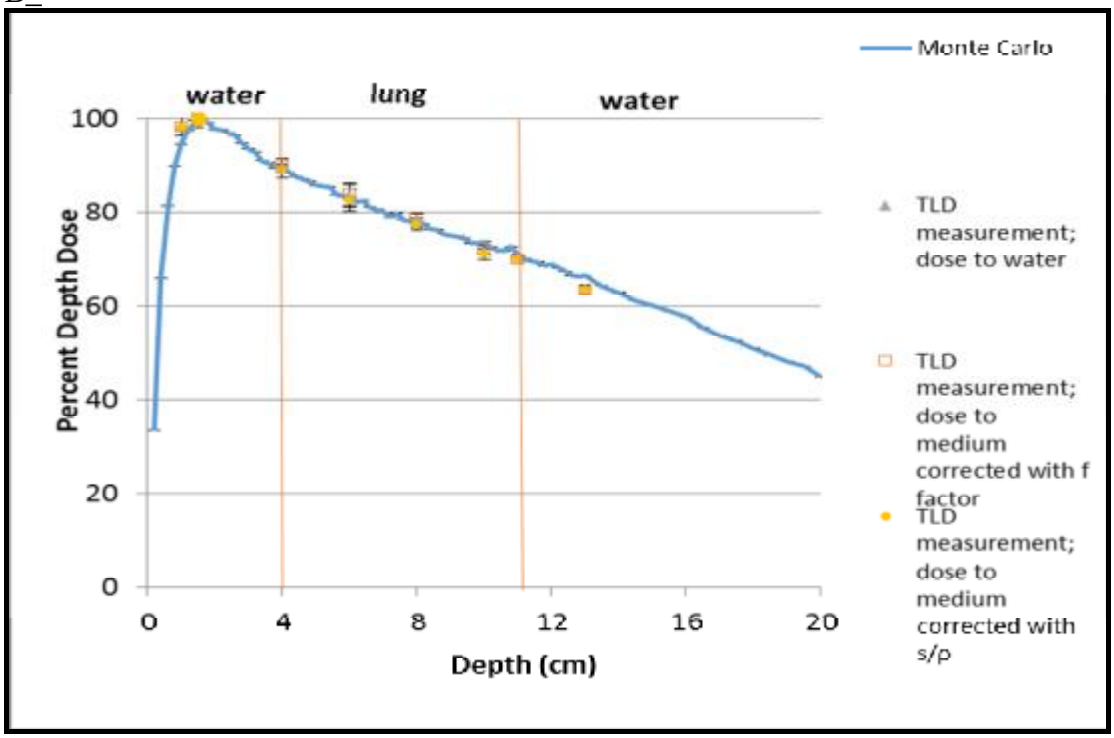

Graphic 5.10. EGSnrc based Monte Carlo calculated PDD curves for the A- cortical bone and B- lung heterogeneity phantoms as it is depicted in Figure 4.17 including TLD measurements presented as dose to water and dose to medium.

6. DISCUSSION AND CONCLUSION

Measurement of dose in heterogeneous mediums is a classical problem in radiotherapy and investigated by many researchers using MC simulations, experiments, and theoretical calculations. Bragg-Cavity theory is commonly used to convert the dose in TLD to the dose in medium using stopping power ratios as it is suggested. This approach provides correct results for lung, however, not for bone. This can be attributed to the fact that TLD, having similar effective Z, will not disturb the charge particle fluence that would existed if the cavity and the surrounding medium are of the same material. For high Z materials such as bone, however, having a low effective Z, TLDs will disturb the charge particle fluence. Hence, the use of stopping power ratios may not provide accurate results. With increasing the size of the detector, the fluence disturbance will increase, as such the dose measurement accuracy will be affected. For photon beams with energies higher than 400 keV, the TLD behaves like a medium-sized cavity for which Bragg-Gray cavity theory cannot be used. Burlin cavity theory, on the other hand, provided a framework for the dose to medium conversion for all detector sizes. Burlin cavity theory proposed a dose to medium conversion factor that depend on a parameter d that varies between unity for small (or Bragg–Gray) cavity and zero for large cavity. It is, indeed, the dose contribution resulting from photon interactions in the phantom material and accounts for the attenuation of electrons across the cavity (Burlin, 1966; Paliwal and Almond, 1975). It is however, very difficult, at the best, to determine parameter d for medium size dosimeters such as TLDs in heterogeneous mediums.

There are only a few study that investigated the response of TLD using Burlin cavity theory by either comparing with measurements or MC simulations. Materials investigated were included aluminum, LiF, lead, copper, water, and polystyrene. The study by Ogunleye et al. (Ogünleye, 1980) is the most comprehensive experiment performed, to date, in order to evaluate the Burlin cavity theory for TLDs. They reported a good agreement between the Burlin cavity theory and experimental results for polystyrene, but theory overestimated the TLD response in high Z materials such as aluminum, copper, and lead. Similar results were observed with MC simulations

later by Mobit et al. The agreement was within 1% for water, while there was a disagreement between Monte Carlo simulations and Burlin's theory of 6 and 12% for LiF TLDs irradiated in copper and lead phantoms respectively. Their study concluded that the Burlin expression is fairly successful for low Z materials while it failed for high Z materials.

No study were found to evaluate the Burlin cavity theory for TLD in bone and lung, which are the most important heterogeneities in radiological sciences. In addition, no study evaluated the value of the parameter d for TLDs that are used in clinic. Similarly, none of the manuscripts that evaluated the accuracy of the heterogeneity correction of treatment planning systems discussed about how they converted the dose to TLD to dose to medium (Reft et al.,2006). Thus, in this study, we systematically analyzed theoretical assumptions in calculating the parameter *d,* which was subsequently used to calculate the *f* factor using the Burlin cavity theory to convert the dose to TLD in medium to dose to medium. Comparison with MC simulation were within the deviation of 1%that of the Monte Carlo simulations for both lung and bone.

Furthermore, a simple experiment which is generally used to evaluate the accuracy of heterogeneity corrections of treatment planning systems was used to demonstrate that the Burlin cavity theory can be used to successfully estimate the dose to both lung and bone as long as the parameter d is known for the particular TLDs. This statement is confirmed using MC simulations.

Consequently, a practical framework to measure dose in medium is provided in this study that directly uses the readings from the TLD measurements in water and bone or lung and multiplying the ratio with the $(f)_{\text{medium}}^{\text{water}}$factor rather than estimating the parameter d for a particular TLD.

REFERENCES

AAPM REPORT NO. 85, 2004. Tissue Inhomogeneity Corrections for Megavoltage Photon Beams. Report of Task Group No. 65 of the Radiation Therapy Committee of the American Association of Physicists in Medicine.

AAPM Task Group No. 21, 1983. A protocol for the determination of absorbed dose from high energy photon and electron beam. Med. Phys., 14:741-771.

ABOU-HAIDAR, Z., et al., 2012. Output factor determination for dose measurements in axial and perpendicular planes using a silicon strip detector. Phys. Rev. ST Accel. Beams. 15:042802-1 - 7.

AHMED, S., N., 2007. Physics & Engineering of Radiation Detection, First edition. Academic Press – Elsevier. San Diego, USA. p68.

AHNESJO, A. and ASPRADAKIS, M. M., 1999. Dose calculations for external photon beams in radiotherapy. Phys. Med. Biol. 44:R99–R155.

ALMOND, P., R., and MCCRAY, K., 1970. The energy response of LiF, CaF2, and Li2B4O7: Mn to high energy radiations. Phys. Med. Biol. 15(2):335-42.

ANDERSEN, V., et al., 2005. The application of FLUKA to dosimetry and radiation therapy. Radiat Prot Dosimetry. 116 (1-4): 113-117.

ASCHAN C., 1999. Applicability of Thermoluminescent Dosimeters in X-Ray Organ Dose Determination and in the Dosimetry of Systemic and Boron Neutron Capture Radiotherapy, University Of Helsinki, Report Series in Physics, HU-P-D77.

ATTIX, F., H., 1986. Introduction to Radiological Physics and Radiation Dosimetry. Wiley-VCH Verlag GmbH & Co. KGaA, New York, NY. 607p.

ATTIX, F., H., 2004. Introduction to Radiological Physics and Radiation Dosimetry. 1st ed. Wiley-VCH Verlag GmbH & Co. KGaA, Weinheim. 628p.

AZORIN, 1990. Theory and Applications.

BABCOCK, K., K., R., 2009. The Effects of Anatomic Resolution, Respiratory Variations and Dose Calculation Methods on Lung Dosimetry, PhD Thesis, University of Saskatchewan. 183p.

BERGER, M., J., 1993. “ESTAR National Institute of Standards and Technology Physics Laboratory Ionizing Radiation Division” Technical Report No. NISTIR, 4999.

BERTILSSON, G., 1974. 4th Int. Conf. on Luminescence Dosimetry. Institute of Nuclear Physics, Krakow, Poland. 907p.

BLACK, A. R. and WATANABE, S, 1974. Physical parameters of glow peaks 4, 5 and 6 in TLD-100 (LiF:Mg,Ti). Revista Brasileira de Fisica, 4, No 2.

BOTTER-JENSEN, L., 1997. Luminescence techniques: instrumentation and methods. Radiation Measurements, 27: 749-68

BURLIN, T., E. and CHAN, F., K., 1969. The effect of the wall on the Fricke dosimeter. Int. J. Appl. Radiat. 20:767-775.

BURLIN, T., E., 1966. A general cavity theory of ionization. Br. J. Radiol. 39:727-734.

CARLSSON, G., A., 2001. Bragg-Gray Dosimetry: Theory of Burch Department of Medicine and Care Radio Physics Faculty of Health Sciences.

CARRASCO et al., 2004. Comparison of dose calculation algorithms in phantoms with lung equivalent heterogeneities under conditions of lateral electronic disequilibrium, Med. Phys. 31, 10.

CARRASCO et al., 2007. Comparison of dose calculation algorithms in slab phantoms with cortical bone equivalent heterogeneities, Med. Phys. 34 (8),

CECEN, Y., 2008. Monte Carlo Simulation in Radiotherapy, Hacettepe University PhD Thesis, pp: 19.

CHAN, F., K. and BURLIN, T., E., 1970. An experimental examination of a general cavity theory using a solid state dosimeter. Br. J. Radiol. 43:54-61.

CHEN, R. and MCKEEVER, S., 1997. Synthesis, characterization and investigation of thermoluminescence properties of strontium pyrophosphate doped with metals. Theory of Thermoluminescence and Relates Phenomena World Scientific Publishing Co. Pte. Ltd., Singapore,

CHERRY, P., DUXBURY, A., 2009. Practical Radiotherapy Physics and Equipment. 2nd Edition, Cambridge University Press, John Wiley & Sons. United Kingdom. 301p.

COOKE, D., W. and HOGSTROM, K., R., 1980. Thermoluminescent response of LiF and $Li_2B_40_7$:Mn to pions. Phys. Med. Biol. 25(4):657-666.

CURIE, D., 1960. Luminescence in Crystals. 1st edition. Methuen, London. 322p.

DANIELS, F., 1967. Early Studies of Thermoluminescence Radiation Dosimetry . In: Proc. Int. Conf. on Luminescence Dosimetry, Stanford, Ca. USA. US Atomic Energy Commission Conf-650637 (Springfield, Va: NTIS) pp. 34–43.

DAVIS, S., D., 2003. High Sensitivity Lithium Fluoride as a Detector for Environmental Dosimetry, B.Sc. Medical Physics Unit McGill University, 98p.

DEMARCO, J., CHETTY, I., and SOLBERG, T., 2002. A monte carlo tutorial and the application for radiotherapy treatment planning. Med Dosim. 27(1)1:43–50.

DOĞAN, N., SIEBERS, J., V. and KEALL, P., J., 2006. Clinical comparison of head and neck and prostate IMRT plans using absorbed dose to medium and absorbed dose to water. Phys. Med. Biol. 51:4967–4980.

DUNN, W., L. and SHULTIS, J., K., 2012. Exploring Monte Carlo Methods. Academic Press, Elsevier. Burlington, MD. 384p.

DUTREIX, J. and BERNARD, M., 1966. Dosimetry at Interfaces for High Energy X and Gamma Rays. Br. J. Radiol. 39:205-210.

EDY, A., A., 2012. A General Cavity Theory for Photon Beams. American Institute of Physics. 1423:373-378.

EHRLICH, M., 1971. 3rd Znt. Conf. on Luminescence Dosimetry, R150 Danish AEC, Riso, Denmark. 550p.

EKLÖF, A., AHNESIÖ, A., BRAHME, A., 1990. Photon Beam Energy Deposition Kernel for Inverse Radiotherapy Planning. Acta Oncologica, 29(4) 447 – 454.

EVANS, R.D., 1955. The Atomic Nucleus. McGraw-Hill, New York. 972p.

FAIRCHILD, R., G., MATTERN, P., L., LENGWEILER, and LEVY, P., W., 1978. Thermoluminescence of LiF TLD100: Glowcurve kinetics. Journal of Applied Physics. 49:4523-4533.

FANO, U., 1954. Note on the Bragg-Gray cavity principle for measuring energy dissipation. Radiation Res. 1237 – 1240.

FIPPEL, M., 2006. Monte Carlo Dose Calculation for Treatment Planning, p: 199.

FRAASS, B., A., 2003. Summary and recommendations of a National Cancer Institute workshop on issues limiting the clinical use of Monte Carlo dose calculation algorithms for megavoltage external beam radiation therapy. Med. Phys. 30(12):3206-16.

FURETTA, C., 2003. Handbook of Thermoluminescence. Word Scientific Publishing, Singopore, 482p.

GARLICK, G., F., J., 1949. Luminescent Materials. Oxford University Press, London. 254p.

GOWDA, S., et al., 2004. Photon mass attenuation coefficients, effective atomic numbers and electron densities of some thermoluminescent dosimetric compounds. Journal of Phys. 63(3):529-541.

HAIDER, J., A., 1995. Dosimetry studies of small fields in homogeneous and inhomogeneous media for high energy photons. The University of British Columbia PhD Thesis. 204p.

HARALDSSON, P., KNÖÖS, T., NYSTRÖM, H. and ENGSTRÖM, P., 2003. Monte Carlo study of TLD measurements in air cavities. Phys.Med. Biol. 48:253–259.

HOROWITZ, Y., S. and DUBI, A., 1982. A proposed modification of Burlin's general cavity theory for photons. Phys. Med. Biol., 27(6):867-870.

HOROWITZ, Y., S., MOSCOVITCH, M. and DUBI, A., 1983. Modified general cavity theory applied to the calculation of gamma dose in ^{60}Co thermoluminescence Dosimetry. Phys. Med. Biol. 28:829-840.

HOROWITZ, Y., S., OSTER, L. and DATZ, H., 2007. The thermoluminescence dose response and other characteristics of the high temperature TL in LiF:Mg, Ti (TLD-100). Radiation Protection Dosimetry, 124, 2: 191-205.

IAEA Report 277, 1987. International Atomic Energy Agency. Absorbed dose determination in photon and electron beams, Vienna, Austria.

ICRU Report 37, 1984. International Commission on Radiation Units and Measurements. Stopping powers for electrons and positrons. International commission on radiation units and measurements, Maryland, USA.

ICRU Report 398, 2000. International Commission on Radiation Units and Measurements. Determination of Absorbed Dose in a Patient Irradiated by Beams of X or Gamma Rays in Radiotherapy.

ILIC-POPOVIC, J., 1971. On the applicability of a solid-state Bragg-Gray cavity chamber for luminescence degradation dosimetry. Int. J. Appl. Radiat. Isotopes. 22(8):457-461.

JABLONSKI, A., 1935. Über den Mechanisms des Photolumineszenz von Farbstoffphosphoren. Z. Phys. 94:38-46.

JAIN, V., K., 1986. Thermoluminescence mechanism in LiF TLD-100 from 90 to 300K. J. Phys. D: Appl. Phys.19:1791-1807.

JANSSENS, A., EGGERMONT, G., JACOBS, R. and THIELENS, G., 1974. Spectrum perturbation and energy deposition models for stopping power. Phys. Med. Biol. 19:619-630.

JUSTE, B., MİRÓ, R., GALLARDO, S., SANTOS, A., VERDU, G., 2005. Considerations of MCNP Monte Carlo code to be used as a radiotherapy treatment planning tool. Conf Proc IEEE Eng Med Biol Soc. 3:2828-31.

KAISER, K., 2010. Performance Validation of a Prototype Skin Contamination Detector via Use of Very Thin Thermoluminescent Dosimetry, Master of Science Thesis, Oregon State University, Oregon, USA.

KARZMAK, 1965. Radiation Safety for Radiation Workers, 2005. University of Wisconsin Medison.

KAWRAKOW, I. and FIPPEL, M., 2000. Investigation of variance reduction techniques for monte carlo photon dose calculation using xvmc. Physics in Medicine and Biology. 45(8):2163–2184.

KAWRAKOW, I. and ROGERS, D., W., O., 2011. The EGSnrc Code System: Monte Carlo simulation of electron and photon transport, Technical Report PIRS–701, National Research Council of Canada, Ottawa, Canada.

KAWRAKOW, I., MAINEGRA-HING, E., ROGERS, D., W., O., TESSIER, F. and WALTERS B., R., B., 2009. The EGSnrc Code System: Monte Carlo Simulation of Electron and Photon Transport, Ionizing Radiation Standards NRC Canada.

KEARSLEY, E., 1984. A new general cavity theory. Phys. Med. Biol. **29**, 1179.

KHAN, F., M., 2003. The Physics of Radiation Therapy. 3rd Edition, Lippincott Williams & Wilkins. Philadelphia, USA. 560p.

KNOSS et al., 2006. Comparison of dose calculation algorithms for treatment planning in external photon beam therapy for clinical situations, PMB 51:5785-5807.

KORHONEN, L., 2009. Methods for dose calculation and beam characterization in external photon beam radiotherapy, PhD Thesis, Helsinki University of Technology, Helsinki.

KRON, T., 1995. Thermoluminescence dosimetry and its applications in medicine, Part 2: History and applications., Australas Phys. Eng. Sci. Med., 18(1):1-25.

KRON, T., 1999. Applıcatıons Of Thermolumınescence Dosımetry In Medıcıne, Radiation Protection Dosimetry Vol. 85, Nos. 1–4, pp. 333–340.

LAURENCE, G., C., 1937. The measurement of extra-hard X-rays and gamma-rays in roentgens. Can. J. Research. 15:67-78.

LEMOIGNE, Y. and CANER, A., 2009. Radiation Protection in Medical Physics, Springer, NATO Science for Peace and Security Series, France, 192p.

LI, C., LAMEL, L.S. and TOM, D., 1995. A patient dose verification program using diode detectors. Med. Dosim. 20, 209-214.

LOEVINGER, R., 1956. The Dosimetry of Beta Sources in Tissue. Radiology, 66:55-62.

LOWE, B., A., 1979. The Application of Cavity Theory to the Dosimetry of Electron Fields. Phys. Med. Biol. 24(1):162-165.

MA, C., M. et al., 2004. MCSIM—A Monte Carlo dose calculation tool for radiation therapy. In Proceedings of the 14th ICCR, Seoul, Korea, pp. 123–126.

MA, C., M. and ROGERS D. W. O., 2009. BEAMdp User Manual. Technical Report PIRS–0509C (RevA), National Research Council of Canada, Ottawa, Canada.

MAINEGRA- HING, E., 2011. NRC User Codes for EGSnrc, Technical Report PIRS–702(RevC), National Research Council of Canada, Ottawa, Canada.

MANOHARA, S., R. et al., 2008. On the effective atomic number and electron density: A comprehensive set of formulas for all types of materials and energies above 1 keV, 266(18):3906-3912.

MANSFIELD, C., M. and SUNTHARALINGAM, N., 1975. The usefulness of thermoluminescent dosimetry in clinical radiation therapy. In Proceedings of the International Symposium on Advances in Biomedical Dosimetry, International Atomic Energy Agency, Vienna. pp. 335-346.

MARTIN, J., E., 2006. Physics for Radiation Protection, 2nd ed., Wiley VCH, 332p.

MAUCERI, T. and KASE, K., 1987. Effects of ionization chamber construction on dose measurements in heterogeneity. Med. Phys. 14(4):653-6.

MAYLES, P., NAHUM, A., ROSENWALD, J., C., 2007.Handbook of Radiotherapy Physics. Theory and Practice. CRC Press, Taylor & Francis. FL, USA. 1425p.

MCKEEVER, S. W. S., 1985. Thermoluminescence of solids; CambridgeUniversity Press: Cambridge, UK.

MCKEEVER, S., MOSCOVITCH, M., TOWNSEND, P., 1995. Thermoluminescence Dosimetry Materials: Properties and Uses. Nuclear Technology Publishing, England. 204p.

McKINLAY, A., F, 1981. Thermoluminescence Dosimetry, Medical Physics Handbook 5 page: 17. Taylor & Francis; 1st edition. 270pp.

METCALFE, P., 2008. Radiobiology and Radiation Protection Lecture Notes, University of Wollongong.

METCALFE, P., KRON, T., HOBAN, P., 2007. The Physics of Radiotherapy X-Rays and Electrons, 1st edition. Medical Physics Publishing, Madison, WI. pp: 95-96.

MILJANIC, S. and RANOGAJEC-KOMOR, M., 1997. Application of cavity theory to the response of various TLDs to ^{60}Co gammas degraded in water. Phys. Med. Biol. 42:1335–1349.

MOBIT, P., N., NAHUM, A., E. and MAYLES, P., 1997. An EGS4 Monte Carlo examination of general cavity theory. Phys. Med. Biol. 42:1319–1334.

MOSCOVITCH, M., HOROWITZ, Y., S., 2007. Thermoluminescent materials for medical applications: LiF:Mg,Ti and LiF:Mg,Cu,P. Radiation Measurements 41:71–7.

NELSON, W., R., HIRAYAMA, H. and ROGERS, D., W., O., 1985. The EGS4 code system. Report No. SLAC-265, Stanford Linear Accelerator Center, Stanford, California.

NIETO, J., A., 2004.Thermoluminescence Dosimetry (TLD) and its Application in Medical Physics, AIP Conference Proceedings. 724(1):20.

NILSSON, B., RUDEN, B. and SORCINI, B., 1988. Characteristics of silicon diodes as patient dosimeters in external radiation therapy. Radiother. Oncol. 11, 279-288.

NIST; (http://www.physics.nist.gov/Divisions/Div846/Gp2/gp2.html) (Access time: 10.12.2013)

OGUNLEYE, O., T., ATTIX, F., H. and PALIWAL, B., R., 1980. University Comparison of Burlin cavity theory with LiF TLD measurements for cobalt-60 gamma rays. Phys. Med. Biol. 25(2):203-213.

OSEI, E., K., DARKO, J., MOSSERI, A. and JEZIORANSKI, J., 2003. EGSNRC Monte Carlo study of the effect of photon energy and field margin in phantoms simulating small lung lesions. Med. Phys. 30:2706–2714.

PAGANETTI, H., 2009. Dose to water versus dose to medium in proton beam therapy. Phys. Med. Biol. 54:4399–4421.

PALIWAL, B., R. and ALMOND, P., R., 1975. Applications of cavity theories for electrons to LiF dosimeters. Phys. Med. Biol. 20:547–58.

PHAM, T., M., 2009. Simulation of the Transmitted Dose in an EPID Using a Monte Carlo Method, University of Adelaide, Master thesis, pp: 32.

PODGORSAK, E., B., 2010. Radiation Physics for Medical Physicists. 2nd Edition, Springer-Verlag Berlin Heidelberg, 745p.

POON, E. and VERHAEGEN, F., 2005. Accuracy of the photon and electron physics in GEANT4 for radiotherapy applications. Med. Phys. 32:1696-1711,

PRADHAN, A., S., 1981. Thermoluminescence Dosimetry and Its Applications. Radiat Prot Dosimetry, 1(3): 153-167.

RADIATION SAFETY FOR RADIATION WORKERS, 2005. Wisconsin Madison; http://www.ehs.wisc.edu/rad/RadiationSafetyForRadiationWorkersTraining Manual. pdf (Access time: 10.12.2013)

RASHEEDY, M., S., 1996. A new method for obtaining the trap parameters of complex thermoluminescence glow peaks. J. Phys. D: Appl. Phys,. 29:1340–1344.

REFT, C. S., RUNKEL-MULLER, R. and MYRIANTHOPOULOS, L., 2006.In vivo and phantom measurements of the secondary photon and neutron doses for prostate patients undergoing 18 MV IMRT. Med. Phys., **33**, 3734.

RICE, J., A., 1995. Mathematical Statistics and Data Analysis. Belmont, CA: Duxbery Press. 688p.

RIKNER, G. and GRUSELL, E., 1987. General specifications for silicon semiconductors for use in radiation dosimetry. Phys. Med. Biol. 32, 1109-1117.

RIKNER, G. and GRUSELL, E., 1987. Patient dose measurements in photon fields by means of silicon semiconductor detectors. Med. Phys. 17, 870-873.

RIVERA, T., 2012. Thermoluminescence in Medical Dosimetry. Applied Radiation and Isotopes, 71:30–34.

ROGERS, D. W. O, MA, C. M., WALTERS, B., DING, G. X., SHEIKH-BAGHERI, D., ZHANG, G., 2002. BEAMnrc User's Manual. IRS, National Research Council of Canada, Ottawa.

ROGERS, D. W. O. and BIELAJEW, A., F., 1990. Monte Carlo Techniques of Electron and Photon Transport for Radiation Dosimetry. K1A/ OR6, National Research Council of Canada Ottawa, Canada. 445p.

ROGERS, D. W. O., FADDEGON B. A., DING, G. X., MA, C. M., WEI, J. and MACKIE, T. R., 1995. BEAM: A Monte Carlo code tosimulate radiotherapy treatment unitsMed. Phys.22503–24.

ROGERS, D., W., O., 2006. Fifty years of Monte Carlo simulations for medical physics. Phys. Med. Biol., 51:287-301.

ROGERS, D., W., O., KAWRAKOW, I., SEUNTJENS, J., P., WALTERS, B., R., B., 2009. BEAMnrc User Manual. Technical Report PIRS–0509A (RevL), National Research Council of Canada, Ottawa, Canada.

SAEEDI, F., YIN, Z. and HUGTENBURG, R. P., 2004. Dosimetry in conditions of electron disequilibrium, Radiation Physics and Chemistry, 71:979 – 980.

SELTZER, S., M., 1993. Calculation of Photon Mass Energy-Transfer and Mass Energy-Absorption Coefficients. Radiation Research, 136(2): 147-170.

SEMPAU, J., et al., 2001. Monte Carlo simulation of electron beams from an accelerator head using PENELOPE. Phys. Med. Biol.,46: 1163-86.

SHACHAR, B., B. and HOROWITZ, Y., S., 1993. Long-Term Fading of Peak 5 in TLD-100 Using Computerised Glow Curve Deconvolution (CGCD) and Thermal Peak Isolation Techniques, 47(1-4): 181-185.

SIDEK, M., A., J., 2010. Monte Carlo investigations of radiotherapy beams: Studies of conventional, stereotactic and unflattened beams, PhD Thesis, The University of Birmingham, Birmingham, England.

SIEBERS, J., V., KEALL, P., J., NAHUM, A., E. and MOHAN, R., 2000. Converting absorbed dose to medium to absorbed dose to water for Monte Carlo based photon beam dose calculations. Phys. Med. Biol., 45:983–995.

SILVA, H., 1989. An analysis of the electron spectrum effect on LiF response to cobalt-60 gamma-rays. Nuclear Instruments and Methods in Physics Research B44166-171.

SPENCER, L., V., and ATTIX, F., H., 1955. A theory of cavity ionization. Radia. Res., 3:239-254.

STERNHEIMER, R., M., 1952. The Density Effect for the Ionization Loss in Various Materials. Physical Review, 88(4):851-859.

SVENSSON, H. and BRAHME, A., 1986. Recent advances in electron and photon dosimetry in: Radiation Dosimetry. Physical and Biological Aspects. Orton, C.G. (ed.). New York: Plenum Press.

TURNER, A., P. and ANDERSON, D., W., 1973. Thermoluminescent response of lithium fluoride to high energy photons. Phys. Med. Biol., 18:46-52.

TURNER, J., E., 2004. Atom, Radiation and Radiation Protection, 2nd ed. Wiley-VCH, 606p.

VALEUR, B. and BERBERAN-SANTOS, M., N., 2011. A Brief History of Fluorescence and Phosphorescence before the Emergence of Quantum Theory. J. Chem. Educ., 88:731-738.

WALTER, R., N., 2008. History and Overview of EGS4; http://rcwww.kek.jp/research/egs/docs/pdf/History_and_Overview.pdf (Access time: 10.12.2013)

WALTERS, B., KAWRAKOW, I., ROGERS, D., W., 2005. DOSXYZnrc User's Manual. Technical Report No. PIRS-794(RevB), National Research Council of Canada, Ottawa, Canada.

WALTERS, B., R., B. and ROGERS, D., W., O., 2001. BEAMnrc User's Manual. Technical Report No. PIRS-0509(A) revG, Canada.

WANG, J., 2002. Thermolumınescence Excitation Spectroscopy: A Technique To Study Energy Levels Of Impurity In Solids, Master Thesis, University of Georgia, Athens, Georgia.

YIN, Z., HUGTENBURG, R., P. and BEDDOE, A., H., 2004. Response corrections for solid-state detectors in megavoltage photon Dosimetry. Phys. Med. Biol., 49:3691 – 3702.

ZAIDI, H., 2003. The Monte Carlo method: theory and computational issues, Therapeutic Applications of Monte Carlo Calculations in Nuclear Medicine, Chapter 1, pp: 6-7-13.

ZHOU, H., 2009. A bone composition model for Monte Carlo x-ray transport simulations. AAPM.

CURRICULUM VITAE

Neslihan SARIGÜL was born on 1983, in Mersin. She graduated with a degree of Bachelor of Science (B.Sc) in Physics Education from Gazi University, Ankara, Turkey in 2006. She started her Ph.D education in Physics Department at Çukurova University, Adana, Turkey in 2010. She is an academic specialist at Hacettepe University Institute of Nuclear Science since 2013. She is married and has a son.

APPENDICES

APPENDIX A

The TLD sensitivities and experimental data.

The Figure 1, 2 and 3 show sensitivity and uncertainty for TLDs of 0.015, 0.038 and 0.0889 cm respectively.

	20.1.2012 (115 MU)		23.1.2012 (115 MU)		27.1.2012 (115 MU)		9.3.2012 (115 MU)		average	average	
TLD	reading 1 (nC)	sensitivity 1	reading 2 (nC)	sensitivity 2	reading 3 (nC)	sensitivity 3	reading 4 (nC)	sensitivity 4	reading	sensitivity	uncertainty
1	69,536	0,9520	69,3	0,9603	69,3	0,9581	65,554	0,9640	68,423	0,9586	0,5%
2	71,157	0,9303	72,7	0,9154	71,4	0,9299	69,016	0,9156	71,068	0,9228	0,8%
3	67,006	0,9880	66,7	0,9977	67	0,9910	63,87	0,9894	66,144	0,9915	0,4%
4	61,375	1,0786	61,7	1,0786	61,3	1,0831	57,062	1,1074	60,359	1,0869	1,4%
5	57,248	1,1564	58,1	1,1454	57	1,1648	55,244	1,1439	56,898	1,1526	1,0%
6	66,573	0,9944	66,9	0,9947	66,8	0,9939	63,539	0,9946	65,953	0,9944	0,0%
7	68,652	0,9643	69,1	0,9631	68,8	0,9650	64,63	0,9778	67,796	0,9675	0,7%
8	64,166	1,0317	63,7	1,0447	63,7	1,0423	61,78	1,0229	63,337	1,0354	1,0%
9	58,049	1,1404	57,6	1,1554	57,1	1,1628	55,318	1,1424	57,017	1,1502	1,1%
10	69,957	0,9463	72,2	0,9217	70,3	0,9444	69,2	0,9132	70,414	0,9314	1,7%
11	66,016	1,0028	66,6	0,9992	66,6	0,9969	broken		66,405	0,9996	0,3%
12	74,478	0,8889	73,9	0,9005	73,1	0,9083	49,451	1,2779	67,732	0,9939	19,0%
13	67,579	0,9796	68,1	0,9772	67,2	0,9880	71,796	0,8802	68,669	0,9563	5,1%
14	52,284	1,2662	52,1	1,2773	50,1	1,3252	64,35	0,9820	54,709	1,2127	15,6%
15	61,331	1,0794	61,1	1,0892	60,9	1,0902	58,484	1,0805	60,454	1,0848	0,6%
16	63,396	1,0442	63,8	1,0431	63,2	1,0505	59,274	1,0661	62,418	1,0510	1,1%
17	61,325	1,0795	61	1,0910	60,7	1,0938	57,865	1,0921	60,223	1,0891	0,6%
18	66,029	1,0026	65,3	1,0191	65,8	1,0090	61,808	1,0224	64,734	1,0133	0,9%
19	66,561	0,9946	66,2	1,0053	66,9	0,9924	60,692	1,0412	65,088	1,0084	2,3%
20	73,645	0,8989	74,2	0,8969	74,5	0,8912	70,908	0,8912	73,313	0,8945	0,4%
21	67,277	0,9840	68,4	0,9729	67,9	0,9778	64,42	0,9809	66,999	0,9789	0,5%
22	67,241	0,9845	67,9	0,9801	68,1	0,9750	66,262	0,9537	67,376	0,9733	1,4%
23	76,247	0,8682	76,6	0,8688	75,3	0,8817	73,307	0,8620	75,364	0,8702	0,8%
24	66,908	0,9894	65,5	1,0160	66,7	0,9954	64,523	0,9794	65,908	0,9951	1,5%
25	67,475	0,9811	66,6	0,9992	66,3	1,0014	64,532	0,9792	66,227	0,9903	1,2%
26	58,872	1,1245	59,5	1,1185	59,4	1,1178	56,624	1,1160	58,599	1,1192	0,4%
27	72,778	0,9096	73,2	0,9091	70,8	0,9378	68,333	0,9248	71,278	0,9203	1,4%
28	64,678	1,0235	65,2	1,0207	65,5	1,0137	61,732	1,0237	64,278	1,0204	0,5%
29	60,38	1,0964	62,5	1,0648	61	1,0884	57,818	1,0930	60,425	1,0856	1,4%
30	64,422	1,0276	64,7	1,0286	66,9	0,9924	62,248	1,0152	64,568	1,0160	1,7%
31	75,794	0,8734	76,2	0,8733	76,8	0,8645	73,23	0,8629	75,506	0,8686	0,6%
32	69,156	0,9573	69,1	0,9631	69,7	0,9526	63,996	0,9874	67,988	0,9651	1,6%
33	66,754	0,9917	66,3	1,0038	68	0,9764	61,579	1,0262	65,658	0,9995	2,1%
34	67,497	0,9808	67,7	0,9830	67,4	0,9851	64,207	0,9842	66,701	0,9833	0,2%
35	67,515	0,9805	69,1	0,9631	69,5	0,9553	65,87	0,9594	67,996	0,9646	1,1%
36	62,881	1,0528	65,9	1,0098	67,3	0,9865	62,717	1,0076	64,700	1,0142	2,8%
37	67,175	0,9855	67,6	0,9844	68,3	0,9721	63,701	0,9920	66,694	0,9835	0,8%
Average	**66,200**		**66,549**		**66,395**		**63,193**				
NOTE : The average backround TLs were subtracted from readings.											

Figure 1. The sensitivities and uncertainties for TLDs of 0.015 cm

	20.1.2012 (115 MU)		23.1.2012 (150 MU)		30.1.2012 (115 MU)		9.3.2012 (115 MU)		average	average	
TLD	**reading 1 (nC)**	**sensitivity 1**	**reading 2 (nC)**	**sensitivity 2**	**reading 3 (nC)**	**sensitivity 3**	**reading 4 (nC)**	**sensitivity 4**	**reading**	**sensitivity**	**uncertainty**
1	148,423	1,1178	201	1,1343	148	1,1241	146,722	1,1068	161,036	1,1208	1,2%
2	177,77	0,9333	242	0,9421	177	0,9399	172,211	0,9430	192,245	0,9396	0,4%
3	144,58	1,1475	198	1,1515	145	1,1473	142,419	1,1402	157,500	1,1466	0,5%
4	171,586	0,9669	236	0,9661	171	0,9729	168,448	0,9640	186,759	0,9675	0,4%
5	168,129	0,9868	227	1,0044	168	0,9902	164,657	0,9862	181,947	0,9919	0,9%
6	171,985	0,9647	235	0,9702	167	0,9962	168,303	0,9649	185,572	0,9740	1,5%
7	168,115	0,9869	226	1,0088	168	0,9902	163,521	0,9931	181,409	0,9948	1,0%
8	152,078	1,0910	207	1,1014	151	1,1017	147,46	1,1012	164,385	1,0988	0,5%
9	163,318	1,0159	226	1,0088	167	0,9962	162,888	0,9969	179,802	1,0045	1,0%
10	166,784	0,9948	225	1,0133	165	1,0083	163,441	0,9936	180,056	1,0025	1,0%
11	172,284	0,9630	233	0,9785	178	0,9346	170,077	0,9548	188,340	0,9577	1,8%
12	167,56	0,9902	229	0,9956	166	1,0022	165,338	0,9822	181,975	0,9925	0,8%
13	164,887	1,0062	225	1,0133	164	1,0144	159,021	1,0212	178,227	1,0138	0,6%
14	165,781	1,0008	226	1,0088	162	1,0269	162,043	1,0021	178,956	1,0097	1,2%
15	163,544	1,0145	222	1,0270	162	1,0269	159,836	1,0160	176,845	1,0211	0,7%
16	169,051	0,9814	230	0,9913	165	1,0083	168,243	0,9652	183,074	0,9865	1,8%
17	165,034	1,0053	227	1,0044	166	1,0022	161,563	1,0051	179,899	1,0043	0,1%
18	173,22	0,9578	240	0,9500	173	0,9616	168,475	0,9639	188,674	0,9583	0,6%
19	133,231	1,2453	184	1,2391	133	1,2508	131,847	1,2317	145,520	1,2417	0,8%
20	162,696	1,0198	223	1,0224	162	1,0269	156,158	1,0399	175,964	1,0273	0,9%
21	169,257	0,9802	233	0,9785	168	0,9902	163,701	0,9920	183,490	0,9853	0,7%
22	196,305	0,8452	272	0,8382	192	0,8665	193,644	0,8386	213,487	0,8471	1,3%
23	140,756	1,1787	192	1,1875	141	1,1799	135,44	1,1990	152,299	1,1863	0,9%
24	160,597	1,0331	222	1,0270	163	1,0206	156,033	1,0407	175,408	1,0304	0,9%
25	214,121	0,7748	300	0,7600	217	0,7666	211,378	0,7682	235,625	0,7674	0,6%
26	166,392	0,9971	225	1,0133	165	1,0083	162,726	0,9979	179,780	1,0042	0,8%
27	153,8	1,0787	211	1,0806	155	1,0733	147,511	1,1009	166,828	1,0834	1,2%
28	152,963	1,0846	211	1,0806	155	1,0733	151,458	1,0722	167,605	1,0777	0,6%
29	181,148	0,9159	256	0,8906	184	0,9041	179,373	0,9053	200,130	0,9040	1,0%
30	160,783	1,0319	224	1,0179	163	1,0206	158,573	1,0241	176,589	1,0236	0,6%
31	167,219	0,9922	227	1,0044	167	0,9962	162,674	0,9983	180,973	0,9978	0,5%
32	147,33	1,1261	200	1,1400	145	1,1473	142,265	1,1415	158,649	1,1387	0,9%
33	175,679	0,9444	240	0,9500	178	0,9346	171,718	0,9457	191,349	0,9437	0,6%
34	183,337	0,9049	248	0,9194	184	0,9041	180,309	0,9006	198,912	0,9073	0,8%
35	142,872	1,1613	197	1,1574	144	1,1553	138,238	1,1747	155,528	1,1622	0,9%
36	165,85	1,0004	226	1,0088	167	0,9962	166,713	0,9741	181,391	0,9949	1,5%
37	167,674	0,9895	232	0,9828	170	0,9786	163,657	0,9923	183,333	0,9858	0,6%
38	156,203	1,0621	216	1,0556	157	1,0596	154,072	1,0540	170,819	1,0578	0,4%
39	162,29	1,0223	224	1,0179	162	1,0269	158,665	1,0235	176,739	1,0226	0,4%
40	152,094	1,0908	206	1,1068	155	1,0733	149,261	1,0880	165,589	1,0897	1,4%
41	165,355	1,0034	232	0,9828	167	0,9962	162,21	1,0011	181,641	0,9959	0,9%
42	157,825	1,0512	221	1,0317	160	1,0398	154,682	1,0498	173,377	1,0431	0,9%
43	228,651	0,7256	324	0,7037	230	0,7233	223,004	0,7282	251,414	0,7202	1,1%
44	159,863	1,0378	225	1,0133	163	1,0206	156,607	1,0369	176,118	1,0272	1,2%
45	164,75	1,0070	230	0,9913	169	0,9844	162,373	1,0001	181,531	0,9957	1,0%
46	171,704	0,9663	233	0,9785	175	0,9506	165,14	0,9833	186,211	0,9697	1,5%
47	162,928	1,0183	227	1,0044	165	1,0083	158,232	1,0263	178,290	1,0143	1,0%
Average	**165,911**		**228,000**		**166,362**		**162,390**				
NOTE : The average backround TLs were subtracted from readings.											

Figure 2. The sensitivities and uncertainties for TLDs of 0.038 cm

	20.1.2012 (115 MU)		23.1.2012 (150 MU)		30.1.2012 (115 MU)		9.3.2012 (115 MU)		average	average	
TLD	**reading 1 (nC)**	**sensitivity 1**	**reading 2 (nC)**	**sensitivity 2**	**reading 3 (nC)**	**sensitivity 3**	**reading 4 (nC)**	**sensitivity 4**	**reading**	**sensitivity**	**uncertainty**
1	385,01	1,0840	513	1,0885	386	1,0842	359,927	1,0876	410,984	1,0861	0,2%
2	414,741	1,0063	552	1,0116	416	1,0061	385,141	1,0164	441,971	1,0101	0,5%
3	232,161	1,7978	318	1,7560	236	1,7734	220,051	1,7789	251,553	1,7765	1,7%
4	246,233	1,6950	332	1,6819	242	1,7294	234,075	1,6723	263,577	1,6947	2,5%
5	386,181	1,0808	523	1,0677	385	1,0871	363,661	1,0764	414,461	1,0780	0,8%
6	479,24	0,8709	626	0,8920	468	0,8943	445,391	0,8789	504,658	0,8840	1,1%
7	484,357	0,8617	653	0,8551	491	0,8524	446,224	0,8773	518,645	0,8616	1,1%
8	434,289	0,9610	579	0,9644	434	0,9643	406,012	0,9641	463,325	0,9635	0,2%
9	451,504	0,9244	588	0,9497	438	0,9555	409,804	0,9552	471,827	0,9462	1,5%
10	464,393	0,8987	634	0,8808	466	0,8981	432,323	0,9055	499,179	0,8958	1,1%
11	394,511	1,0579	519	1,0759	390	1,0731	376,342	1,0402	419,963	1,0618	1,6%
12	402,929	1,0358	539	1,0360	409	1,0233	373,94	1,0468	431,217	1,0355	1,0%
13	463,571	0,9003	604	0,9245	465	0,9000	439,37	0,8909	492,985	0,9040	1,4%
14	469,263	0,8894	618	0,9036	460	0,9098	435,515	0,8988	495,695	0,9004	0,9%
15	544,28	0,7668	736	0,7587	555	0,7541	509,236	0,7687	586,129	0,7621	0,7%
16	249,154	1,6751	338	1,6521	257	1,6285	236,145	1,6577	270,075	1,6533	1,9%
17	426,955	0,9775	558	1,0007	433	0,9666	396,391	0,9875	453,587	0,9831	1,5%
18	392,186	1,0642	523	1,0677	403	1,0385	375,085	1,0436	423,318	1,0535	1,5%
19	433,418	0,9630	587	0,9513	440	0,9512	412,813	0,9483	468,308	0,9534	0,7%
20	466,969	0,8938	622	0,8977	465	0,9000	434,793	0,9003	497,191	0,8980	0,3%
21	512,161	0,8149	687	0,8128	510	0,8206	484,469	0,8080	548,408	0,8141	0,5%
22	420,637	0,9922	572	0,9762	417	1,0036	395,633	0,9894	451,318	0,9904	1,1%
23	470,536	0,8870	641	0,8711	477	0,8774	443,747	0,8822	508,071	0,8794	0,7%
24	401,712	1,0390	541	1,0322	405	1,0334	376,558	1,0396	431,068	1,0360	0,4%
25	407,813	1,0234	557	1,0025	415	1,0085	393,711	0,9943	443,381	1,0072	1,2%
Average	**417,368**		**558,400**		**418,520**		**391,454**				
NOTE : The average backround TLs were subtracted from readings.											

Figure 3. The sensitivities and uncertainties for TLDs of 0.089 cm

The following Figure 4 shows the experimental results. The data were obtained from 0.0152, 0.038, 0.089 cm TLDs which were irradiated in lung, bone and water phantoms respectively. Some TLD results were eliminated because their results were so different from the others.

APPENDIX B

BEAMnrc input parameters for phase space data were created on bone surface

This Appendix gives information about how the phase space data were created on the bone phantom surface. To create it, the BEAMnrc GUI (see Figure 5) was used. We can summarize in seven step how the phase space data were created for only bone phantom. The bone and TLD were designed as slabs.

Not	The average background TL was subrtacted from reading						
		1.exp.	2.exp.	3.exp.	1.exp.	2.exp.	3.exp.
	TLD number	TL nC	TL nC	TL nC	TL X Sensitivity		
0.0152 cm	1	58,62	56,90	55,48	56,19	54,55	53,18
lung	7	45,29	61,50	57,79	43,82	59,50	55,91
	21	58,08	58,69	55,72	56,86	57,46	54,55
	22	59,86	60,70	56,90	58,27	59,08	55,38
	32	58,08	59,55	55,68	56,05	57,48	53,74
	37	57,17	56,90		56,22	55,96	
	35			56,69			54,68
0.0152 cm	3	59,17	58,87	53,93	58,67	58,37	53,47
bone	6	61,90	59,75	57,41	61,56	59,42	57,08
	8		58,79			60,87	
	14						
	17						
	18	58,39	57,94	56,11	59,17	58,71	56,86
	19	57,88	57,01	54,16	58,36	57,49	54,61
	28	56,63	56,62	54,70	57,79	57,78	55,82
	26			50,85			56,91
0.0152 cm	2	56,00	56,17	51,22	51,68	51,84	47,27
water	4	47,10	45,78	42,84	51,19	49,76	46,56
	5	45,30	43,60	41,82	52,21	50,25	48,20
	7	45,30			43,83		
	8	49,30		49,54	51,05		51,29
	9		43,98	43,08		50,58	49,56
	10		55,58			51,77	
	12		56,11			55,77	
	15			45,28			49,12
	16			46,52			48,89
0.038 cm	2	160,98	159,28	156,56	151,25	149,66	147,10
lung	4	157,96	166,20	149,27	152,82	160,79	144,41
	18	156,67	156,99	153,22	150,14	150,45	146,84
	21	151,96	156,91	147,15	149,72	154,60	144,98
	33	162,21	166,67	154,74	153,08	157,28	146,03
	37	152,28	156,12	148,61	150,12	153,90	146,50
0.038 cm	13	151,98	157,81	149,18	154,07	159,98	151,23
bone	15	149,71	155,79	146,28	152,87	159,08	149,37
	20	150,11	156,88	147,35	154,20	161,15	151,36
	24	151,10	154,76	147,57	155,69	159,46	152,05
	30	155,44	155,48	146,69	159,11	159,16	150,15
	39	152,20	157,17	147,87	155,65	160,73	151,22
0.038 cm	1		124,48	116,37		139,51	130,43
water	3		123,10	114,76		141,15	131,58
	5	140,00	141,68	132,98	138,87	140,53	131,91
	6	140,00	143,89	134,33	136,36	140,14	130,83
	7	137,00	139,64	131,07	136,28	138,91	130,39
	8	126,00	128,63	119,50	138,45	141,34	144,03
	9	140,00					
0.089 cm	21	459,02	474,52	482,46	373,68	386,30	392,77
lung	7		447,35	445,33		385,45	383,70
	23	431,34	442,03	436,03	379,33	388,74	383,46
	10	428,60	439,69	434,80	383,92	393,86	389,48
	20	415,49	424,16	417,98	373,10	380,88	390,44
	14	413,59	424,74	431,74	372,40	382,43	388,74
0.089 cm	2	383,49	392,96	392,78	387,36	396,93	396,74
bone	12	370,51	377,40	379,42	382,25	390,79	392,88
	24	377,29	382,50	383,81	390,88	396,28	397,63
	11	373,34	370,79		396,41	393,70	
	5	358,60	367,52	372,57	386,56	396,18	401,63
	1	361,41	364,59	370,04	392,52	395,98	401,89
	22			397,60			393,77
0.089 cm	3	182,00	193,84		323,32	344,35	
water	4	195,00	203,53		330,46	344,92	
	6	376,00	396,32	397,79	332,39	350,35	351,65
	8	344,00	369,22	373,33	331,44	355,74	359,70
	9		379,45	372,48		359,04	352,44
	13		375,25	387,08		339,21	349,90
	17			354,88			348,88
	19			359,14			342,41
	25			349,46			351,97

Figure 4: Experimental data

Step1: The BEAMnrc Gui was opened and the "Specify a new accelerator" was selected.

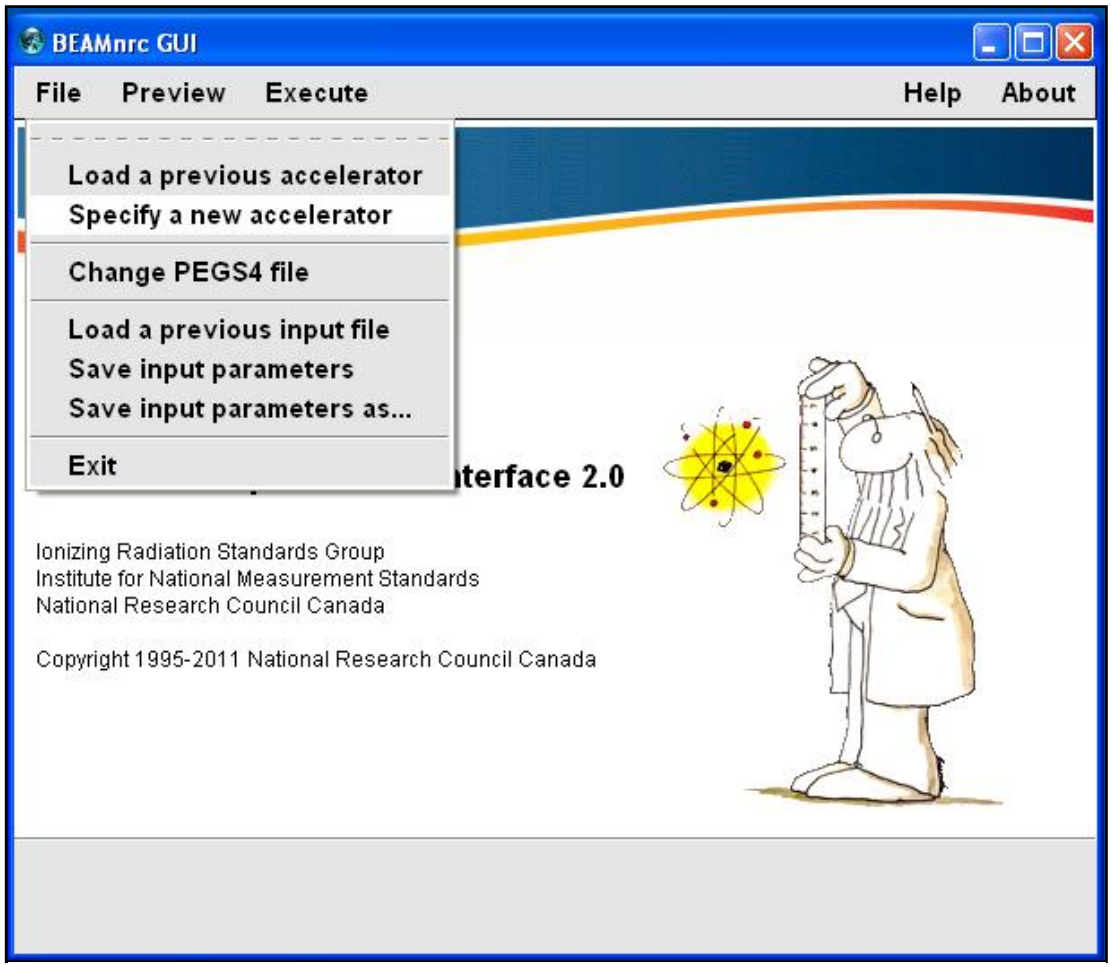

Figure 5: BEAMnrc gui.

Step 2: Three SLABS were created (see Figure 6) and the information were entered the system.

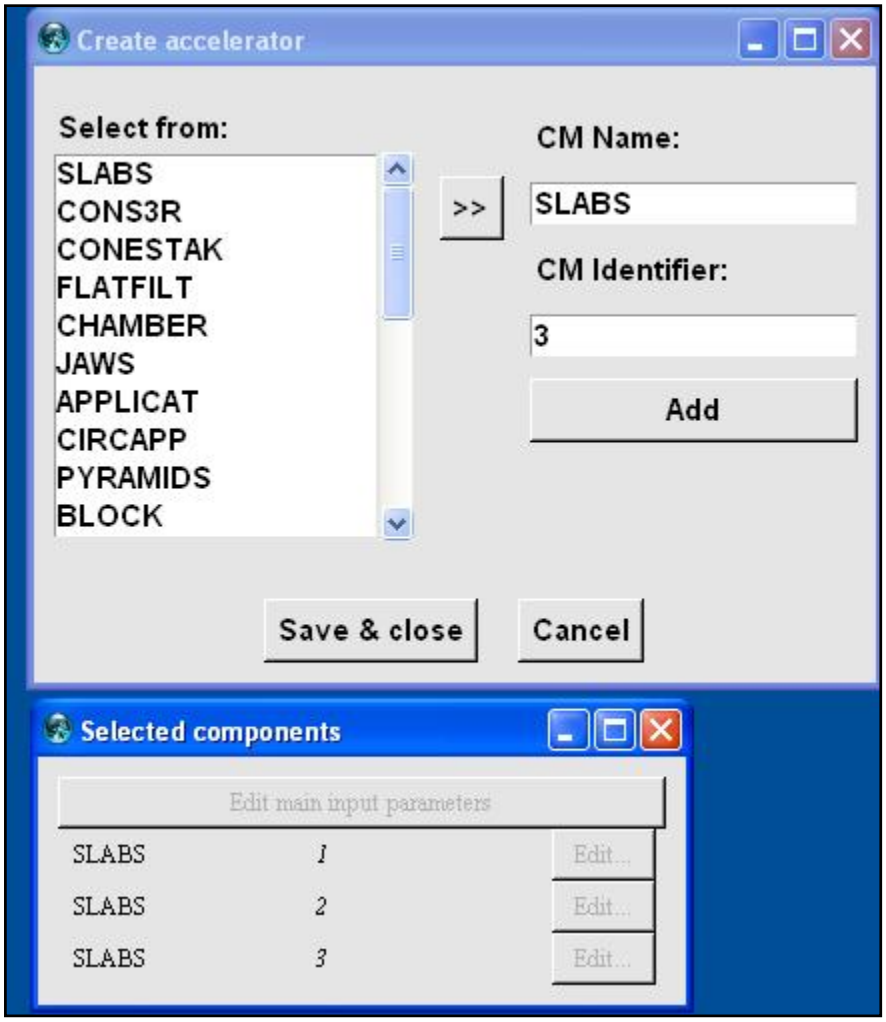

Figure 6: Create slabs using create accelerator section.

Step 3: The slabs were saved so the new module was created. The module name was "myphantom". After that the pegs4 data was selected as 700 icru.

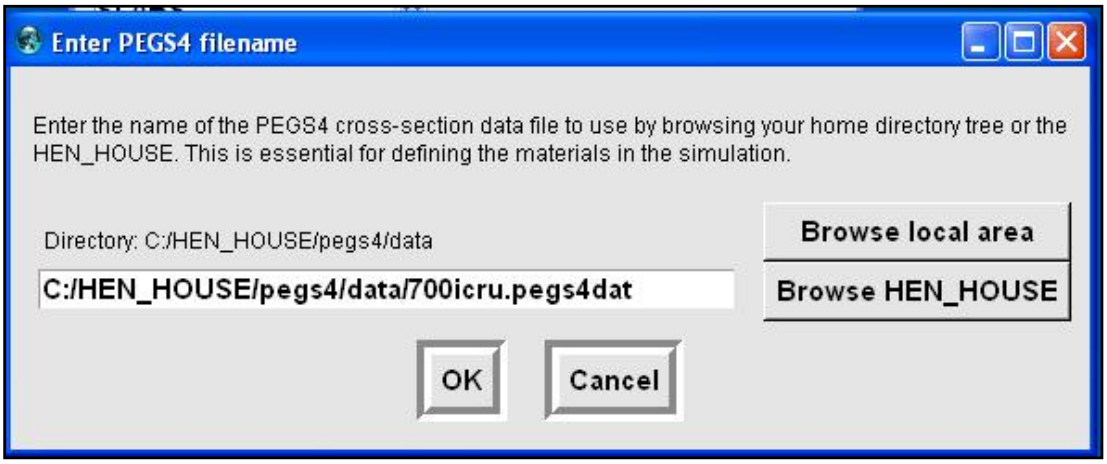

Figure 7: The PEGS4 File

Step 4: The slabs information were entered the system as defined in the following Figure 8, Figure 9 and Figure 10.

- **Slab 1: for bone**

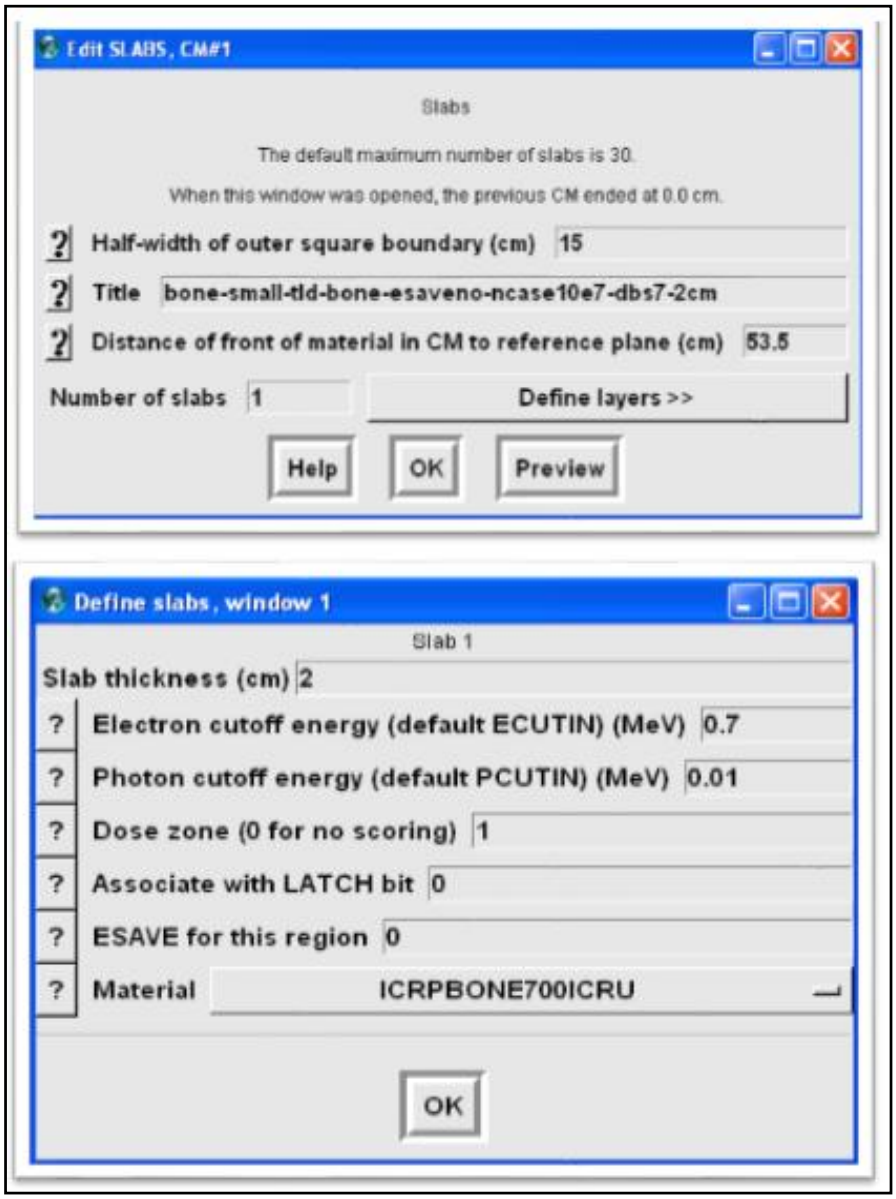

Figure 8: Information of CM1

- **Slab 2: for TLD**

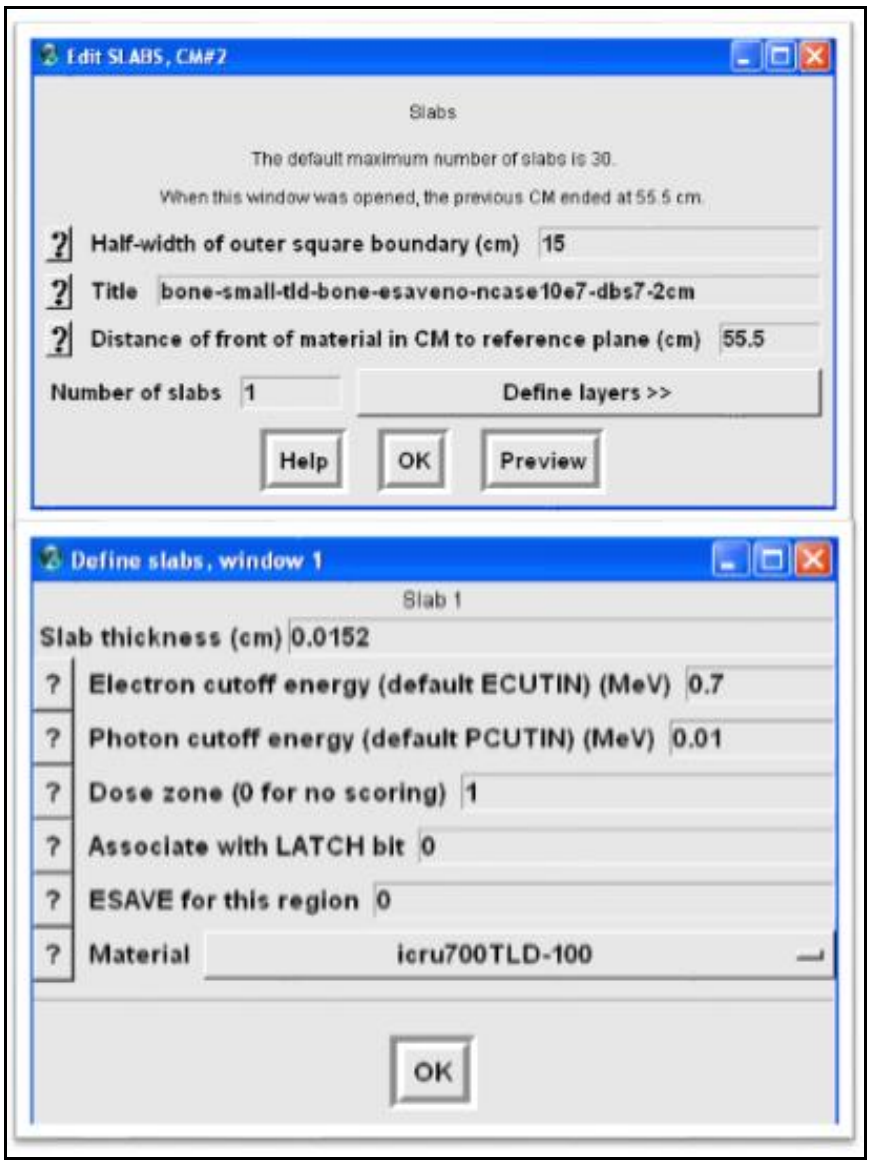

Figure 9: Information of CM2

- **Slab 3 : for bone**

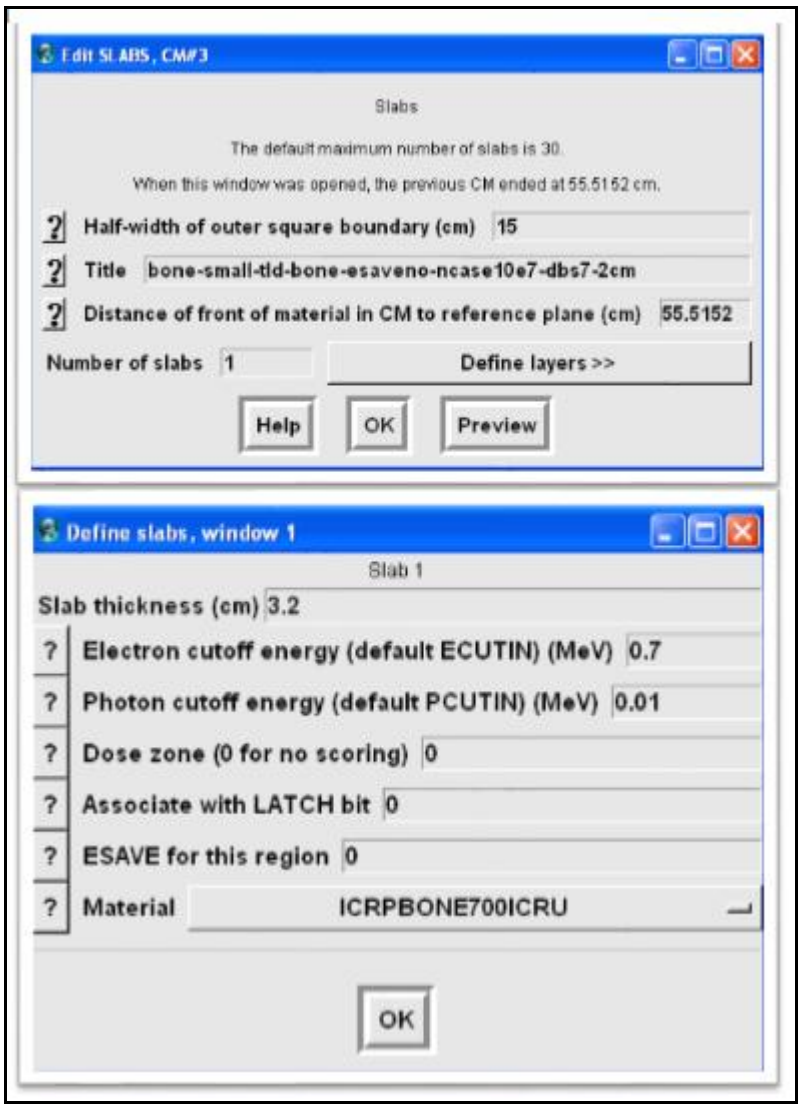

Figure 10: Information of CM3

Step 5: At the end of the creating of slabs, the main input data were entered the system (see Figure 11).

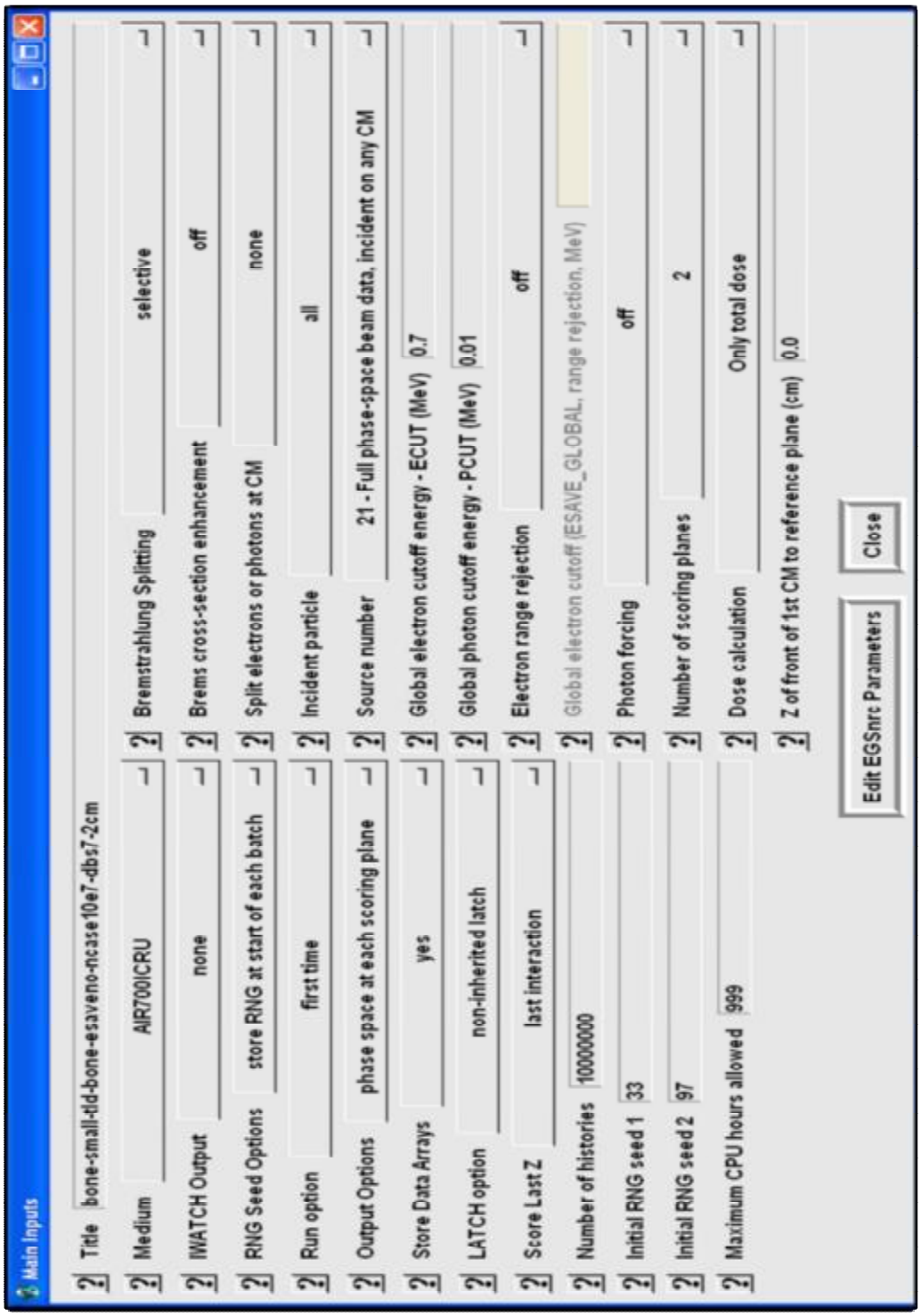

Figure 11: Main input data

Step 6: Finally the source section (Figure 12) was set up and the program was run.

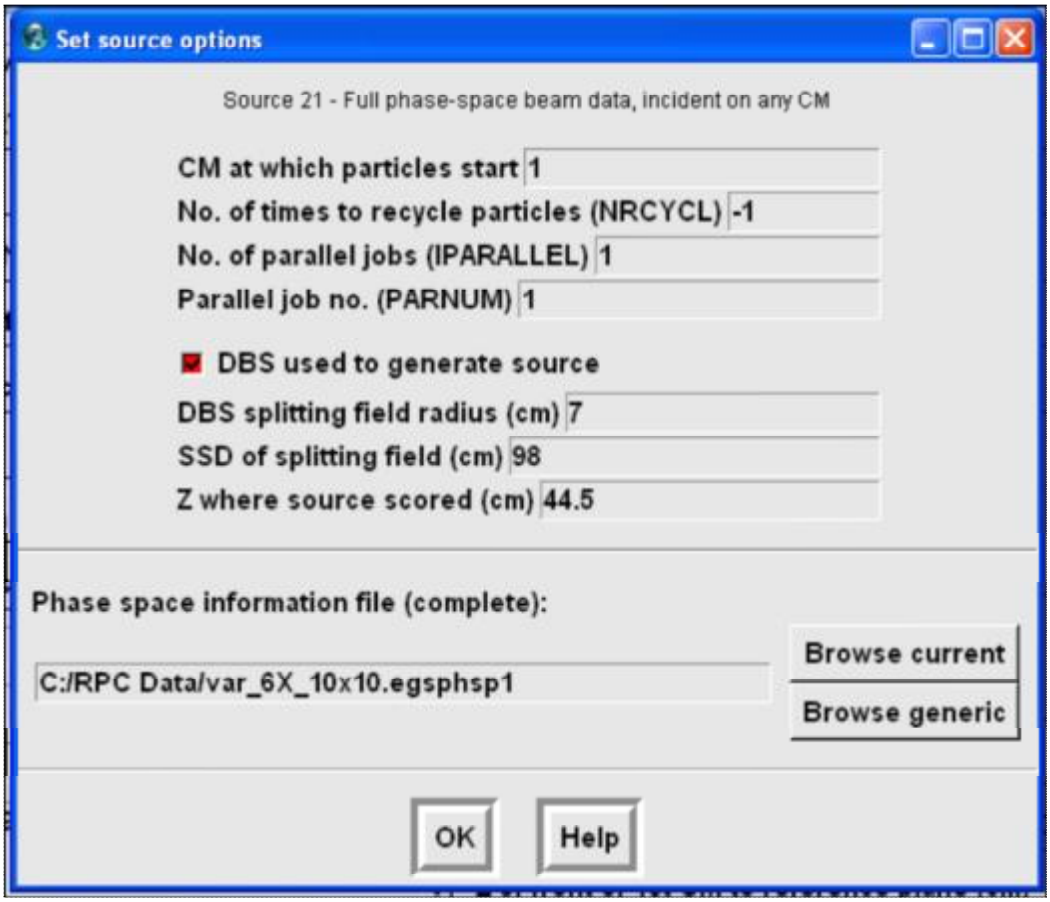

Figure 12: Source options

With this sections the phase space data were created on the bone phantom surface. In this study, the phase space data were created on bone, lung, water phantoms and TLD surface. The same process was applied to the other phantoms.

APPENDIX C

Beamdp Example: To Derive Energy Fluence Distribution from Ph-Sp (Phase Space) Data For Bone Phantom.

This appendix gives information how the energy fluence and spectral distribution were created from phase space data using beamdp GUI. But only energy fluence are showed in the appendix. If you see the spectral distribution, the same process is applied.

Step 1: The beamdp Gui (Figure 13) was opened and the "energy fluence distribution from phase space data" action was selected.

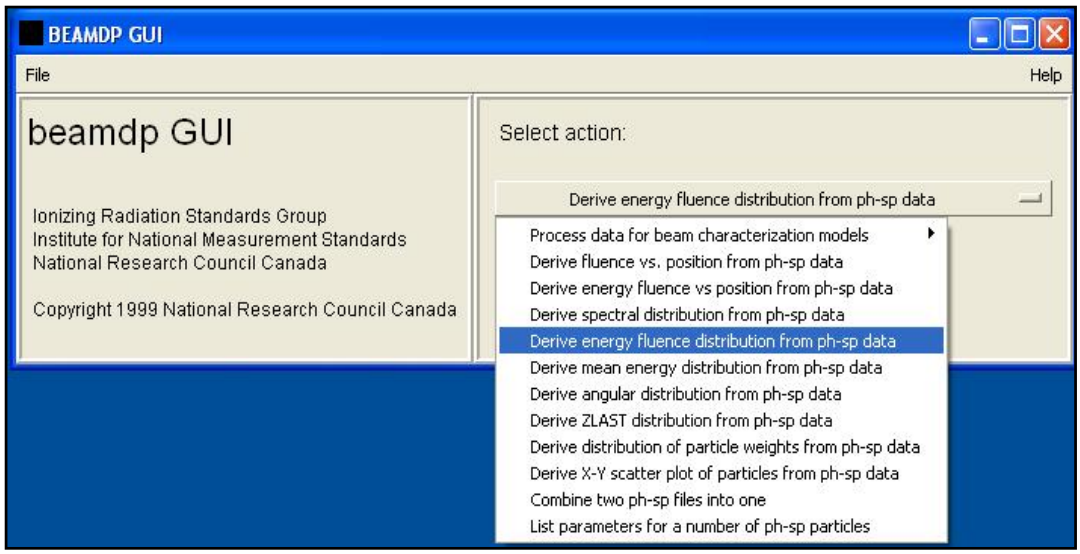

Figure 13: Beamdp Gui

Step 2: The inputs were entered to the following section (Figure 14) . In this study the field size was 10x10 cm^2 so the $x_{min\text{-}max}$ and $y_{min\text{-}max}$ were chosen ±5. The phase space data, are created by BEAMnrc, were selected. Then the programme was executed.

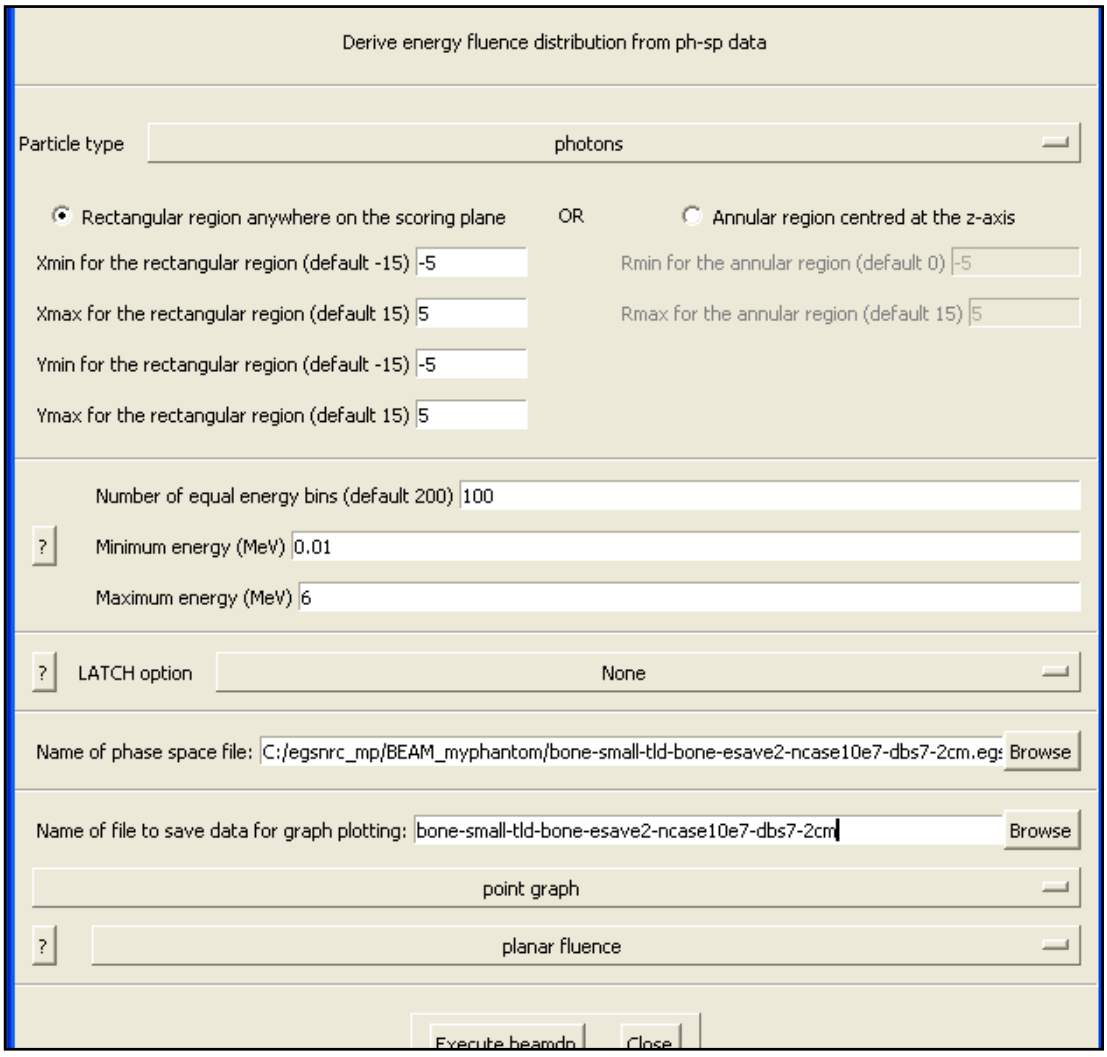

Figure 14: Input parameter to derive energy fluence from ph-sp data.

APPENDIX D

DOSXYZnrc

This appendix gives information about how the bone phantom was created. The lung and water phantom were created by the same method. This can be summarized in seven step.

Step 1: The DOSXYZnrc GUI (Figure 15) was opened and clicked file to choose "start a new input file".

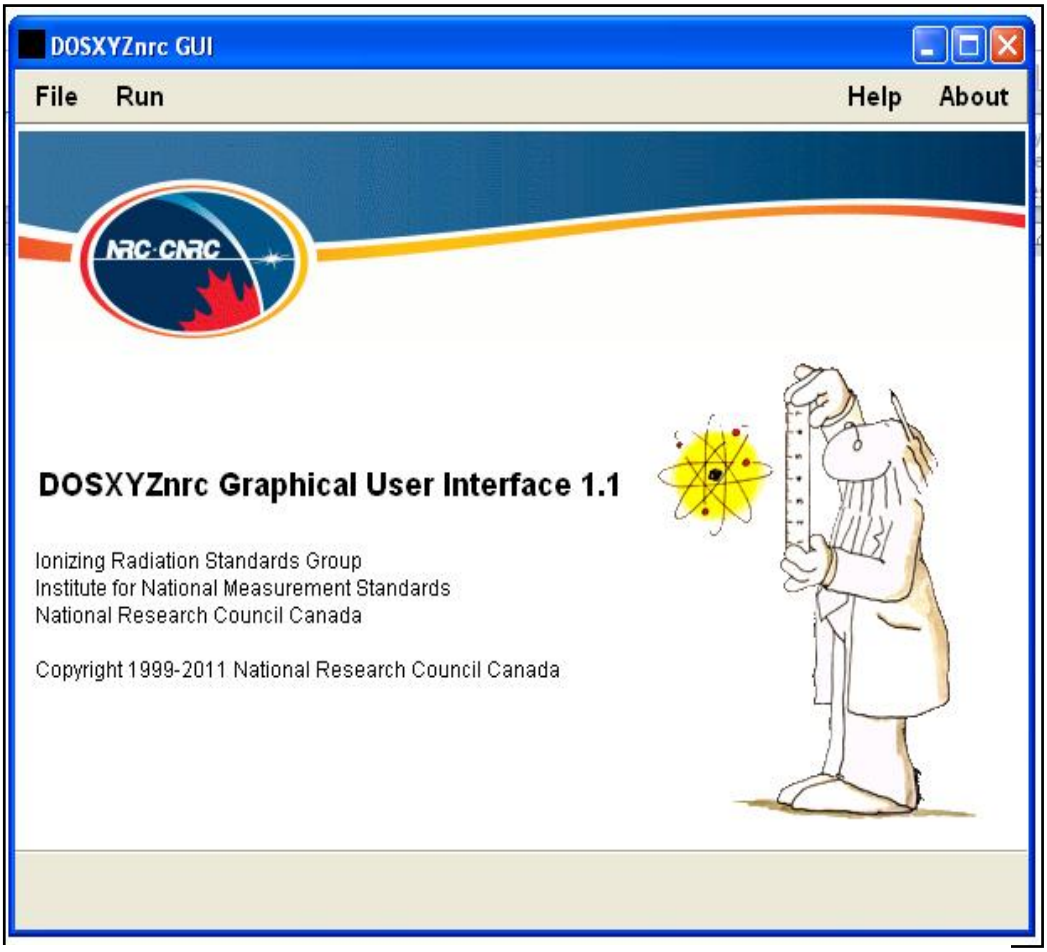

Figure 15: DOSXYZnrc Gui

Step 2: The pes4 data (Figure 16) was selected from "Browse HEN-HOUSE PEG4 Data"- 521icru.pegs4 file.

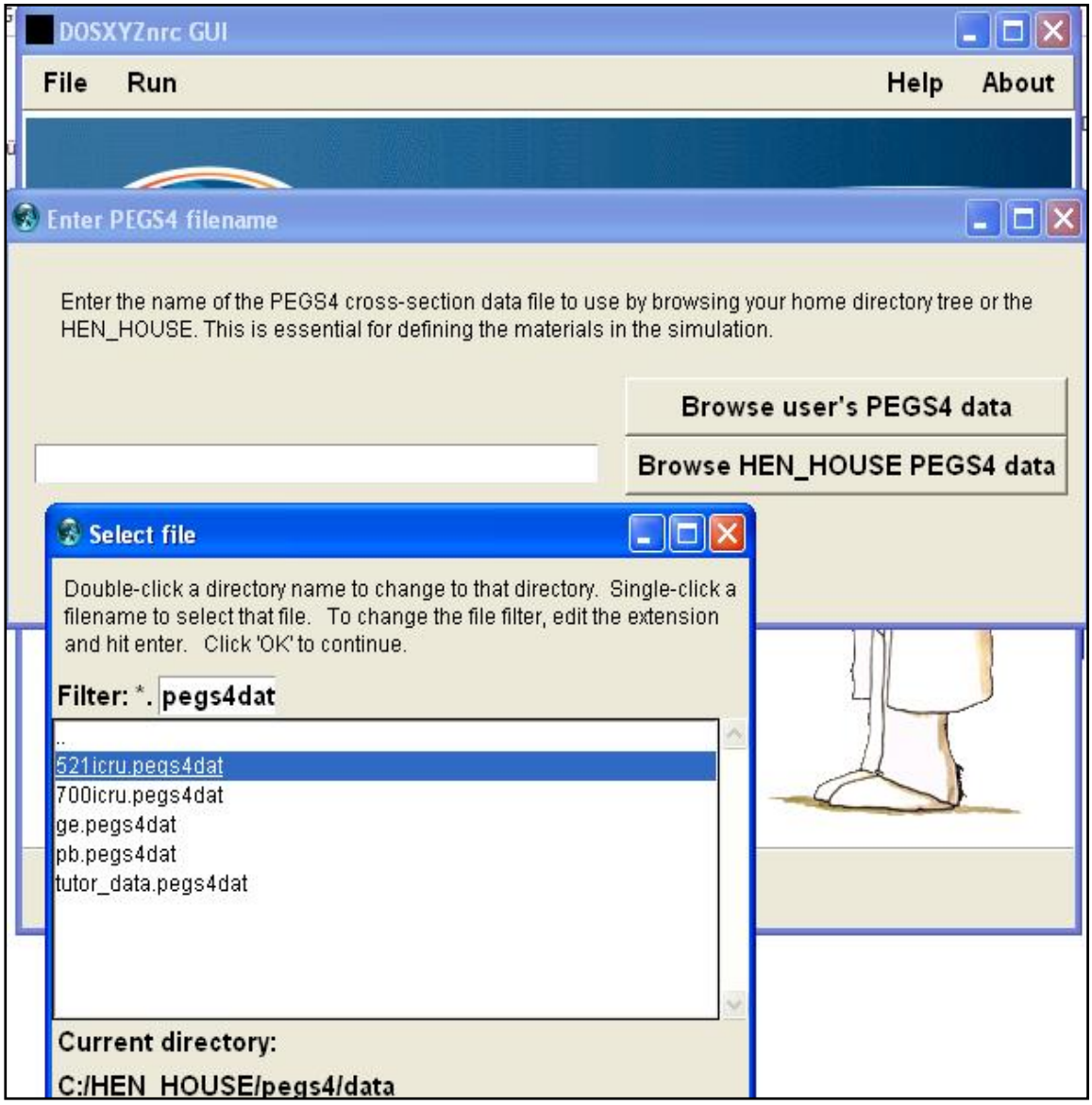

Figure 16: PEGS4 File

Step 3: The input parameter were entered the system as seen in the following Figure 17.

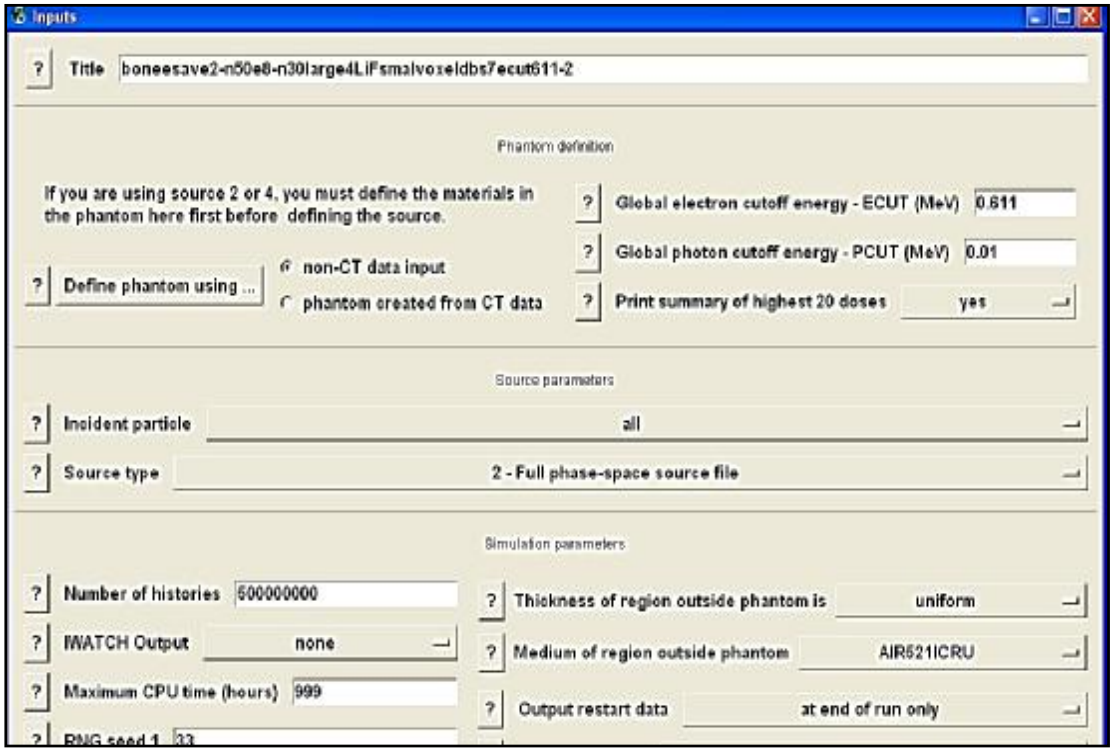

Figure 17: Input parameter for bone phantom.

Step 4: The “define phantom” section was selected to create the bone phantom with voxel dimensions. And this section the number of media was written 3 (Figure 18). They were ICRPBONE521ICRU-AIR521ICRU-TLD100 (LiFMgTi) (Figure 19).

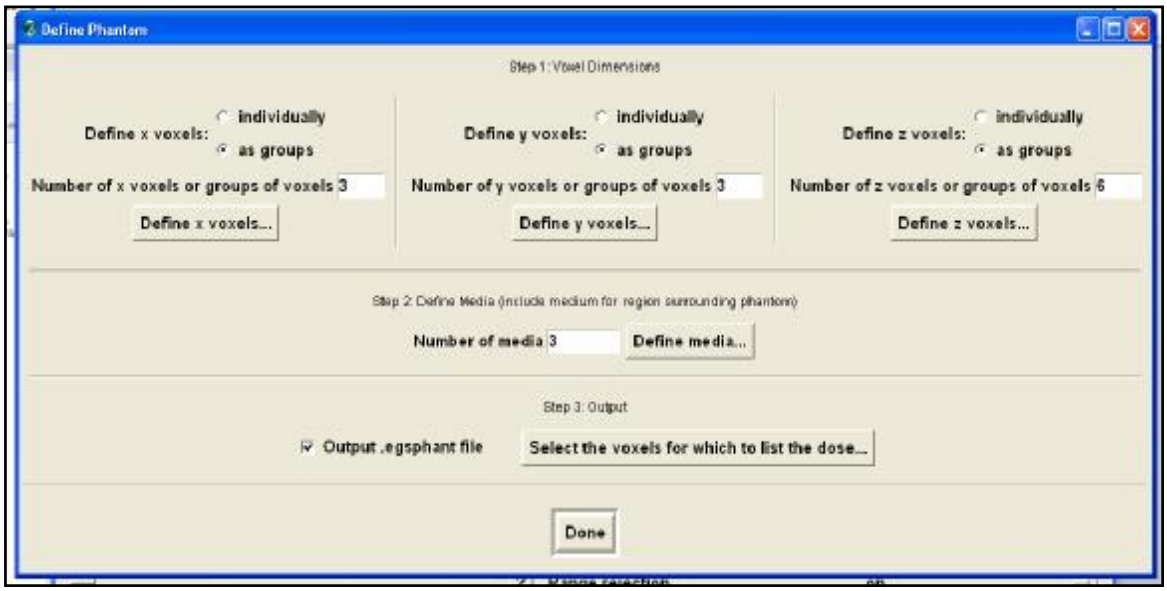

Figure 18: Phantom Design

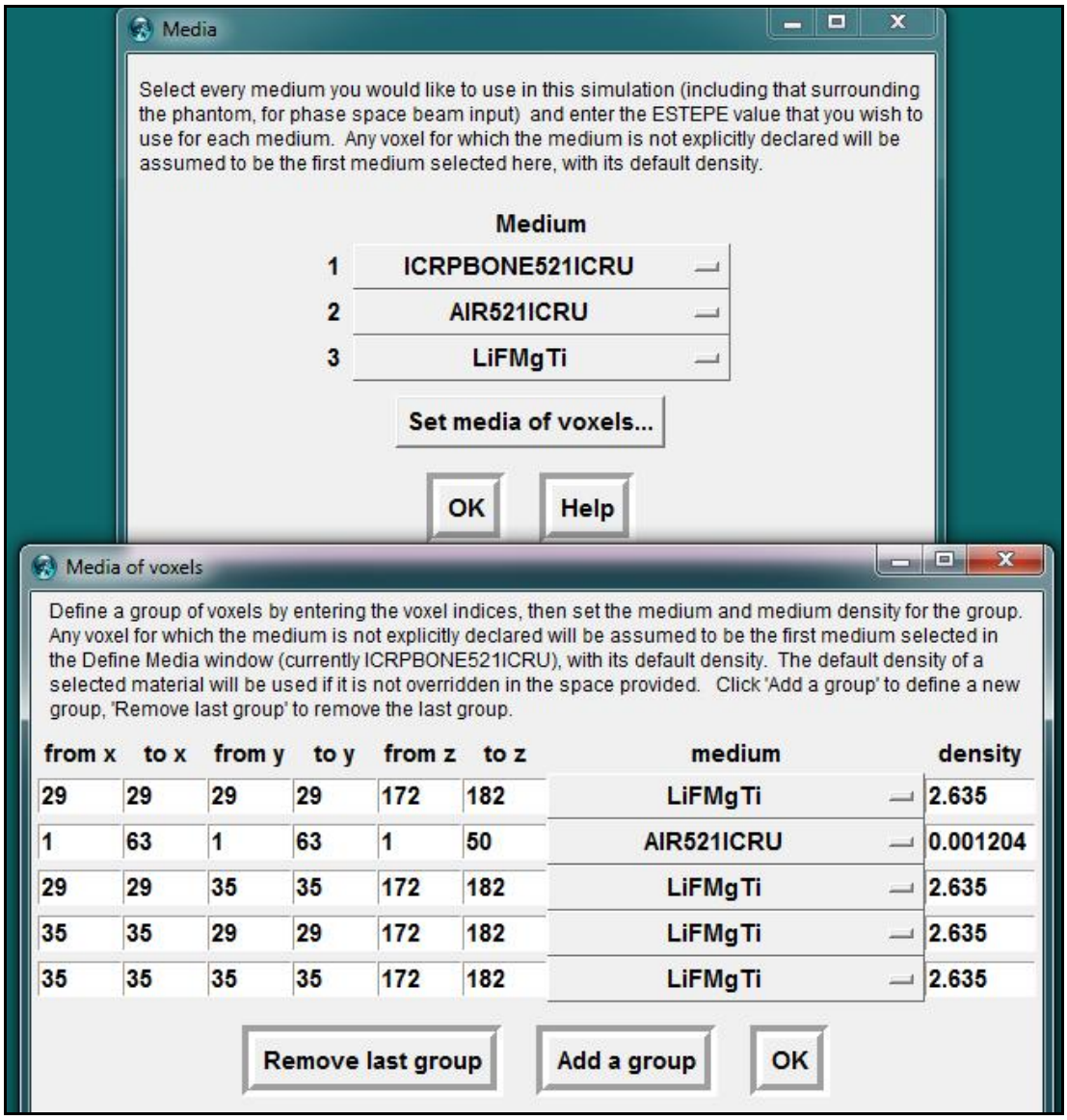

Figure 19: Media and media of voxels

Step 5: This section was chosen to see the PDD and isodose curve (Figure 20).

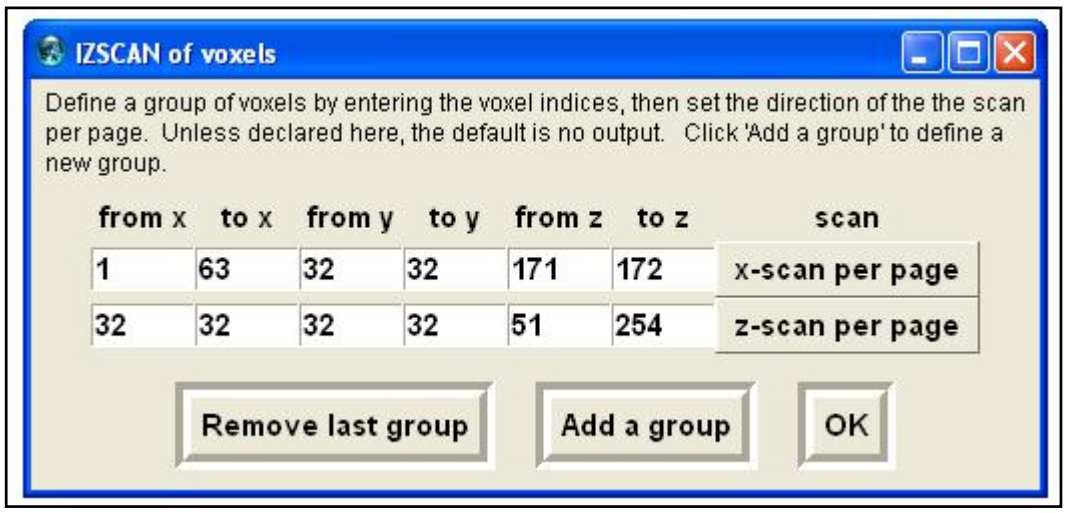

Figure 20: IZSCAN of voxels

Step 6: The source options were set up as shown in the following Figure 21.

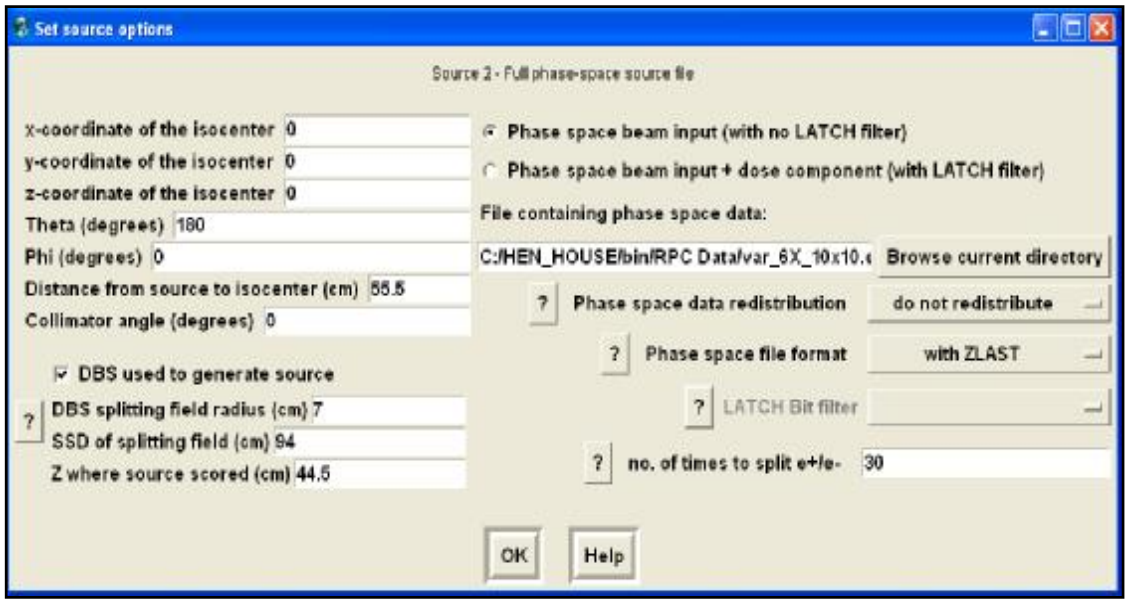

Figure 21: Source options

Step 7: After the all parameters were compiled, the programme was run. The data can opened by excel or MATLAB program.

APPENDIX E

PDD Curves

The following figures (Figure 22, Figure 23 and Figure 24) show the typical calculated dose distribution in the water, bone and lung phantom were obtained by Monte Carlo DOSXYZnrc programme.

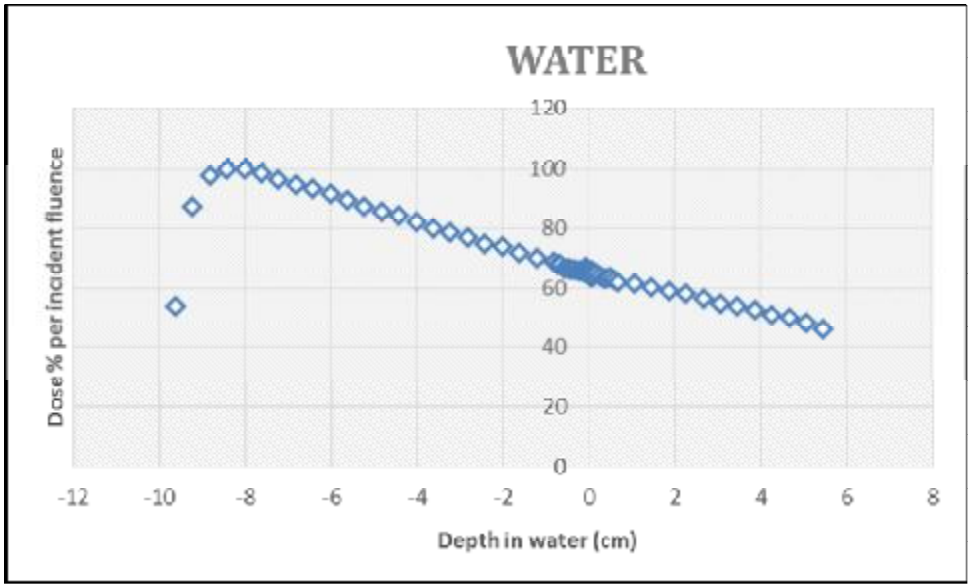

Figure 22: A typical calculated dose distribution in the water phantom for a 10x10 cm^2 field size was obtained by Monte Carlo DOSXYZnrc programme. Dmax was calculated in 1.6 cm at 10x10 cm^2 field size for 6 MV.

Figure 23: A typical calculated dose distribution in the bone phantom for a 10x10 cm^2 field size was obtained by Monte Carlo DOSXYZnrc programme. Dmax was calculated 0.8 cm at 10x10 cm^2 field size for 6 MV.

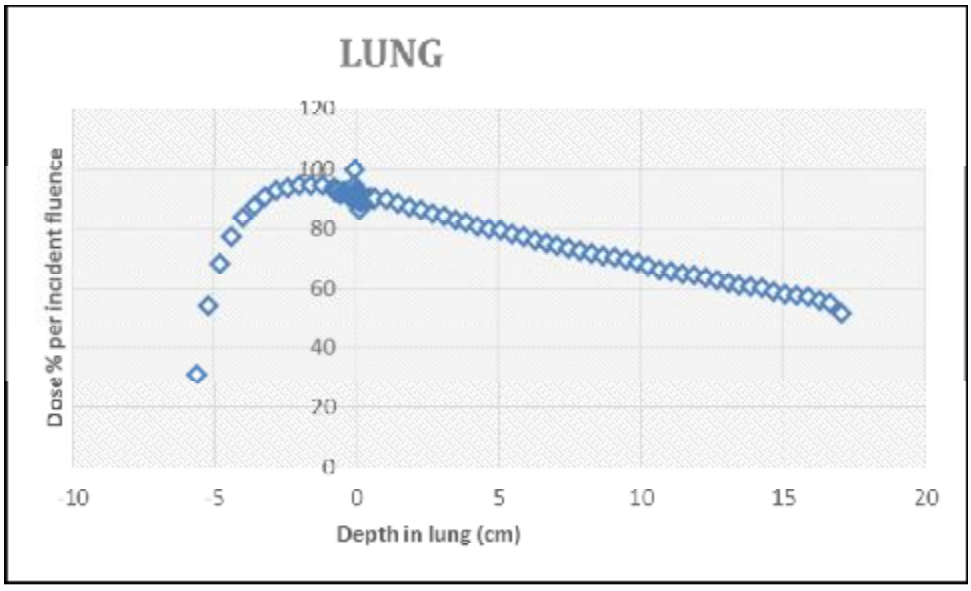

Figure 24: A typical calculated dose distribution in the lung phantom for a 10x10 cm^2 field size was obtained by Monte Carlo DOSXYZnrc programme. Dmax was calculated approximately 5.6 cm at 10x10 cm^2 field size for 6 MV.

APPENDIX F

MATLAB CODES

```
clear all
FilePath_a = ('*.3ddose');
% u=32;
[dose,error,xbound,ybound,zbound]=dicomrt_read3ddose(1, 'filename.3ddose');
% imshow(dose(:,:,u)/max(max(dose(:,:,u))))
[pmedia,pdensity,pmedname,pxbound,pybound,pzbound]=dicomrt_readegsphant(1,'
filename');
% figure;imshow(pdensity(:,:,u)/max(max(pdensity(:,:,u))))
[i,j,k]=size(dose);
m=0;
sumdose=0;
sumerror=0;
sumersqr=0;
doselist=[];
erlist=[];
for z=1:k
   for y=1:j
      for x=1:i
         if pmedia(x,y,z)==3
            sumdose=sumdose+dose(x,y,z);
            sumerror=sumerror+error(x,y,z);
            sumersqr=sumersqr+(error(x,y,z))^2;
            m=m+1;
            doselist(m)=dose(x,y,z);
            erlist(m)=error(x,y,z);
         end
      end
   end
end
```

```
avdose=sumdose/m
averror=sumerror/m

xx=round(x/2);
pdd=dose(xx,xx,:);
pdd=pdd(:);
figure;plot(zbound(1:z),pdd)
%%
% u=32;
clear all
[dose,error,xbound,ybound,zbound]=dicomrt_read3ddose(1, 'filename.3ddose ');
% imshow(dose(:,:,u)/max(max(dose(:,:,u))))
[pmedia,pdensity,pmedname,pxbound,pybound,pzbound]=dicomrt_readegsphant(1,'f
ilename');
% figure;imshow(pdensity(:,:,u)/max(max(pdensity(:,:,u))))
[i,j,k]=size(dose);
xx=round(i/2);
pdd=dose(xx,xx,:);
pdd=pdd(:);
for n=1:k
if pdd(n)==max(pdd)
                ii=n;
        end
end
mmax=(pdd(ii-1)+pdd(ii)+pdd(ii+1))/3
m=0;
sumdose=0
for z=1:k
        for y=1:j
                for x=1:i
                        if      pmedia(x,y,z)==3
```

```
                                    sumdose=sumdose+dose(x,y,z);
                                    doses(m+1,1)=x;
                                    doses(m+1,2)=y;
                                    doses(m+1,3)=z;
                                    doses(m+1,4)=dose(x,y,z);
doses(m+1,5)=dose(x,y,z)/mmax;
m=m+1;
                            end
                    end
            end
end
avdose=sumdose/m;
avdosenorm=avdose/mmax
```